Exploring LEO-Aided GPS Direct Position Estimation in Degraded Signal Environments

by

J. Tanner Koza

A thesis submitted to the Graduate Faculty of
Auburn University
in partial fulfillment of the
requirements for the Degree of
Master of Science

Auburn, Alabama
August 3, 2024

Keywords: Direct Position Estimation, LEO, GPS, Radio Frequency Interference

Approved by

Scott M. Martin, Chair, Assistant Professor of Mechanical Engineering
David M. Bevly, Bill and Lana McNair Distinguished Professor of Mechanical Engineering
Hunter C. Burch, Assistant Professor of Electrical Engineering

Abstract

Due to their low received signal power, Global Navigation Satellite Systems (GNSS) are easily subject to radio frequency interference (RFI). Subsequently, extensive research regarding advanced receiver designs that mitigate RFI is ubiquitous. Among these designs is the Direct Position Estimation (DPE) architecture, which addresses the shortcomings of conventional receivers by jointly processing all channels and estimating the receiver state in a single step. Combining each channel's received power, this single-step methodology proves more robust than receivers that fuse measurements from independently processed channels in two steps. Despite this robustness, DPE can still succumb to the effects of RFI. This thesis discusses the performance capabilities of two DPE architectures that utilize dedicated and opportunistic low Earth orbit (LEO) positioning, navigation, and timing (PNT) sources, respectively, to supplement the Global Positioning System (GPS) in various RFI scenarios. Specifically, a Bayesian DPE approach is applied to each architecture, and necessary modifications are introduced for each LEO source. Furthermore, a methodology that prevents the obfuscation of GNSS information by high-powered LEO signals is presented.

Each architecture's performance is evaluated using a Monte Carlo analysis that employs a correlator-level simulation of GPS L1 C/A. It is shown that including dedicated and opportunistic LEO sources substantially reduces the root mean square errors (RMSE) associated with the estimated position, velocity, and timing (PVT) states in high GPS attenuation regimes compared to other architectures. Specifically, the proposed architectures are compared to standalone GPS DPE, LEO-aided GPS Vector Processing (VP), and standalone GPS VP. The VP comparisons are included to gauge performance against a two-step methodology. The results also indicate that the probability of tracking GPS in the scenario with the highest RFI increases by up to 85.12% compared to the additional architectures. Furthermore, a simple computational efficiency study assesses the benefits of aiding the naturally computationally expensive

DPE architecture with dedicated LEO signals. Lastly, an open-source satellite navigation simulation environment is introduced.

Acknowledgments

Table of Contents

List of Figures

ix

<center>List of Tables</center>

List of Abbreviations

ADC   Analog-to-Digital Converter

AWGN Additive White Gaussian Noise

BPSK   Binary Phase Shift Keying

C/A   Coarse/Acquisition

C/N_0 Carrier-to-Noise Density Ratio

CAF   Cross-Ambiguity Function

CDMA Code-Division Multiple Access

CPU   Central Processing Unit

DLL   Delay Lock Loop

DoD   Department of Defense

DOP   Dilution of Precision

DPE   Direct Position Estimation

DSSS   Direct-Sequence Spread Spectrum

ECEF   Earth-Centered Earth-Fixed

EIRP   Effective Isotropic Radiated Power

EKF   Extended Kalman Filter

FDE   Fault Detection and Exclusion

FFT   Fast Fourier Transform

FLL   Frequency Lock Loop

FPGA   Field-Programmable Gate Array

FSPL   Free-Space Path Loss

GNSS   Global Navigation Satellite Systems

GPS   Global Positioning System

GPST   GPS Time

GPU   Graphics Processing Unit

IFFT   Inverse Fast Fourier Transform

ISA   International Standard Atmosphere

LEO   Low Earth Orbit

LNAV   Legacy Navigation

LOS   Line-of-Sight

MEO   Medium Earth Orbit

MLE   Maximum Likelihood Estimation

PLL   Phase Lock Loop

PNT   Positioning, Navigation, and Timing

PPS   Precise Positioning Service

PRN   Pseudorandom Noise

PSD   Power Spectral Density

PVT   Position, Velocity, and Timing

RF   Radio Frequency

RFI   Radio Frequency Interference

RMSE   Root Mean Square Error

SA   Selective Availability

SDR   Software-Defined Receiver

SGP4   Simplified General Perturbations 4

SIR   Sequential Importance Resampling

SNR   Signal-to-Noise Ratio

SOP   Signal of Opportunity

SP3   Extended Standard Product 3

SPS   Standard Positioning Service

STL   Satellite, Timing, and Location

SWaP-C Size, Weight, Power, and Cost

TCXO   Temperature-Compensated Crystal Oscillator

TDMA   Time Division Multiple Access

TEC   Total Electron Count

TLE   Two-Line Element

UE   User Equipment

VDFLL   Vector Delay-Frequency Lock Loop

VDLL   Vector Delay Lock Loop

VP   Vector Processing

WNLS   Weighted Nonlinear Least Squares

Chapter 1

Introduction and Background

1.1 Motivation

The emergence of new-age technologies requires unprecedented positioning, navigation, and timing (PNT) accuracy across the globe [1]. For decades, Global Navigation Satellite Systems (GNSS) have been the standard for position, velocity, and timing (PVT) solutions in various applications, such as high-precision agriculture and stock exchange synchronization. However, the quality of these standalone solutions is becoming insufficient as state-of-the-art services, such as urban air mobility and autonomous ride-sharing, demand better performance [2, 3]. In addition, the widespread reliance on low-powered GNSS signals threatens existing mass-market civil, industrial, and military applications. Specifically, sustained signal degradation or loss could significantly jeopardize public safety and global financial stability. In fact, O'Connor et al. [4] estimates the United States economy would suffer daily losses of $1 billion during a Global Positioning System (GPS) outage. Therefore, recent research aims to maximize GNSS capabilities while reducing their exposure as singular points of failure.

The limitations of GNSS can be attributed to various factors, many of which are readily addressed. However, the effects of natural and malicious radio frequency interference (RFI) are challenging to handle. Hence, RFI frequently disrupts the standard operation of GNSS user equipment (UE). This disruption stems from the significant power diffusion of GNSS signals from medium Earth orbit (MEO). Specifically, adverse propagation conditions, such as multi-path, atmospheric scintillation, and jamming, can easily overwhelm these signals and render GNSS UE useless [5]. This thesis is motivated by the impact of such conditions and the benefits of mitigating their influence on GNSS performance and resilience.

1.2 Research Statement

The research presented in this thesis focuses on bolstering GNSS performance with low Earth orbit (LEO) satellite constellations and advanced receiver architectures. Although each has been studied in detail, the intersection of these domains is largely unexplored in the literature, leaving much to be researched regarding modern GNSS augmentation.

The present realization of broadband mega-constellations in LEO has significantly influenced the exploration of GNSS alternatives. This influence results from the high received power and geometric diversity of these constellations, which directly address the shortcomings of GNSS in MEO. This thesis explores using the signals from such constellations to augment an advanced GNSS receiver architecture. The considered architecture uses the principles of Direct Position Estimation (DPE) to maximize solution accuracy in environments with significant GNSS RFI. Coupling the benefits of broadband LEO constellations and DPE promises increased performance of GNSS solutions in unfavorable signal conditions.

The studies conducted in this thesis evaluate the performance of LEO-aided DPE receiver architectures for GPS in degraded signal environments. GPS is selected because it is the most prevalent GNSS. The studies assume dedicated and opportunistic LEO PNT sources to address the current state of such aiding. These aiding sources are considered to be operating in ideal signal conditions. Additionally, a comparison to other advanced architectures is conducted to illustrate relative performance gains.

1.3 Prior Art

This section presents an overview of recent literature addressing the adverse impact of RFI on GNSS signals. Given the broad scope of this problem, publications relevant to the research domains discussed in Section 1.2 are solely included. Hence, the highlighted works are detailed in two subsections: LEO Positioning, Navigation, and Timing and Direct Position Estimation.

1.3.1 LEO Positioning, Navigation, and Timing

Historically, considerable production and launch costs have forced satellite constellations to use the expansive coverage of high orbital altitudes. High altitudes are attractive as fewer satellites are required to achieve global service, reducing overall expenses. For this reason, GNSS have been placed in MEO ($\sim$20,000 km) instead of LEO ($<$2000 km), allowing for smaller constellations of less than 50 satellites. Figure 1.1 illustrates the difference in satellite coverage from these orbits.

Figure 1.1: GNSS and LEO Orbital Altitude Comparison

Limiting the size of GNSS is important as current generation satellites (e.g., GPS Block III) cost upward of $500 million to produce and launch [6]. Thus, GNSS are discouraged from joining LEO—eliminating the possibility of higher received power and resulting performance gains. However, a new paradigm in the space industry is prioritizing practices that

allow for a 10 to 100 fold reduction in the price per kilogram of orbital launch [7]. This recent initiative—named *New Space*—has enabled broadband mega-constellations in LEO whose spreading losses are up to 28 dB less than GNSS [8]. This benefit, among others, has sparked interest in using LEO constellations to handle or avoid the effects of GNSS RFI. For further context, Table 1.1 compares the trade-offs between GNSS and LEO.

Table 1.1: Comparison of Typical LEO and MEO Systems for Navigation

	MEO (GPS)	LEO (Iridium)	LEO-to-MEO Ratio
Altitude	$20{,}200\,\text{km}$	$780\,\text{km}$	$1:25$
Spreading Loss at Zenith	$-97\,\text{dB}$	$-69\,\text{dB}$	$28\,\text{dB}$
Coverage Area	$1.73 \times 10^8\,\text{km}^2$	$1.93 \times 10^7\,\text{km}^2$	$1:9$
Coverage Radius	$7900\,\text{km}$	$2500\,\text{km}$	$1:3$
Mean Motion	$0.008\,°/\text{s}$	$0.06\,°/\text{s}$	$7:1$
Orbital Period	$12\,\text{h}$	$100\,\text{min}$	$1:7$
Multi-Path Decorrelation Time	$10\,\text{min}$	$1\,\text{min}$	$1:10$
Note. Adapted from Reid et al. [8]			

Today, notable names in New Space have prioritized delivering broadband communications with mega-constellations in LEO (e.g., Starlink, OneWeb, and Kuiper). For this reason, equipping these systems with PNT capabilities has been of little importance or entirely disregarded. This emphasis on communications service has motivated considerable research into using LEO mega-constellations as signal of opportunity (SOP) sources. This section presents a brief overview of PNT approaches using LEO SOPs. In addition, the few existing and future constellations that address the shortage of dedicated LEO PNT are highlighted.

Signals of Opportunity

In practice, SOPs are ambient, non-cooperative signals that can offer PNT capabilities despite being designed for other applications. They are openly available and generally maintain functionality in environments with significant GNSS RFI. Typical sources of SOPs include cellular networks, radio broadcasts, and LEO constellations, the last of which is detailed in this section.

The literature regarding LEO SOPs is fairly extensive, as there are a few approaches to using them. Most approaches utilize measurements of the received signal's carrier frequency (i.e., Doppler shift) and batch them over time to compute PVT solutions using a limited number of satellites [9–12]. In addition, methods of blind tracking LEO SOPs can produce range measurements used in a trilateration problem that determines a receiver's PVT states [13, 14]. Similar to this thesis, there is a subset of the literature that looks to use these methods to directly aid GNSS [15–17].

Although these opportunistic methods are promising, they are still heavily limited by the non-cooperative nature of LEO SOPs. Specifically, the main problems associated with LEO SOPs are their unknown satellite states [18] and signal structures [19]. Also, the observability of these systems is typically poor, reducing their potential as PNT sources [20]. This motivates the dissemination of dedicated LEO PNT signals through commercial constellations.

Dedicated LEO PNT

The idea of dedicated LEO PNT is not entirely new. In fact, it predates modern GNSS [21], but had been cast away for decades in favor of systems in MEO. However, the emergence of New Space and LEO mega-constellations has inspired commercial entities to revisit the idea. Specifically, these entities want to implement LEO PNT signals into existing and new constellations to provide performance that can supplant GNSS. This section briefly highlights some of the projects pursuing dedicated LEO PNT today.

Iridium NEXT is a constellation that has been at the forefront of bringing PNT to LEO. Traditionally used for communications, this constellation added a navigation signal in 2016 that reports nanosecond timing accuracy and position accuracy of 10 meters [22]. Unfortunately, this constellation can only guarantee one satellite in view at a time for all users, preventing it from achieving GNSS PNT quality. In addition, other existing communications constellations like OneWeb [23] and Globalstar [24] look to venture into the PNT space.

Conversely, other projects are prioritizing PNT by launching constellations whose sole purpose is to transmit navigation signals. These projects include constellations from Xona

Space Systems [25] and TrustPoint [26], which have recently received additional funding to pursue their respective LEO PNT systems [27, 28].

1.3.2 Direct Position Estimation

DPE improves upon conventional receiver architectures by processing received channels and estimating a receiver's state in a single step. This single-step approach is more robust in high RFI environments than conventional methods that independently process received channels and fuse the resulting measurements in a separate processing stage. DPE's robustness results from combining the received signal power from all considered satellites. This combination facilitates aiding between channels and allows for the ongoing processing of signals subjected to RFI, an unachievable outcome in most conventional architectures.

The idea of DPE was introduced for GNSS in [29] and has been built upon the last few years. Much literature has focused on establishing the theoretical foundations of this method [30–32]. Conversely, other work has assessed the practical implications and applications of DPE [33–37]. This thesis aims to build upon the idea of Bayesian DPE by exploiting the methodologies presented in [38–40].

1.4 Research Contributions

This research seeks to initiate the exploration of advanced LEO-aided GNSS receiver architectures that employ Direct Position Estimation. Considering this, several academic contributions have been made and are summarized as follows.

- A description of a DPE architecture that utilizes dedicated LEO PNT signals to aid GPS is provided.

- A description of a DPE architecture that utilizes opportunistic LEO PNT Doppler shift measurements to aid GPS is provided.

- An algorithm for fusing LEO and GNSS signals with vastly different nominal received powers.

- A Monte Carlo analysis is conducted across various interference scenarios to evaluate the performance of the dedicated and opportunistic LEO PNT GPS DPE architectures relative to other advanced architectures.

- A simple computational efficiency study is performed to assess the benefits of dedicated LEO PNT aiding in a DPE architecture.

- An open-source satellite navigation simulation environment called Navsim is introduced.

1.5   Thesis Outline

The remainder of this thesis is organized as follows. Chapter 2 introduces GPS with a brief history of the system, an explanation of the architecture, and examples of its modern applications. In addition, the components of the GPS L1 C/A signal structure are presented. Chapter 3 defines the foundations of GNSS software-defined receivers and offers a brief description of the vector processing architecture used for comparison. Chapter 4 outlines the investigated Direct Position Estimation architectures and modifications needed to incorporate assistance from LEO. Chapter 5 details the open-source simulation environment developed to perform this research. Chapter 6 provides the results of three studies that evaluate the performance of the proposed architectures. Finally, Chapter 7 discusses conclusions and offers future work.

Chapter 2

The Global Positioning System

The creation of GPS in the late 20th century revolutionized PNT across the globe. Upon its inception, GPS delivered positioning and timing capabilities previously unattainable, ushering in the new age of GNSS. The resulting proliferation of GNSS (e.g., Galileo, GLONASS, Bei-Dou) has reduced the technological advantage of GPS. Nonetheless, GPS maintains its status as the most widely used GNSS. For this reason, this thesis considers GPS when assessing the performance of LEO-aided DPE receiver architectures.

This chapter provides a brief overview of the GPS constellation. Specifically, the history, architecture, and current applications of GPS are highlighted in Section 2.1. In addition, the GPS L1 C/A signal structure is detailed in Section 2.2. The GPS L1 C/A signal is chosen for its pervasiveness—i.e., it is transmitted by all operational satellites and utilized by most commercial receivers. The context supplied in this chapter provides the reader with a general understanding of GNSS by explaining GPS and its legacy civilian signal.

2.1 Overview of GPS

The Global Positioning System, formally known as the NAVSTAR Global Positioning System, was approved by the United States Department of Defense (DoD) in 1973. The primary purpose of this system was to provide the military with PNT that was accurate and globally available. Over two decades, the initial system was developed and deployed, with the first satellite launched in 1978 and global operation declared in 1995. In addition to military service, GPS was approved for civil use to benefit industries such as commercial aviation. Therefore, GPS was divided into two standardized services to maintain better performance for military use: the Precise Positioning Service (PPS) and the Standard Positioning Service (SPS). GPS's full

capabilities were available in the PPS, but access to this service required DoD authorization. This authorization forced civil users to employ the SPS, which was intentionally degraded to an accuracy of 100 meters [41]. Throughout the 1990s, these services coexisted until a study sponsored by Congress determined the degradation of the SPS was unnecessary and should be discontinued [42]. Hence, the so-called Selective Availability (SA) was deactivated by a Presidential Order on May 2, 2000 [43, 44]. The dismantling of SA allowed civilian GPS applications to thrive, creating a global dependence on GNSS.

2.1.1 System Architecture

The GPS architecture comprises three main components or segments—the space segment, the control segment, and the user segment. Figure 2.1 illustrates these segments in a simplified operational setting.
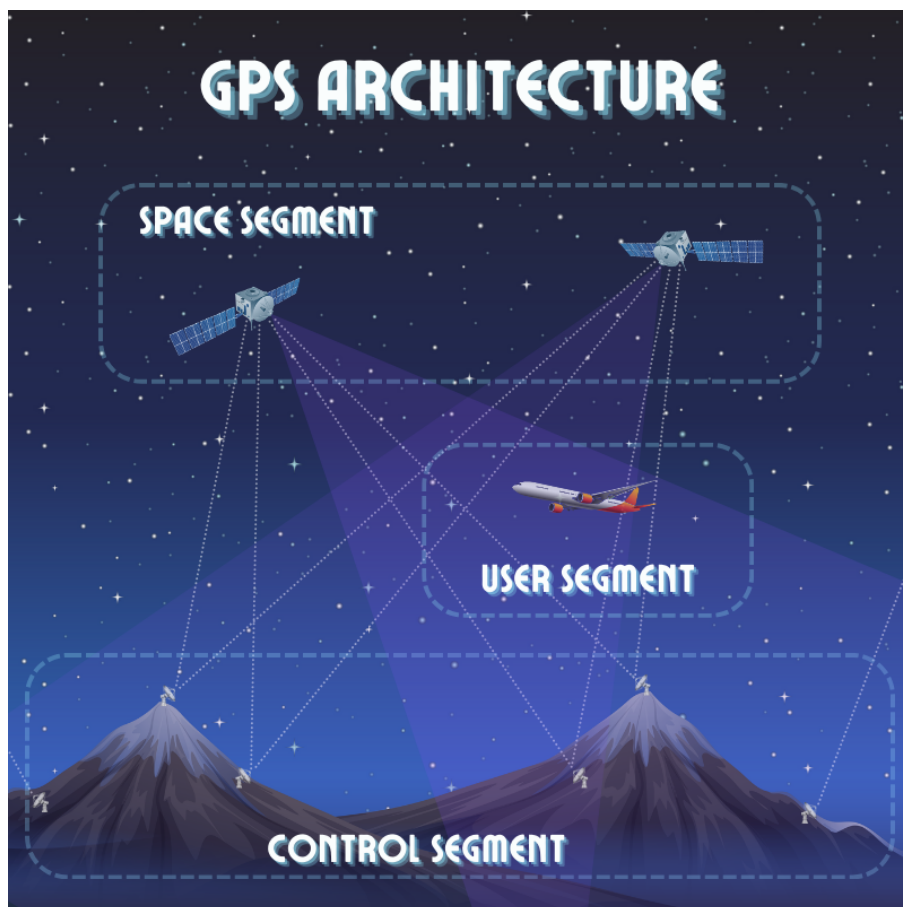
Figure 2.1: GPS Architecture Segmentation

The space segment consists of up to 32 satellites, with a minimum of 24 being operational at all times. Currently, 31 operational satellites exist in six orbital planes. These orbital planes are defined by inclination angles of 55 degrees and altitudes near 20,200 kilometers, resulting in orbital periods of nearly 12 hours [45]. These orbital characteristics allow at least four satellites in view at a time, satisfying the minimum number needed to compute a PVT solution anywhere in the world.

The control segment—managed by the U.S. Space Force in Colorado Springs, Colorado—comprises a master control station, multiple monitoring stations, and a group of ground antennas worldwide. The monitoring stations collect and send ranging information to the master control station to compute precise satellite orbits. This information is then sent to each satellite from the ground antennas and broadcasted in a navigation message used by GPS UE. In addition, the control segment maintains GPS time (GPST) and computes parameters that convey the state of each satellite's atomic clock. GPST is a time reference that enables the computation of nanosecond-level transit times from multiple satellites, allowing GPS to have standard meter-level accuracy. Figure 2.2 provides a world map of the control segment's infrastructure.
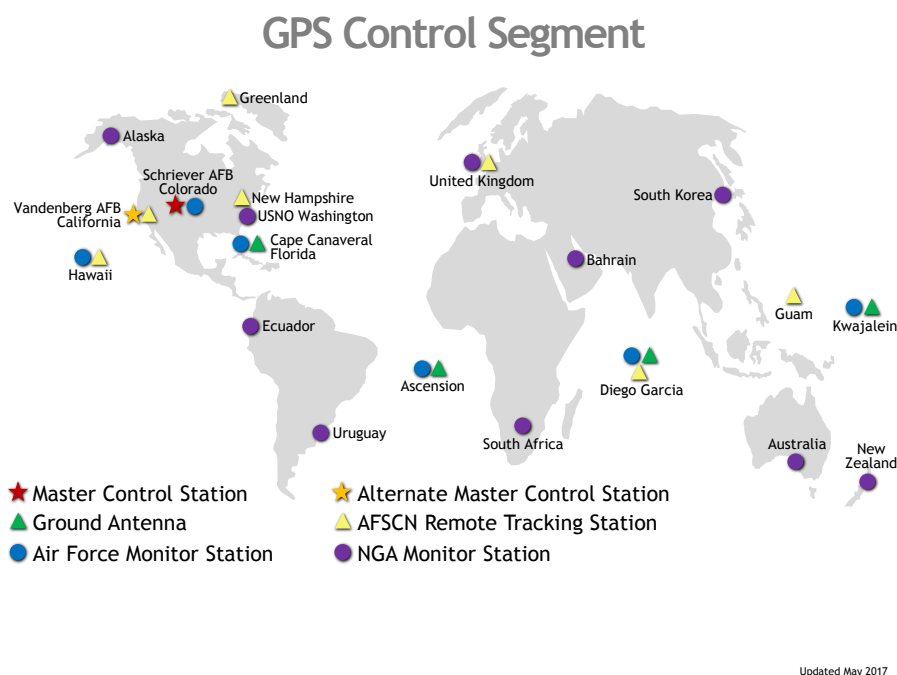
Figure 2.2: GPS Control Segment Global Infrastructure [46]

10

The user segment is simply the collection of all UE that utilizes GPS. This includes all commercial and military technology (i.e., receivers, processors, and antennas) used to determine signal observables and their corresponding position, velocity, and timing.

2.1.2   Current Applications

Over the years, GPS has been applied to many civil applications, causing tremendous growth in technologies comprising the user segment and its affiliated platforms. These applications can be broadly organized into four categories:

- consumer products for everyday use,

- precise timing dissemination,

- precise (sub-meter-level) positioning,

- highly specialized applications (e.g., commercial aviation and space navigation).

The ubiquity of smartphones in the consumer space has enabled GNSS—and GPS—to become part of daily operations for almost six billion devices [47]. In addition to navigation applications (e.g., Google Maps, Apple Maps, Waze), GPS has found its way into new location-based services such as ride-sharing, delivery services, and mobile gaming. The combination of GPS and other technologies (e.g., wireless communications) has catalyzed many commercial industries, promoting the growth of GPS as a technology that enables practical services, convenience, and leisure. In fact, the European Union Agency for the Space Programme [47] estimates GPS and GNSS global revenues will rise from more than €260 billion ($\sim$\$283 billion) in 2023 to roughly €580 billion ($\sim$\$632 billion) in 2033. Figure 2.3 presents commercial industries that use GPS.

Despite being often disregarded, GPS is just as crucial in synchronizing system times as it is for positioning worldwide. The ability to synchronize to GPST allows governments and businesses access to nanosecond-level timing without the cost of maintaining atomic clocks. This synchronization is critical to systems such as communications networks, financial institutions,

Figure 2.3: Commercial Industries Implementing GPS Features [48]

and electrical power grids, which would otherwise require extensive timing infrastructures specific to each application. The use of timing from GPS has proven cost-effective as it supplied the telecommunications and electrical sectors with benefits of $685.990 billion and $15.730 billion, respectively, from 1984 to 2017 [4].

In addition, GPS is being used to achieve precise positioning in many demanding applications. GPS carrier phase measurements and augmentation infrastructures have allowed real-time and post-process position determination with centimeter-level accuracy. This accuracy has proven beneficial to many technical disciplines (e.g., agriculture and geodesy) where precise control and knowledge of small position changes are imperative.

GPS currently enables many highly specialized applications. The most critical of these applications is found within the commercial aviation industry. Before GPS became globally available, commercial pilots relied on strapdown inertial navigation systems and ground-based radio navigation aids to maintain assigned flight paths. Now, GPS supplements these systems to provide consistent safety and efficiency that was previously intermittent or unachievable.

Furthermore, the space industry presents a specialized application of GPS that is especially relevant to this thesis. The orbit determination of LEO satellites with GPS UE has allowed the New Space initiative to take hold, significantly reducing operating costs in LEO. For this reason, the LEO mega-constellations that have inspired this research can be realized.

2.2 The GPS L1 C/A Signal

GPS currently broadcasts multiple signals from the space segment. As demand for better performance has grown, GPS has introduced these signals with new generations, or blocks, of satellites. The available signals span three subsections of the L-band (1 GHz to 2 GHz) in the radio spectrum and are depicted with their spreading modulations in Figure 2.4.
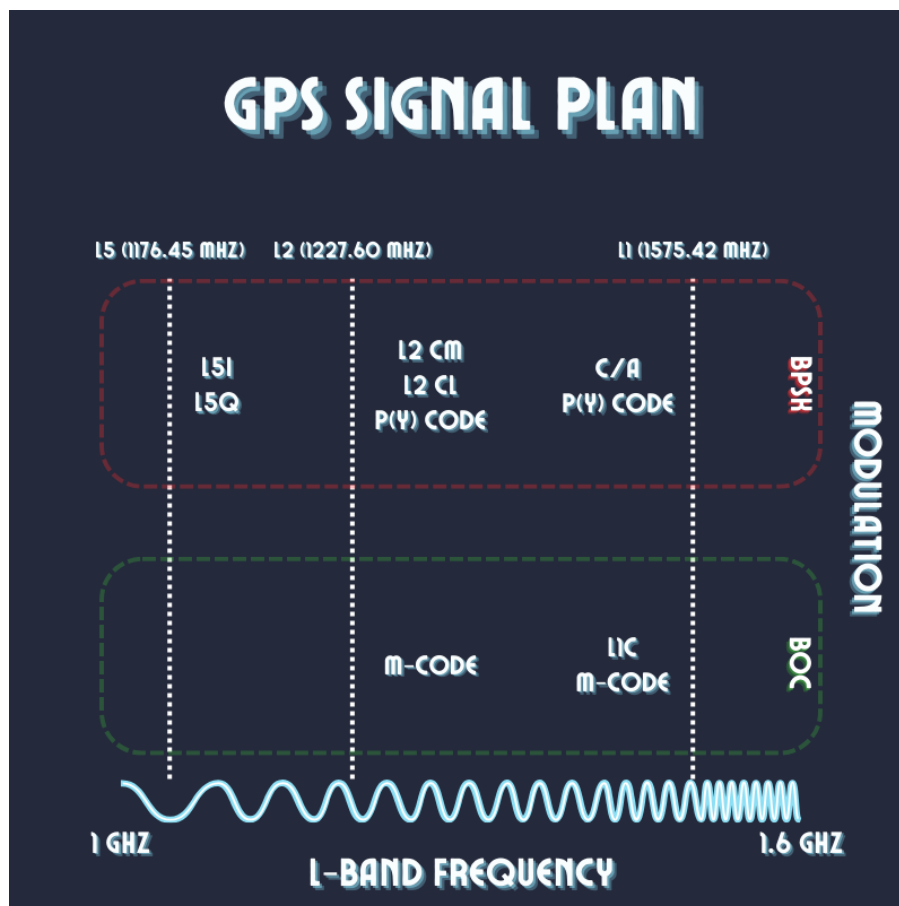
Figure 2.4: GPS Signal Plan and Spectrum

GPS L1 C/A, the legacy civilian signal, has been chosen for this thesis as it is available on all satellite blocks. The L1 C/A signal consists of three main components that are detailed in this section—the carrier signal, the Coarse/Acquisition (C/A) code, and the navigation message

13

created by the control segment. The combination of these components can be seen in the GPS L1 C/A signal model given by the following

$$s^{(j)}(t) = \sqrt{2P}x^{(j)}D^{(j)}\cos(2\pi f_{L1}t + \theta) \tag{2.1}$$

where P is the signal power, $x^{(j)}$ is the current C/A code value for the jth satellite, $D^{(j)}$ is the current bit value of the jth satellite's navigation message, f_{L1} is the L1 carrier signal frequency in Hertz, and θ is the carrier signal phase in radians.

2.2.1 Carrier Signal

The L1 C/A carrier signal is a sinusoidal signal centered at a frequency of 1575.42 MHz in the L-band. This frequency and band are selected to allow the signal to penetrate the Earth's ionosphere and troposphere with minimal delays. All GNSS currently exist in the L-band for this reason. Further, high-frequency L-band carrier signals allow for high-bandwidth spreading sequences like the C/A code.

2.2.2 Coarse/Acquisition Code

The C/A code is a Pseudorandom Noise (PRN) code that allows for each satellite to be simultaneously received by GPS UE without any cross-channel interference. This type of channel access method is called Code-Division Multiple Access (CDMA) and is standard across most GNSS. A set of PRN codes called Gold codes enable CDMA through specific correlation properties [49]. Specifically, the autocorrelation function of a Gold code resembles that of Gaussian noise, solely correlating with a phase-matched replica of itself. In other words, the autocorrelation value is only significant at a sequence delay of less than one bit (or chip). Further, the resemblance to Gaussian noise reduces any cross-correlation with the codes of other satellites. The autocorrelation function of a GPS L1 C/A Gold code is depicted in Figure 2.5.
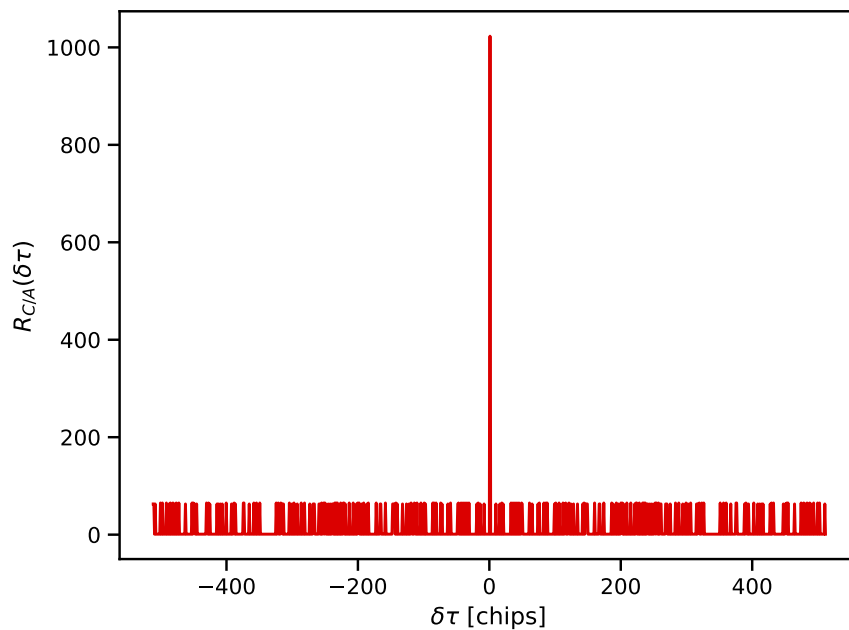
Figure 2.5: C/A Code Autocorrelation Function

The C/A code is a spreading sequence of data called chips that repeats every millisecond. Each code comprises 1023 chips transmitted from each satellite at a rate of $1.023\,\mathrm{MHz}$. Often called the ranging code, the C/A code can provide knowledge of each satellite's timing through these chips, which can be converted to ranging information. This timing is conveyed through tracking the code phase (i.e., sub-chip sequence position) on each received channel. The designation of the C/A code as a spreading sequence comes from the effect of Binary Phase Shift Keying (BPSK) modulation. BPSK is implemented by multiplying the C/A code and carrier signal, causing sudden phase transitions of π radians that allow data transmission on a constant frequency signal. As a result of this rapid phase modulation, the carrier signal is effectively spread across the frequency domain, increasing the bandwidth and decreasing the signal's power. This decrease in signal power, coupled with the transmission from MEO, causes GPS L1 C/A to be received below the thermal noise floor. The spreading effects can be seen by the modulation shown in Figure 2.6.

15
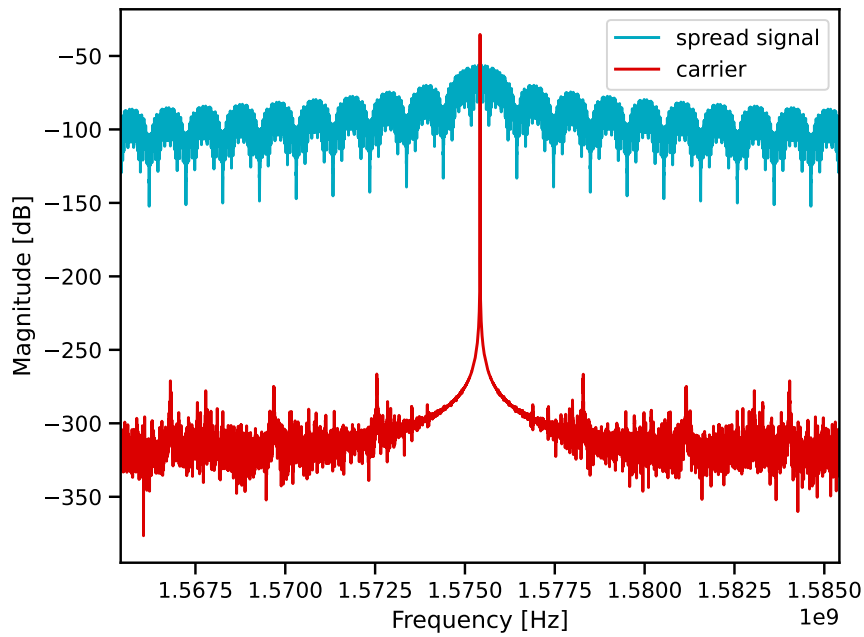
Figure 2.6: Power Spectral Density of C/A Code Modulation on L1 Carrier Signal

2.2.3 Legacy Navigation Message

In addition to the C/A code, a low-rate data message is modulated on the carrier signal. This message is called the legacy navigation (LNAV) message and is sent at a bit rate of 50 Hz. This rate corresponds to a bit period of 20 milliseconds, allowing for 20 C/A code repetitions per bit transmitted. Each bit is part of 25 frames that last 30 seconds, forming a master frame transmitted over 12.5 minutes. Each frame comprises five sub-frames of 10 words, with 30 bits per word.

The sub-frames encompass details concerning the clock parameters and orbital information, referred to as ephemeris, of the respective satellite alongside atmospheric model parameters and constellation-wide information. Sub-frames 1, 2, and 3 contain the clock and ephemeris information regarding the transmitting satellite and are repeated in each frame. This repetition allows GPS UE to obtain the information required to form a PVT solution within 30 seconds despite the longer master frame duration. Sub-frames 4 and 5 transmit data regarding the entire constellation and are the same across all satellites. The data transmitted in these

16

sub-frames is spread over the 25 frames comprising the master frame, defining the total message period. Figure 2.7 presents the general structure of the LNAV message. More information regarding the LNAV message can be found in the latest GPS Interface Control Document [50].
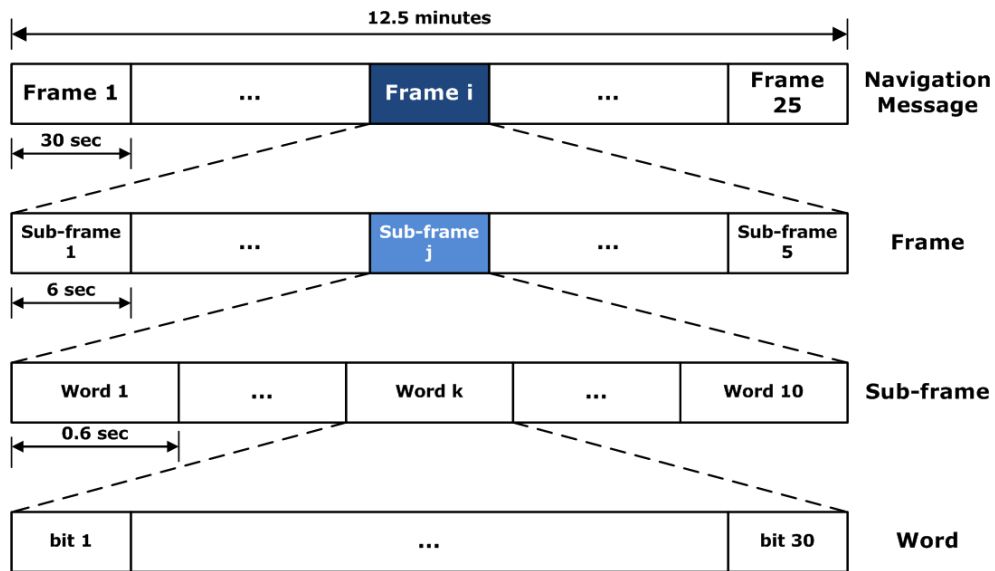
Figure 2.7: Legacy Navigation Message Structure [51]

Chapter 3

Principles of GNSS Software-Defined Receivers

Generally, GNSS receivers operate by attempting to replicate received signals to produce observables related to the receiver's PVT states. Initially, this operation was exclusively implemented with hardware optimized for low-cost and real-time operation, as general-purpose computational resources were insufficient. Despite being beneficial for fielded systems, such implementation prevents easy modification of the underlying PNT algorithms, which proves unfavorable for rapid development and analysis. This immutable nature and the evolution of computing hardware have motivated the creation of software-defined receivers (SDR) for GNSS.

The benefit of SDRs comes from the ability to process GNSS signals with the same accuracy as hardware receivers while being rapidly reprogrammable. This characteristic enables many new PNT algorithms that would otherwise be difficult to develop, warranting the explanation of an SDR's operational principles. This chapter explains the general hardware configuration and underlying PNT algorithms that comprise a GNSS SDR to contextualize the advanced receiver architectures presented in this thesis. In addition, information regarding an advanced vector processing SDR architecture is provided for later comparison.

3.1 Software-Defined Receivers

GNSS SDRs, widely introduced for GPS and Galileo in [52], are post-process or real-time GNSS receivers that aim to facilitate the rapid development of PNT algorithms. Commonly, SDRs consist of four hardware/interfacing components: an antenna, a front end, a processing unit, and a user interface. Once received by the antenna, radio frequency (RF) signals are mixed down to an intermediate or baseband frequency by the front end. Then, these mixed signals are

filtered with a bandpass filter (BPF) and amplified with a low-noise amplifier (LNA). Finally, the front end's analog-to-digital converter (ADC) transforms the RF signals into discrete samples. The processing unit—often a Central Processing Unit (CPU), Graphics Processing Unit (GPU), or Field-Programmable Gate Array (FPGA)—applies three general processing stages to produce a PVT solution from the discrete samples. This PVT solution is then displayed through a user interface. This description of an SDR's hardware configuration and internal data transmission, illustrated in Figure 3.1, is oversimplified as it is not the focus of this thesis. The reader is referred to Chapter 8 in [53] for further information. The rest of this section focuses on the processing stages used to determine a PVT solution, the first being signal acquisition.
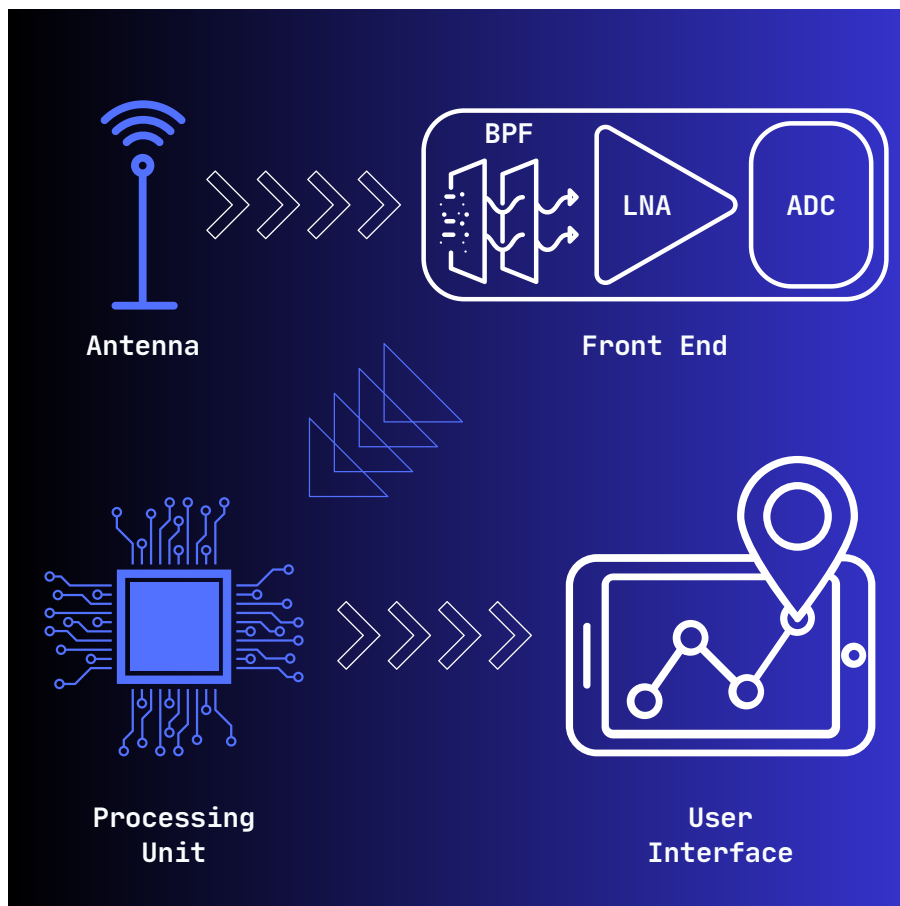
Figure 3.1: SDR Hardware Configuration and Internal Data Transmission

3.1.1 Signal Acquisition

After front end sampling, the processing unit must determine which satellite transmissions are found in the resulting discrete samples through signal acquisition. The purpose of signal

acquisition is to begin the continuous processing of each received channel by identifying three channel parameters: the identity of each transmitting satellite, the signal's code phase, and the signal's Doppler shift. This identification is accomplished using the correlation of the received samples with various local signal replicas. Considering the Direct-Sequence Spread Spectrum (DSSS) signal model given in the previous chapter (Equation 2.1) for GPS L1 C/A, the baseband local signal replicas can be written as

$$s^{(j)}(t) = \sqrt{2P}x(t-\tau)^{(j)}D(t-\tau)^{(j)}\cos(2\pi f_d t + \theta) \tag{3.1}$$

where P is the signal power, τ is the time delay associated with the transit time and system clock biases, f_d is the baseband Doppler shift associated with the relative dynamics and system clock drifts, $x^{(j)}$ is the current C/A code value for the jth satellite, $D^{(j)}$ is the current bit value of the jth satellite's navigation message, and θ is the carrier replica phase in radians.

The significant distinction between Equation 2.1 and Equation 3.1 is the inclusion of the unknown signal parameters τ and f_d. A local signal replica represented by Equation 3.1 only resembles the received signal when the τ and f_d of each signal match. In other words, when the correlation between the replica and received samples is maximized. The ability to distinguish a maximum comes from the correlation properties of a DSSS signal's ranging code. Specifically, the autocorrelation function of these codes (e.g., GPS L1 C/A Code in Section 2.2.2) solely allows significant correlation at a τ whose corresponding code phase nearly matches a received signal's code phase. During acquisition, a receiver must generate a replica for all satellites and potential τ (i.e., all code phases) to resolve each channel's identity and received code phase. As this section continues, τ will be used interchangeably to refer to a received signal's time delay or code phase.

In addition, the correlations are only discernible when each channel's f_d is known within a range (or bin) of $\frac{1}{2T_{PDI}}$Hz, where T_{PDI} is the pre-detection integration period in seconds. Considering an extensive range of Doppler shifts can be produced by the relative satellite and receiver motion (e.g., around ±5 kHz in a static scenario), a concurrent search for each channel's τ and f_d bin must be performed.

Two main acquisition algorithms can be used to search across the τ and f_d domains for each satellite. The first algorithm is a serial search that successively checks each possible code phase and Doppler bin. This algorithm is excessively slow with a computational complexity of $\mathcal{O}(n^2)$, prohibiting its use in many SDR acquisition schemes. The second algorithm is a parallel search that utilizes the Fast Fourier Transform (FFT) and Inverse FFT (IFFT) to reduce the computational complexity to $\mathcal{O}(n \log n)$. Specifically, the parallel search algorithm uses the FFT to test all code phases simultaneously in each successive Doppler bin. A block diagram of this algorithm is depicted in Figure 3.2.
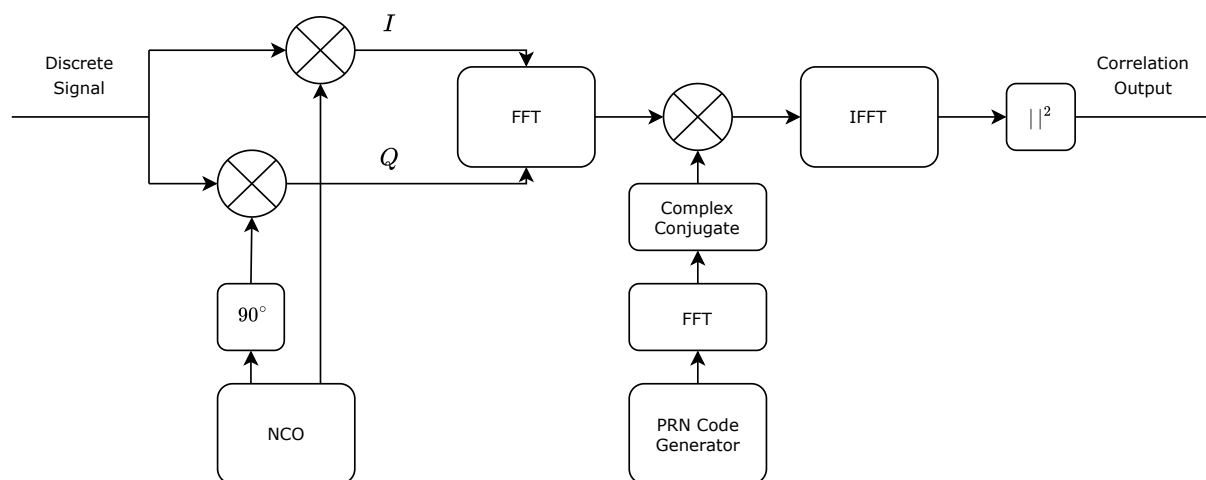
Figure 3.2: Parallel Code Phase Search Algorithm

For both algorithms, the length of time used to correlate (i.e., the pre-detection integration period) is pivotal in reducing the effect of noise in weak GNSS signals. The longer the correlation, the larger the effective signal-to-noise ratio (SNR), which is the basis for most detection criteria. However, there are limitations to the selection of T_{PDI}. In the case of GPS L1 C/A, coherent pre-detection integration periods are limited to 10 milliseconds because of the 20-millisecond LNAV message bit period. This integration constraint is necessary as phase coherence can only be guaranteed in one of two consecutive 10-millisecond integration periods before LNAV message synchronization. On the other hand, the lower limit of integration for conventional receivers is restricted by the ranging code period duration, which is one millisecond for GPS L1 C/A. It should be noted that the complex in-phase and quadrature correlation

21

outputs (or correlators) for multiple coherent integration periods can be non-coherently combined to increase the resulting correlation. This methodology is typically used in GNSS signals with higher navigation message data rates. Yet, a drawback of this methodology is a raised noise floor, given the noise no longer destructively adds across integration periods.

The output of a GNSS signal acquisition algorithm is a Cross-Ambiguity Function (CAF) that can be visualized as a manifold of correlator power in the τ and f_d plane. The location of any significant peak in this manifold indicates the τ and f_d needed to begin signal tracking for a successfully acquired satellite. Figures 3.3 and 3.4 show an example CAF for a received and obscured GPS satellite, respectively. For additional information regarding the presented acquisition algorithms, the reader is referred to [41, 52, 53].
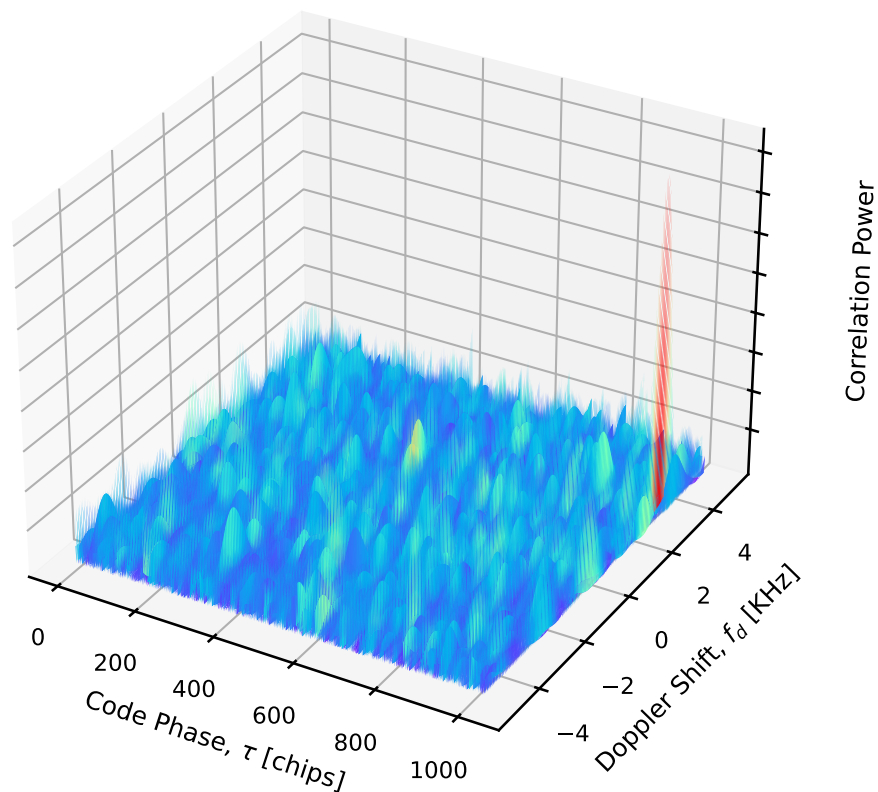
Figure 3.3: Acquisition CAF for Received GPS Satellite
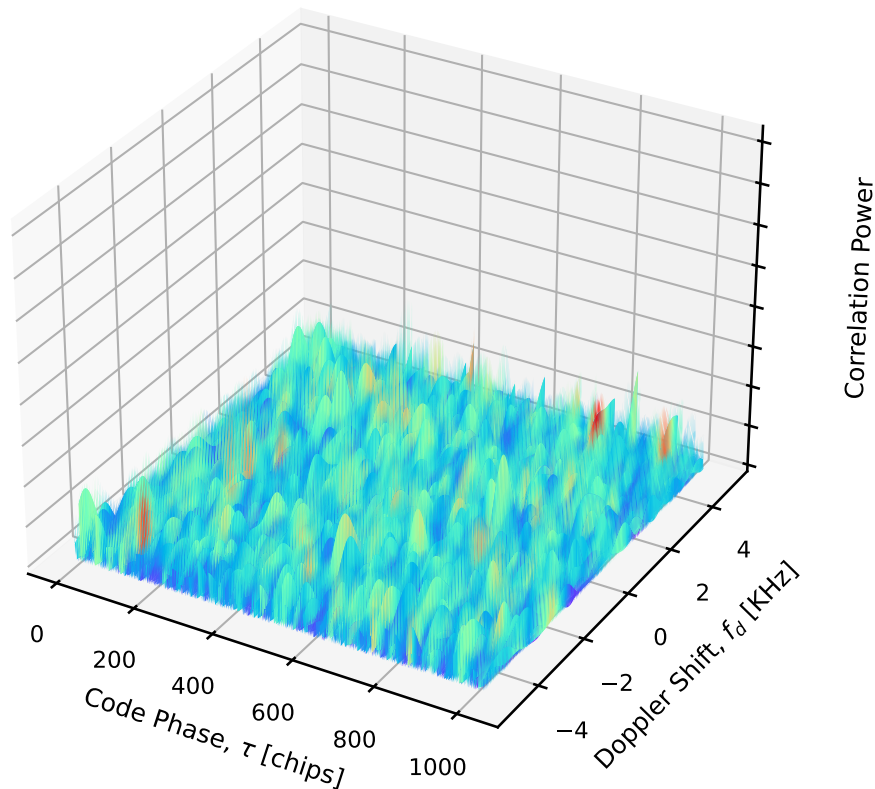
Figure 3.4: Acquisition CAF for Obscured GPS Satellite

3.1.2 Signal Tracking

After determining the current code phase and Doppler shift for each received satellite, the receiver must update these values as they change with relative satellite and receiver motion. The process of continually updating these parameters is called signal tracking. Although signal tracking can be accomplished through repeated acquisition (i.e., in a snapshot receiver), a much more efficient process that uses similar principles is available. In general, this process correlates local signal replicas with the received signals, generates signal parameter errors using the resulting correlators, and filters these errors to update the local signal replicas' parameters. Through signal tracking, the receiver can continually measure the signal's transit time and Doppler shift. Then, these measurements can be used in an estimation architecture to provide a PVT solution. In addition, the phase reversals imparted by the navigation message can be observed and decoded to extract the ephemeris needed to locate the transmitting satellites.

The conventional method of signal tracking is based on simple control theory. Feedback controllers update local replica Doppler shifts to reduce phase and frequency errors determined by discriminator functions. Specifically, two types of controllers called Delay Lock Loops (DLL) and Phase Lock Loops (PLL) are used to track the received code phase and carrier phase, respectively. In the case of code tracking, the DLL uses the code phase determined in acquisition to begin. However, for the PLL, there is no initial phase estimate. For this reason, the PLL uses the acquired Doppler shift, whose quality determines whether an additional tracking stage is needed. This extra stage is unnecessary if the Doppler shift estimate from acquisition is accurate. However, if the estimate is inadequate, a Frequency Lock Loop (FLL) must be used to refine the Doppler shift before precise phase tracking. This refinement may also be done in the acquisition stage using FFT methods [52]. An accurate initial Doppler shift is needed to achieve carrier phase lock, which allows a receiver to extract the modulated navigation message.

Figure 3.5 illustrates the generalized structure that the DLL and PLL share. It comprises a discriminator that determines the code or carrier phase error, a loop filter that low-pass filters the error, and a Numerically-Controlled Oscillator (NCO) that integrates the code or carrier frequency correction output from the loop filter. The resulting phase correction updates the local signal replicas before the process is repeated.
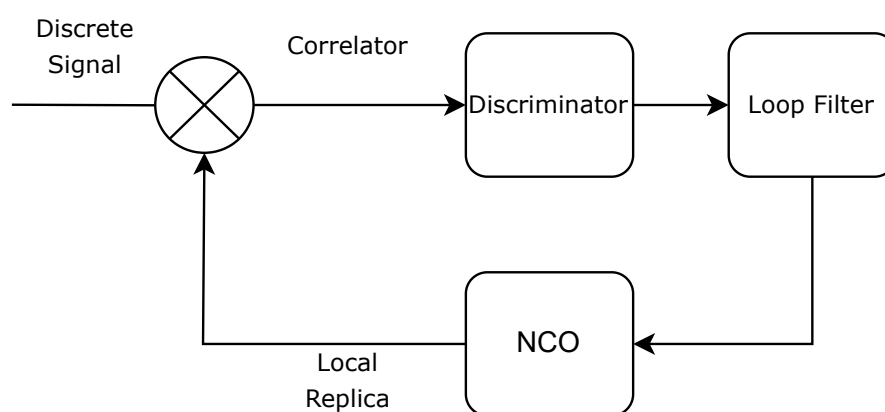
Figure 3.5: Generalized DLL/PLL Structure

The multiplication informing the discriminator in Figure 3.5 indicates a correlation—often called an integrate and dump period—with the received signal. The result of this correlation, as

mentioned in Section 3.1.1, is called a correlator. In most GNSS receivers, six correlators are used to maintain code and carrier signal tracking, which means three complex signal replicas divided into their in-phase and quadrature components are needed. For this reason, tracking in this manner is highly efficient compared to repeated acquisition.

The three replicas are distinguished by their respective code phase offsets. The first replica is called a prompt replica, whose code phase is the current best estimate of the received signal's code phase. The following two replicas are called the early and late replicas, whose code phases are typically advanced or delayed within half of a chip of the prompt replica. The in-phase and quadrature components of the prompt replica are used in the PLL discriminator to determine the current carrier phase error. In contrast, the DLL discriminator uses the early and late replica complex components to update the code phase error. The model for the correlator that results from each of the local replica correlations is given by the following from [54]

$$IP_j = AR(\epsilon)D_j \cos(\pi f_{err}T_{PDI} + \theta_{err}) + \eta_{IP_j}$$

$$QP_j = AR(\epsilon)D_j \sin(\pi f_{err}T_{PDI} + \theta_{err}) + \eta_{QP_j}$$

$$IE_j = AR(\epsilon + \Delta)D_j \cos(\pi f_{err}T_{PDI} + \theta_{err}) + \eta_{IE_j}$$

$$QE_j = AR(\epsilon + \Delta)D_j \sin(\pi f_{err}T_{PDI} + \theta_{err}) + \eta_{QE_j} \tag{3.2}$$

$$IL_j = AR(\epsilon - \Delta)D_j \cos(\pi f_{err}T_{PDI} + \theta_{err}) + \eta_{IL_j}$$

$$QL_j = AR(\epsilon - \Delta)D_j \sin(\pi f_{err}T_{PDI} + \theta_{err}) + \eta_{QL_j}$$

$$A = \sqrt{2T(C/N_0)} \operatorname{sinc}(\pi f_{err}T_{PDI})$$

$$\eta \sim \mathcal{N}(0, 1)$$

where A defines the signal amplitude scale factor, R is the autocorrelation function of the jth satellite's ranging code, Δ is the magnitude of the replica code phase offset, D_j is the constant data bit value over the integration period, and C/N_0 is the carrier-to-noise density ratio. The variables ϵ, f_{err}, and θ_{err} define the code error in chips, frequency error in Hertz, and phase

error in radians between the locally generated replica and the jth satellite's received signal, respectively. In the case of GPS L1 C/A, the autocorrelation function is defined as

$$R(\epsilon) = \begin{cases} 1 - |\epsilon|, & \text{for } |\epsilon| < 1 \\ 0, & \text{for } |\epsilon| \geq 1 \end{cases} \tag{3.3}$$

Discriminator functions for the DLL and PLL are abundant in the literature, with many being presented in [53]. The difference in these discriminators is their prioritization of efficiency and accuracy. Typically, greater accuracy implies a more significant computational burden, which may be essential to consider for an SDR. However, the following discriminators prioritize accuracy. Equations 3.4 and 3.5 define a commonly used code phase and carrier phase discriminator, respectively, as

$$\hat{\epsilon} = (1 - \Delta)\frac{\sqrt{IE^2 + QE^2} - \sqrt{IL^2 + QL^2}}{\sqrt{IE^2 + QE^2} + \sqrt{IL^2 + QL^2}} \tag{3.4}$$

$$\hat{\theta}_{err} = \arctan\left(\frac{QP}{IP}\right) \tag{3.5}$$

where ˆ indicates these errors are only estimates of the actual errors and Δ is the magnitude of the replica code phase offset. It is worth mentioning that Equation 3.5 is one of the Costas loop discriminators, which are notable for their immunity to phase transitions imparted by a signal's navigation message.

The combination of the six correlators and lock loops can be seen in Figure 3.6 as a complete GNSS tracking loop. For the GPS L1 C/A signal, this tracking loop is considered successful if the resulting values of the in-phase prompt IP_j correlator depict the navigation message for each satellite. Once the beginning of an LNAV sub-frame—described in Section 2.2.3—is found, the data can be decoded and used for navigation. Once again, the reader is referred to [41, 52, 53] for additional information regarding signal tracking.
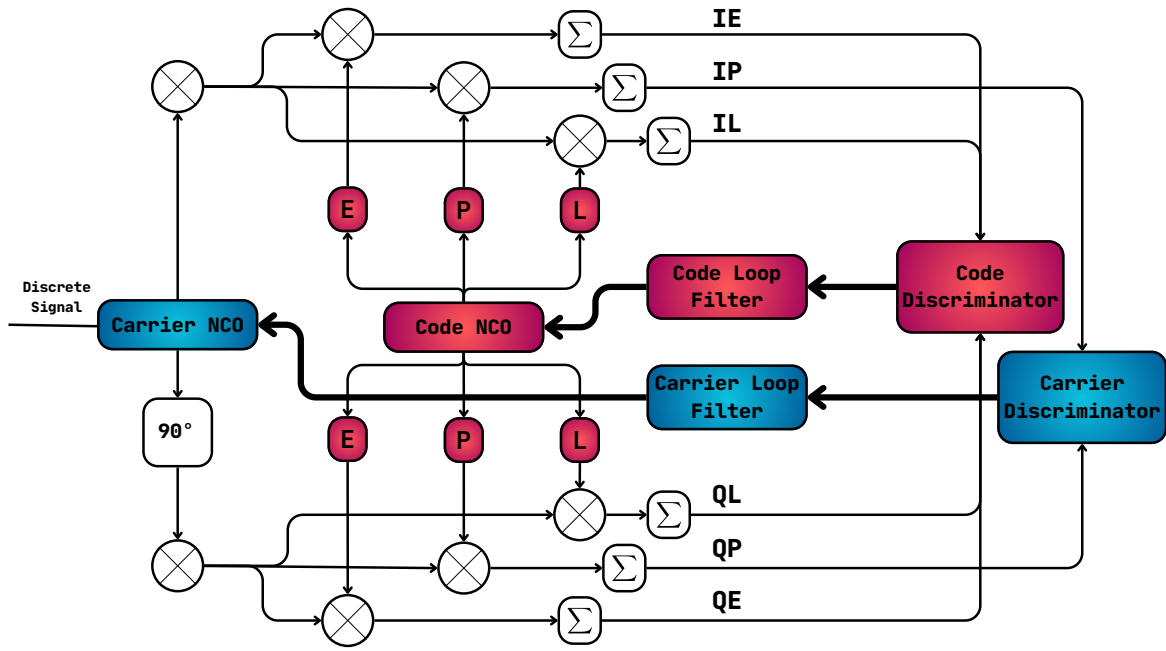
Figure 3.6: Generalized GNSS Tracking Loop

3.1.3 Position, Velocity, and Timing Estimation

Once the received signals are successfully tracked, a conventional GNSS receiver passes measurements of the tracked channels to an estimator (or navigator) to determine the corresponding PVT states. These measurements are called observables and are comprised of the following: pseudoranges, pseudorange rates, and carrier-to-noise density ratios.

Pseudorange Measurements

The pseudorange is the observed transit time of the signal from a transmitting satellite. It is defined as

$$\rho^j = (t_r - t_t^j)c \tag{3.6}$$

where ρ^j is the observed transit time expressed as a range, t_r is the received time, t_r^j is the transmit time of the jth satellite, and c is the speed of light in a vacuum. The pseudorange measurement appears relatively straightforward to obtain, as the transmit time is easily acquired from the navigation message. However, the received time is ambiguous, which requires the

receiver to determine a delta received time using the ranging code instead. Given the transmit time is scheduled and corrected for GNSS, the change in the transmit time for each satellite can be considered constant. This allows the change in transit time to be approximated as

$$\Delta t_k^j = t_k^j - t_{k-1}^j \tag{3.7a}$$

$$\Delta t_k^j = \Delta t_{r_k}^j \tag{3.7b}$$

where t_k^j is the transit time at time k for the jth satellite and $\Delta t_{r_k}^j$ is the change in received time at time k or the jth satellite. Since the change in transit time is known between update periods by measuring the code phase of the ranging code, an initial transit time is all that is needed to begin measuring pseudoranges. This initial transit time can be approximated using knowledge of GNSS orbital altitudes. Assuming an average range of $\sim$20,000 kilometers, the average transit time would be 67 milliseconds. However, given that this approximation is inherently invalid, a different clock bias would be applied to each measurement if this was assumed for all channels, resulting in an unobservable system. This observability issue can be avoided by solely applying the transit time assumption to the closest satellite. This satellite is determined by finding the channel with the earliest decoded navigation message sub-frame. Once the closest satellite is determined, the transit time of every other channel is updated using the time difference of the subsequent decoded sub-frames.

Equation 3.6 is a simplistic representation of the pseudorange measurement as it is just expressed as a function of transit time. However, the transit time is a function of many error sources that must be modeled to achieve the most accurate measurement. These errors are represented in the pseudorange measurement model as

$$\rho^j = r_u^j + c(\delta t_u - \delta t_s^j) + I_u^j + T_u^j + M_u^j + \eta_{\rho^j} \tag{3.8}$$

$$r_u^j = \sqrt{(x_s^j - x_u)^2 + (y_s^j - y_u)^2 + (z_s^j - z_u)^2}$$

where r_u^j is the geometric range from the user u to the jth satellite s, δt_u is the clock bias of the user's receiver, δt_s^j is the clock bias of the jth satellite, I_u^j is the ionospheric delay associated with the user and satellite positions, T_u^j is the tropospheric delay associated with the user and satellite positions, M_u^j is the multi-path delay associated with the user and satellite positions, and η_{ρ^j} is independent, identically distributed Gaussian noise.

Given the model presented in Equation 3.8, it is easy to see why this measurement is called a pseudorange. The geometric range is obscured by transmission path errors of which the receiver has little or no knowledge. More precise solutions can be obtained by removing ionospheric and tropospheric errors with an accurate model [55, 56]. Whether corrected or not, these measurements are used in a trilateration problem to determine a user's position. Traditionally, this requires only three pseudorange measurements. However, the GNSS problem contains a clock bias state imparted by the transit time assumption (i.e., 67 ms) and the receiver's clock dynamics. This requires at least a fourth pseudorange (i.e., received satellite) to estimate a receiver's position and clock states.

Pseudorange Rate Measurements

In addition to positioning, GNSS provides exceptional velocity estimation by measuring the time derivative of the pseudorange. This measurement is called the pseudorange rate and is modeled similarly to Equation 3.8 as

$$\dot{\rho}^j = \dot{r}_u^j + c(\delta \dot{t}_u - \delta \dot{t}_s^j) + \dot{I}_u^j + \dot{T}_u^j + \eta_{\dot{\rho}^j} \tag{3.9}$$

In Equation 3.9, the pseudorange rate $\dot{\rho}^j$ is a function of the delay time derivatives from the pseudorange measurement model, excluding the multi-path delay. The derivatives of these delays are called drifts and can mostly be ignored as they are small or easily modeled. The only exception to this case is $\delta \dot{t}_u$ as the receiver's clock stability is often sacrificed to maintain a low size, weight, power, and cost (SWaP-C) for the user.

The pseudorange rate measurement can be directly extracted from the Doppler shift measured by the receiver on each channel. This measurement of the line-of-sight (LOS) velocity is related to Doppler shift by the following

$$f_d^j = \dot{\rho}^j \frac{f_c}{c} \tag{3.10}$$

where f_c is the center frequency of the transmitted signal. In addition to estimating velocity, this measurement can be integrated to generate an accurate carrier phase measurement that can be converted to a carrier-based pseudorange. This carrier-based pseudorange can provide more precise positioning than code-based pseudoranges, but it is relatively difficult to determine. The difficulty stems from the ambiguous number of carrier signal cycles between the user and the satellite. Although techniques exist for estimating this ambiguity, they are excluded from this thesis as they fall outside its scope.

Carrier-to-Noise Density Ratio

The carrier-to-noise density ratio (C/N$_0$) is a measurement of the ratio of the carrier power and the noise power per unit bandwidth [57]. In other words, C/N$_0$ provides the same type of information as SNR but is independent of the receiver's bandwidth. This measurement can quantify the quality of the measurements mentioned above and is determined using correlators from each channel. This thesis uses Beaulieu's method of determining C/N$_0$, which is given in [58] as the following

$$SNR = \left[\frac{1}{N} \sum_{k=1}^{N} \frac{\hat{P}_{n,k}}{\hat{P}_{c,k}} \right]^{-1} \qquad C/N_0 = \frac{SNR}{T_{PDI}} \tag{3.11}$$

$$\hat{P}_{c,k} = \frac{1}{2} \Big[IP(k)^2 + IP(k-1)^2 \Big],$$
$$\hat{P}_{n,k} = \Big[|IP(k)| - |IP(k-1)| \Big]^2$$

where k indicates the current pre-detection integration period, $\hat{P}_{c,k}$ is the carrier power estimate, $\hat{P}_{n,k}$ is the noise power estimate, and N is the number of pre-detection integration periods to average in the estimation of C/N$_0$.

Navigation State Estimation

Finally, a state estimation technique can determine the PVT states associated with the above-mentioned measurements. The estimated PVT states are defined as

$$\boldsymbol{\gamma} = [x_u, \ \dot{x}_u, \ y_u, \ \dot{y}_u, \ z_u, \ \dot{z}_u, \ c\delta t_u, \ c\delta \dot{t}_u]^T \tag{3.12}$$

where x_u, y_u, and z_u and their derivatives are the user positions and velocities in the Earth-Centered Earth-Fixed (ECEF) reference frame, respectively. The two remaining states are the user clock bias and clock drift. The states in Equation 3.12 are directly related to the pseudorange and pseudorange rate measurements using Equations 3.8 and 3.9 and can be directly estimated if the satellite, atmospheric, and multi-path error sources are omitted. This omission results in reduced state observation models expressed as

$$h(\boldsymbol{\gamma})_{\rho^j} = \sqrt{(x_s^j - x_u)^2 + (y_s^j - y_u)^2 + (z_s^j - z_u)^2} + c\delta t_u \tag{3.13}$$

$$h(\boldsymbol{\gamma})_{\dot{\rho}^j} = (\dot{x}_s^j - \dot{x}_u)a_x^j + (\dot{y}_s^j - \dot{y}_u)a_y^j + (\dot{z}_s^j - \dot{z}_u)a_z^j + c\delta \dot{t}_u \tag{3.14}$$

where a_x^j, a_y^j, a_z^j are the unit vector components from the user to the jth satellite in the ECEF frame.

Conventionally, the Weighted Nonlinear Least Squares (WNLS) estimation technique is used in the GNSS problem. WNLS is necessary because of the nonlinear term that defines the geometric range in Equation 3.13. This term requires Equation 3.13 to be linearized for use in the WNLS observation matrix. The observation matrix (or geometry matrix) for m channels is given by the Jacobian of $h(\boldsymbol{\gamma})$ with respect to each state as

$$\boldsymbol{H} = \begin{bmatrix} a_1^x & 0 & a_1^y & 0 & a_1^z & 0 & 1 & 0 \\ \vdots & \vdots & \vdots & \vdots & \vdots & \vdots & \vdots & \vdots \\ a_m^x & 0 & a_m^y & 0 & a_m^z & 0 & 1 & 0 \\ 0 & a_1^x & 0 & a_1^y & 0 & a_1^z & 0 & 1 \\ \vdots & \vdots & \vdots & \vdots & \vdots & \vdots & \vdots & \vdots \\ 0 & a_m^x & 0 & a_m^y & 0 & a_m^z & 0 & 1 \end{bmatrix} \tag{3.15}$$

where a_m^x, a_m^y, a_m^z are the unit vector components from the mth channel's satellite to the user in the ECEF frame.

The nonlinear nature of trilateration requires an iterative estimation of the error between the actual state and the current estimate of the state. This is accomplished using the residuals of the receiver's measurements with predicted measurements. The resulting measurement residual vector is given as

$$\boldsymbol{z} = [\tilde{\rho}_1 - \hat{\rho}_1, \ \dots \ , \tilde{\rho}_m - \hat{\rho}_m, \ \dot{\tilde{\rho}}_1 - \dot{\hat{\rho}}_1, \ \dots \ , \dot{\tilde{\rho}}_m - \dot{\hat{\rho}}_m]^T \tag{3.16}$$

where the ~ and ˆ indicate a receiver's measurement and a predicted measurement, respectively.

In addition, WNLS utilizes a weighting matrix $\boldsymbol{R}^{-1}$ that is a function of the measured C/N$_0$ for each satellite. This matrix prioritizes measurements from channels with better tracking performance (i.e., higher C/N$_0$) during state estimation. This is accomplished for GPS L1 C/A and similar signals by creating a diagonal measurement covariance matrix using the analytical pseudorange and pseudorange rate residuals given by [59] as

$$\sigma_{\delta\rho}^2 = \frac{\beta^2}{2T_{PDI}^2(C/N_0)^2} + \frac{\beta^2}{4T_{PDI}(C/N_0)} \tag{3.17}$$

$$\sigma_{\delta\dot{\rho}}^2 = K\left(\frac{\lambda}{\pi T_{PDI}}\right)^2\left(\frac{2}{T_{PDI}^2(C/N_0)^2} + \frac{2}{T_{PDI}(C/N_0)}\right) \tag{3.18}$$

$$\boldsymbol{R} = \text{diag}\left([\sigma_{\delta\rho_1}^2, \ \dots \ , \sigma_{\delta\rho_m}^2, \sigma_{\delta\dot{\rho}_1}^2, \ \dots \ , \sigma_{\delta\dot{\rho}_m}^2]\right) \tag{3.19}$$

where β is the ranging code wavelength, λ is the carrier signal wavelength, and C/N_0 is the carrier-to-noise density ratio in dB-Hz.

WNLS updates are conducted with the measurement residuals and the following equations, which are given as

$$\delta\hat{\gamma} = (\boldsymbol{H}^T\boldsymbol{R}^{-1}\boldsymbol{H})^{-1}\boldsymbol{H}^T\boldsymbol{R}^{-1}\boldsymbol{z} \tag{3.20}$$

$$\hat{\gamma}^+ = \hat{\gamma}^- + \delta\hat{\gamma} \tag{3.21}$$

WNLS requires an *a priori* estimate of $\boldsymbol{\gamma}$ to begin its iterative process. This estimate can be provided by another PVT solution or set as a vector of zeros if a previous estimate is unavailable. For greater accuracy, Equation 3.20 can be iterated until $\delta\hat{\gamma}$ is sufficiently small. In addition, the geometry matrix and residual vector must be recalculated upon each iteration using the latest $\boldsymbol{\gamma}$ estimate.

3.2 Vector Processing

The processing stages outlined in Section 3.1 describe the conventional approach to PVT determination that has been used since the inception of GNSS. For decades, this type of processing has proven valuable and efficient in ideal signal conditions. However, the fixed noise equivalent bandwidth tracking loops employed by this approach leave much to be desired. This is because the optimal bandwidth for such tracking loops needs to be known *a priori*, which is nearly never the case. As a result, unnecessary noise can be let into the system, and changes in dynamics can be overlooked, which can prove detrimental to a receiver in a high RFI scenario.

One general approach to tracking GNSS signals with an adaptive bandwidth involves using an Extended Kalman Filter (EKF) [60–62]. An EKF offers adaptive bandwidth determination using the measurement residuals from the code and carrier phase discriminators. However, it still tracks each channel individually, posing robustness issues as signals subjected to harsh transmission paths can be lost without the aid of unaffected signals.

The method of vector processing (VP) improves upon the EKF approach by allowing channels to be processed in aggregate, as illustrated in Figure 3.7. This is accomplished by referencing each channel's local replica to the same PVT estimate. As a result, the adaptive bandwidth filtering benefits of the EKF are combined with the benefits of a filtered navigation solution, allowing for successful tracking of channels with low C/N_0 values. VP has been the standard for advanced receiver architectures for decades; therefore, it is used as a point of comparison for the DPE architectures outlined in this thesis.

Channels
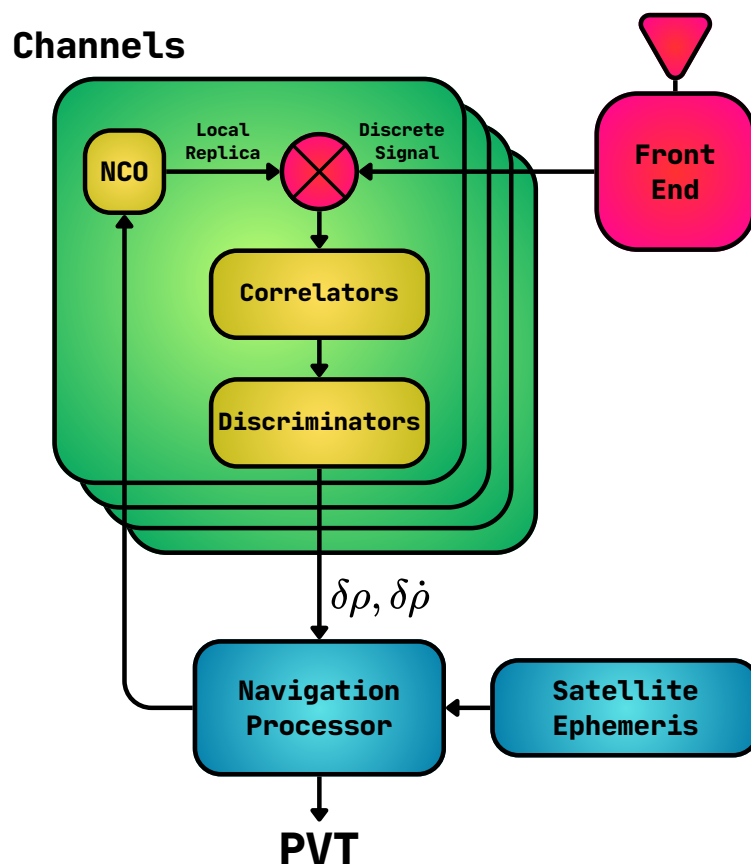
Figure 3.7: Generalized Vector Processing Loop

As an example of VP performance gains, Figure 3.8 compares a VP receiver to a conventional receiver. Specifically, live-sky GPS data was recorded over the course of 18 hours and evaluated using conventional processing and vector processing. It is shown in [54] that the average maximum and minimum vector processing performance gains over this duration were 5.20 dB and 1.54 dB, respectively, when considering each channel's C/N_0. For the performance gain derivations and additional information regarding this study, the reader is referred to

Chapter 6 in [54]. The rest of this section discusses a specific VP architecture called the Vector Delay-Frequency Lock Loop (VDFLL).
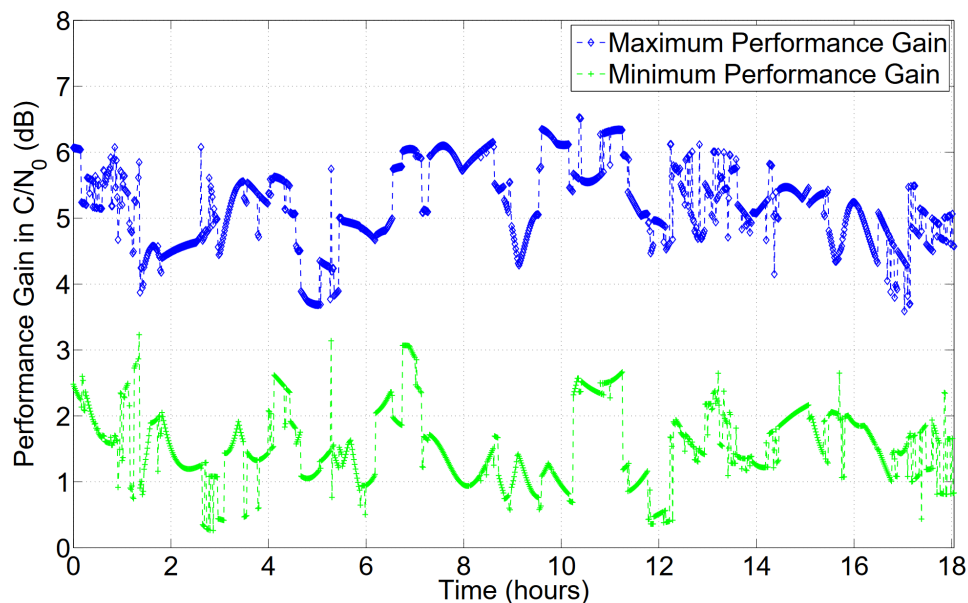
Figure 3.8: Maximum and Minimum Performance Gain in C/N$_0$ from Vector Processing [54]

3.2.1 Vector Delay-Frequency Lock Loop

The origins of the VDFLL can be traced back to the Vector Delay Lock Loop (VDLL) , which was introduced by [63]. The VDLL updates the local replica ranging code frequency with an EKF that jointly estimates the navigation solution. A simple extension of this algorithm, introduced in [64], saw the addition of carrier frequency tracking, creating the modern VDFLL. As a result, the VDFLL has shown great performance gains over conventional tracking methods in scenarios with high dynamics and GNSS RFI [65–67]. The rest of this section outlines the structure of the VDFLL. For more information regarding the VDFLL and additional VP architectures, the reader is referred to [54, 68].

Initialization of a VDFLL requires an *a priori* state estimate from a conventional receiver and each channel's corresponding ephemeris. The state estimate is provided in the same form defined in Equation 3.12 with the units of position indicated in meters, units of velocity indicated in meters per second, clock bias indicated in meters, and clock drift in meters per second. In addition, the initial state estimate is accompanied by a corresponding covariance P_k.

35

Time Update

The dynamic model and process noise covariance propagate the state and covariance in time to the ensuing measurement update. The dynamic model employs a constant velocity assumption and is defined as

$$\hat{\boldsymbol{\gamma}}_{k+1} = \boldsymbol{F}\hat{\boldsymbol{\gamma}}_k \tag{3.22}$$

$$\boldsymbol{F} = \begin{bmatrix} \boldsymbol{A} & 0 & 0 & 0 \\ 0 & \boldsymbol{A} & 0 & 0 \\ 0 & 0 & \boldsymbol{A} & 0 \\ 0 & 0 & 0 & \boldsymbol{A} \end{bmatrix} \qquad \boldsymbol{A} = \begin{bmatrix} 1 & T \\ 0 & 1 \end{bmatrix}$$

where $\boldsymbol{F}$ is the state transition matrix and T is the integration period. The process noise covariance is defined as

$$\boldsymbol{Q} = \begin{bmatrix} \boldsymbol{Q}_x & 0 & 0 & 0 \\ 0 & \boldsymbol{Q}_y & 0 & 0 \\ 0 & 0 & \boldsymbol{Q}_z & 0 \\ 0 & 0 & 0 & \boldsymbol{Q}_{clock} \end{bmatrix} \tag{3.23}$$

$$\boldsymbol{Q}_{xyz} = \begin{bmatrix} \sigma_{xyz}^2 \frac{T^3}{3} & \sigma_{xyz}^2 \frac{T^2}{2} \\ \sigma_{xyz}^2 \frac{T^2}{2} & \sigma_{xyz}^2 T \end{bmatrix} \qquad \boldsymbol{Q}_{clock} = \begin{bmatrix} \sigma_b^2 T + \sigma_r^2 \frac{T^3}{3} & \sigma_r^2 \frac{T^2}{2} \\ \sigma_r^2 \frac{T^2}{2} & \sigma_r^2 T \end{bmatrix}$$

where σ_{xyz}^2 is the variance of the noise processes for the x, y, and z velocity errors in m²/s³, σ_b^2 is the variance of the noise process for the clock phase error in m²/s, and σ_r^2 is the variance of the noise process for the clock frequency error in m²/s³. The σ_{xyz}^2 values are considered tuning parameters that are selected based on the expected dynamics. This selection can be informed by the following given by [69]

$$\delta v_{xyz} \approx \sigma_{xyz}\sqrt{T} \tag{3.24}$$

where δv_{xyz} is the largest expected change in velocity in each direction over an integration period. The clock covariance values σ_b^2 and σ_r^2 for a variety of clock qualities can be found in [70].

Given the above state transition and covariance matrices, the EKF time update is defined as

$$\hat{\boldsymbol{\gamma}}_{k+1}^{-} = \boldsymbol{F}\hat{\boldsymbol{\gamma}}_{i_k}^{+} \tag{3.25}$$

$$\boldsymbol{P}_{k+1}^{-} = \boldsymbol{F}\boldsymbol{P}_k^{+}\boldsymbol{F}^T + \boldsymbol{Q} \tag{3.26}$$

Measurement Update

The model that relates $\boldsymbol{\gamma}$ to the observations is defined as

$$\boldsymbol{y}_k = h(\boldsymbol{\gamma_k}) + \eta_k \tag{3.27}$$

where $\boldsymbol{y}_k$ is the observation vector, h is the nonlinear function that relates the states to the measurements, and η_k is independent, identically distributed Gaussian noise drawn from the covariance $\boldsymbol{R}$ given in Equation 3.19. Once again, the linearized observation matrix given in Equation 3.15 can be used to relate the states to measurement residuals. These measurement residuals are defined in the same manner as Equation 3.16 and can simply be denoted as $\delta\rho_m$ and $\delta\dot{\rho}_m$.

Despite being defined the same way, the $\delta\rho_m$ and $\delta\dot{\rho}_m$ residuals for the VDFLL are obtained in a different manner than explained in Section 3.1.3. In the VDFLL, direct measurements of the pseudoranges and pseudorange rates are not used. Instead, the residuals themselves are directly observable using code phase and Doppler shift discriminators. For the pseudorange residuals, the code phase error output from Equation 3.4 can be converted to a pseudorange error using the respective signal's ranging code wavelength. For the pseudorange

rate residuals, a new discriminator must be defined for the Doppler shift error before it can be converted. A common frequency-tracking discriminator is given as

$$cross = IP_1 QP_2 - IP_2 QP_1$$
$$dot = IP_1 IP_2 + QP_1 QP_2 \tag{3.28}$$
$$\hat{f}_{err} = \frac{\arctan2(cross, dot)}{\pi T}$$

where the prompt correlator subscripts indicate different integration periods. The resulting errors from Equations 3.4 and 3.28 are converted to pseudorange and pseudorange rate residuals using the following

$$\delta \rho_m = \beta \hat{\epsilon} \tag{3.29}$$

$$\delta \dot{\rho}_m = -\lambda \hat{f}_{err} \tag{3.30}$$

where β is the ranging code wavelength and λ is the carrier signal wavelength. For GPS L1 C/A, the corresponding wavelengths are $\beta = 293.05\,\mathrm{m}$ and $\lambda = 0.1905\,\mathrm{m}$.

Given $\boldsymbol{H}$, $\boldsymbol{z}$, and $\boldsymbol{R}$ are defined by Equations 3.15, 3.16, and 3.19, respectively, the EKF measurement update is defined as

$$\boldsymbol{K} = \boldsymbol{P}_{k+1}^{-} \boldsymbol{H}^T (\boldsymbol{H} \boldsymbol{P}_{k+1}^{-} \boldsymbol{H}^T + \boldsymbol{R}) \tag{3.31}$$

$$\hat{\boldsymbol{\gamma}}_{k+1}^{+} = \hat{\boldsymbol{\gamma}}_{k+1}^{-} + \boldsymbol{K} \boldsymbol{z} \tag{3.32}$$

$$\boldsymbol{P}_{k+1}^{+} = (\boldsymbol{I} - \boldsymbol{K} \boldsymbol{H}) \boldsymbol{P}_{k+1}^{-} (\boldsymbol{I} - \boldsymbol{K} \boldsymbol{H})^T + \boldsymbol{K} \boldsymbol{R} \boldsymbol{K}^T \tag{3.33}$$

where $\boldsymbol{I}$ is the identity matrix.

Chapter 4

Direct Position Estimation and Proposed LEO Augmentation

This chapter presents Direct Position Estimation (DPE) as an alternative to the conventional and vector processing techniques discussed in Chapter 3. Introduced for GNSS in [29], DPE aims to overcome some of the critical challenges of traditional PNT processing techniques by directly computing a PVT solution from a sampled signal. The techniques offered in Chapter 3 differ from DPE as they operate in two consecutive steps, classifying them as two-step architectures. The first step generates intermediate measurements of each received signal's parameters with tracking loops. Then, these measurements are used in a navigation filter by the second step, which estimates the corresponding PVT solution, as described in Figure 4.1.

CONVENTIONAL TWO-STEP APPROACH

STEP ONE

ESTIMATE
CHANNEL
OBSERVABLES

STEP TWO

FUSE
OBSERVABLES
IN NAVIGATION
FILTER
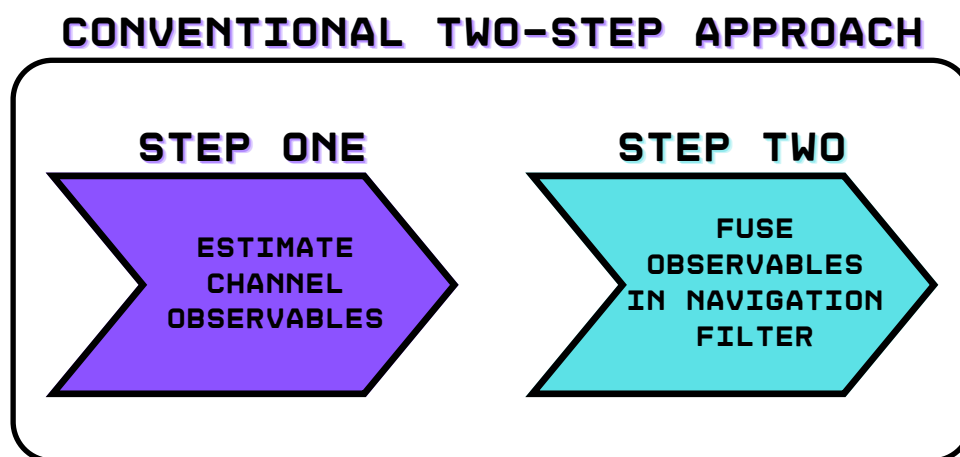
Figure 4.1: Conventional Two-Step Receiver Approach

For conventional and vector processing architectures, the intermediate measurements are recorded across independently processed channels. If subjected to degraded signal conditions (e.g., a high RFI scenario), these measurements are often rejected by the ensuing navigation filter update through covariance weighting or fault detection and exclusion (FDE). Alternatively, DPE can preserve the information from these degraded measurements and perform better in more challenging conditions than two-step architectures [71] with the approach described by Figure 4.2. The rest of this chapter introduces the principles of DPE and discusses two methods for augmenting a GNSS DPE architecture with LEO PNT sources.

DPE ONE-STEP APPROACH

GENERATE CORRELATOR MANIFOLD

STEP ONE

MAXIMIZE CORRELATOR MANIFOLD
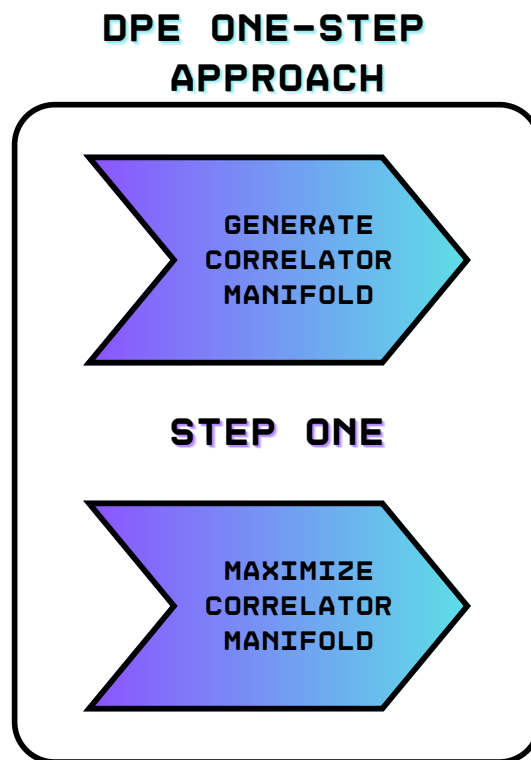
Figure 4.2: DPE One-Step Receiver Approach

4.1   Direct Position Estimation

The central idea of DPE lies in understanding that the time delays (i.e., code phases) and Doppler shifts of all GNSS signals are directly coupled through a receiver's state γ, which is defined in Equation 3.12. As a result of being received at the same time and location, GNSS

signals can be directly processed in a single step to bypass the generation of measurements for each channel. In essence, this is done by selecting a collection of candidate receiver states, generating a local signal replica for each candidate, and determining which states maximize the replica and signal correlation.

Observing the measurement models in Equations 3.8, 3.9, and 3.10, the time delay and Doppler shift can be identified as $\tau \triangleq \tau(\boldsymbol{\gamma})$ and $f_d \triangleq f_d(\boldsymbol{\gamma})$, respectively, assuming the satellite states and atmospheric errors are known. For this reason, the PVT states represented by $\boldsymbol{\gamma}$ can directly generate every satellite's replica without explicitly estimating τ and f_d. This notion is used in vector processing as explained in Chapter 3. However, it can be further exploited to perform a simultaneous joint optimization of all received signal CAFs instead of optimizing on a channel-by-channel basis. This idea of joint optimization is further communicated in the following theoretical overview of DPE.

4.1.1 Theoretical Overview

Consider a subset of N received complex signal samples $\boldsymbol{y} = [y_0, \ \ldots \ , y_{N-1}]^T$. If M satellites are received, then $\boldsymbol{y}$ may be represented as the sum of their respective signals and thermal noise with the following

$$\boldsymbol{y} = \sum_{i=0}^{M-1} a_i \boldsymbol{d}_i + \boldsymbol{\eta} \tag{4.1}$$

where a_i is the amplitude of signal i and $\boldsymbol{d}_i$ is the modulated signal data, excluding the navigation message. For GNSS, this data comprises ranging codes and phase reversals due to satellite and receiver relative motion and clock errors. In addition, $\boldsymbol{\eta}$ is a noise vector of independent, identically distributed Gaussian noise with variance $\sigma_{\boldsymbol{\eta}}^2$. For clarity, Equation 4.1 can be expressed as

$$\boldsymbol{y} = \boldsymbol{D}\boldsymbol{a} + \boldsymbol{\eta} \tag{4.2}$$

where $\boldsymbol{D} = [\boldsymbol{d}_0, \ \ldots \ , \boldsymbol{d}_{M-1}]$ and $\boldsymbol{a} = [a_0, \ \ldots \ , a_{M-1}]^T$. Regarding two-step architectures, each signal $\boldsymbol{d}_i$ is tracked individually and used in the geometric problem discussed in Section 3.1.3

to estimate $\boldsymbol{\gamma}$. In contrast, DPE exploits the fact that $\boldsymbol{D}$ is a function of $\boldsymbol{\gamma}$, allowing for the maximum likelihood estimation (MLE) of $\boldsymbol{\gamma}$ using Equation 4.2 and the following Gaussian probability density function

$$p(\boldsymbol{y} \mid \boldsymbol{\gamma}, \boldsymbol{a}, \sigma_{\boldsymbol{\eta}}) = (2\pi\sigma_{\boldsymbol{\eta}}^2)^{-\frac{N}{2}} \exp\left(-\frac{1}{2\sigma_{\boldsymbol{\eta}}^2} \|\boldsymbol{y} - \boldsymbol{D}(\boldsymbol{\gamma})\boldsymbol{a}\|^2\right) \tag{4.3}$$

Using Equation 4.3, the MLE of $\boldsymbol{\gamma}$ and $\boldsymbol{a}$ can be performed with the following given by [29]

$$\hat{\boldsymbol{\gamma}}, \hat{\boldsymbol{a}} = \arg\min_{\boldsymbol{\gamma},\boldsymbol{a}} \left\{\|\boldsymbol{y} - \boldsymbol{D}(\boldsymbol{\gamma})\boldsymbol{a}\|^2\right\} \tag{4.4}$$

Considering the case where the correlation between any two signals is minimal, it is assumed $\boldsymbol{d}_i^H \boldsymbol{d}_j = 0$, where $i \neq j$ and H denotes the Hermitian transpose. As a result of this assumption, the MLE for $\boldsymbol{\gamma}$ may be reformulated as the following given by [72]

$$\hat{\boldsymbol{\gamma}} = \arg\max_{\boldsymbol{\gamma}} \left\{\|\boldsymbol{D}^H(\boldsymbol{\gamma})\boldsymbol{y}\|^2\right\} \tag{4.5}$$

where $\boldsymbol{a}$ is considered constant for the subset of received samples.

4.1.2 DPE for GNSS Signals

Understanding how the previous section's theoretical overview directly applies to GNSS signals is critical. For this reason, Equation 4.5 is alternatively defined using the complex baseband received signal model for M GNSS satellites. This model assumes a DSSS signal structure and is described as

$$s(t) = a_i s_i(t - \tau_i) \exp(2\pi j f_{d_i} t) + \eta(t) \tag{4.6}$$

where $s_i(t)$ is a navigation signal spread by the ranging code of the ith satellite, a_i is its complex amplitude, τ_i is the time delay, f_{d_i} is the Doppler shift, and $\eta(t)$ is zero-mean AWGN with variance $N_0/2$, where N_0 is an assumed noise density for all channels.

Given the model in Equation 4.6, the MLE for each received channel's τ and f_d can be represented as the following given by [73]

$$\hat{\tau}_i, \hat{f}_{d_i} = \arg \max_{\tau_i, f_{d_i}} \left\{ \frac{1}{N_{nc}} \sum_{k=0}^{N_{nc}-1} \left| \int_{t_k}^{t_{k+1}} s(t) s_i(t - \tau_i) \exp(-2\pi j f_{d_i} t) \right|^2 \right\} \tag{4.7}$$

$$t_k = k T_{code} N_c$$

$$t_{k+1} = (k + 1) T_{code} N_c$$

where T_{code} is the ranging code duration, N_c is the number of coherently integrated ranging code periods, and N_{nc} is the number of non-coherently averaged CAFs resulting from the coherent integrations. The objective function within the braces of this MLE is referred to as $\Lambda_i(\tau_i(\gamma), f_{d_i}(\gamma), N_c, N_{nc})$ for convenience.

Using the MLE for τ and f_d in Equation 4.7, the MLE for γ in Equation 4.5 can be rewritten as

$$\hat{\gamma} = \arg \max_{\gamma} \left\{ \sum_{i=1}^{M} \Lambda_i(\tau_i(\gamma), f_{d_i}(\gamma), N_c, N_{nc}) \right\} \tag{4.8}$$

where M is the number of received satellites, and the argument is the objective function for γ. In practice, Equation 4.8 is realized by maximizing a manifold defined by the summation of each received channel's objective function—i.e., $\Lambda_i(\tau_i(\gamma), f_{d_i}(\gamma), N_c, N_{nc})$—for a selection of strategically placed γ candidates. Figure 4.3 illustrates an example of this manifold for γ candidates whose position states vary across the local North-East plane. The resulting correlation power for each candidate has been scaled to unity and is referred to as a weight. It can be seen that the most likely estimate for this example is located at the center of this plane.

In this thesis, an alternate definition for the objective function in Equation 4.8 is used to preserve carrier phase information in the summation across each channel. This preservation allows for more precise positioning at the cost of initialization robustness. The definition of this alternative excludes the use of non-coherent CAF averaging N_{nc} and is given as
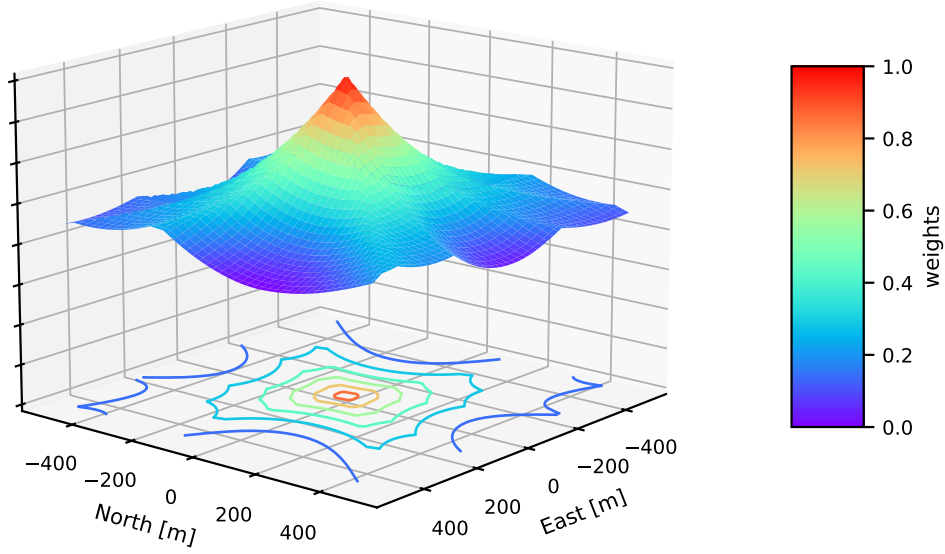
Figure 4.3: Example DPE Manifold

$$\mathbf{\Omega} = \left| \sum_{i=1}^{M} \int_{t_k}^{t_{k+1}} s(t) s_i(t - \tau_i) \exp(-2\pi j f_{d_i} t) \right|^2 \tag{4.9}$$

$$t_k = k T_{code} N_c$$

$$t_{k+1} = (k+1) T_{code} N_c$$

with its corresponding MLE for $\boldsymbol{\gamma}$ defined by

$$\hat{\boldsymbol{\gamma}} = \arg \max_{\gamma} \{\mathbf{\Omega}\} \tag{4.10}$$

The objective function in Equation 4.9 differs from $\sum_{i=1}^{M} \mathbf{\Lambda}_i(\tau_i(\gamma), f_{d_i}(\gamma), N_c, N_{nc})$ as it sums the correlators for each channel before computing the correlation power (i.e., $|\ |^2$). This order of operations maintains correlator-based carrier phase information for each channel,

effectively reducing the peak variance seen in Figure 4.3. The relative precision between code-based and carrier-based pseudoranges explains this reduction in variance despite not being measured in DPE. As with the carrier-based pseudorange, the carrier signal's shorter wave-length offers higher precision than the ranging code in the resulting manifold. However, the issue of carrier phase ambiguity must still be considered.

Carrier phase ambiguity stems from the fact that a receiver can only measure the fractional phase of a signal's most recently received carrier cycle. As a result, the remaining integer number of cycles N to the satellite is unknown. In the case of DPE, carrier phase ambiguity manifests itself as multiple peaks in the manifold resulting from the candidate γ evaluations of Equation 4.9. Specifically, each peak indicates where the cosine function argument in the correlator model from Equation 3.2 is zero. The presence of multiple peaks would seemingly reduce overall certainty when maximizing the manifold, but this is not true. This is because Equation 4.9 still considers code-based information, utilizing the relationship seen in Figure 4.4. In this figure, the low relative precision but absolute ranging nature of the code can aid in resolving the carrier-based range's ambiguity. This aiding is evident as the probability density of the combined range provides a precise and absolute maximum, unlike the carrier-based range. It should be noted that many local maxima still exist in the combined case, but can be avoided in DPE if initializing with an accurate estimate of γ. In addition, the presence of code/carrier divergence is ignored.

Figure 4.5 illustrates an example manifold that retains carrier phase information for the same scenario depicted in Figure 4.3. The reader should note the large difference in scale between these two manifolds. Figure 4.5 is drastically zoomed in to include the absolute maximum and a few local maxima that would be difficult to see because of the centimeter-scale wavelengths of L-band carrier signals.

4.1.3 Practical Considerations

DPE's one-step approach is proven to estimate γ with asymptotically lower, or equal, mean square errors than two-step architectures [74, 75]. However, this comes at the potential cost of being computationally prohibitive. This is because a signal replica must be generated and

45
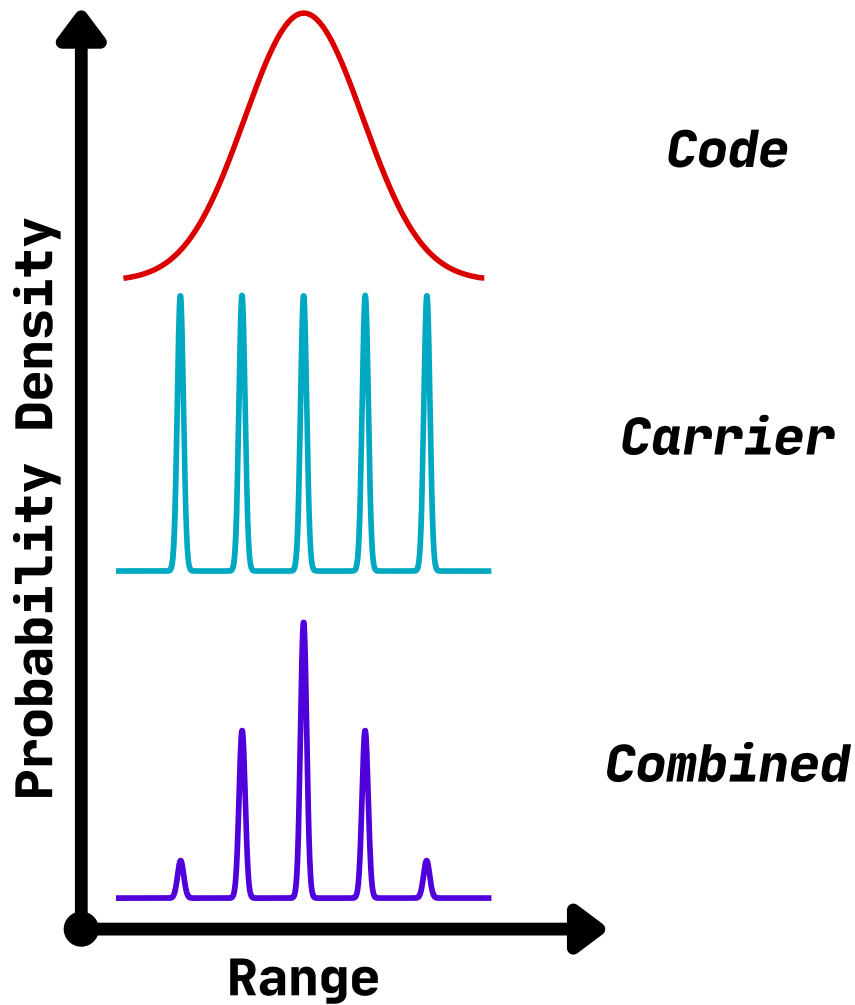
Figure 4.4: Combined Code and Carrier Phase Probability Density

correlated for every candidate. Compared to two-step methods, DPE could potentially require orders of magnitude more correlations depending on its configuration. However, the recent advancement of digital signal processing hardware has significantly increased the computational efficiency of GNSS receivers [76], paving the way for resource-intensive architectures like DPE. Specifically, the use of GPUs for parallelization has been applied to DPE [37] and other architectures for computational performance increases [77–79]. The next section discusses the general DPE architecture used in this thesis and details how LEO PNT sources can be included to increase DPE performance.
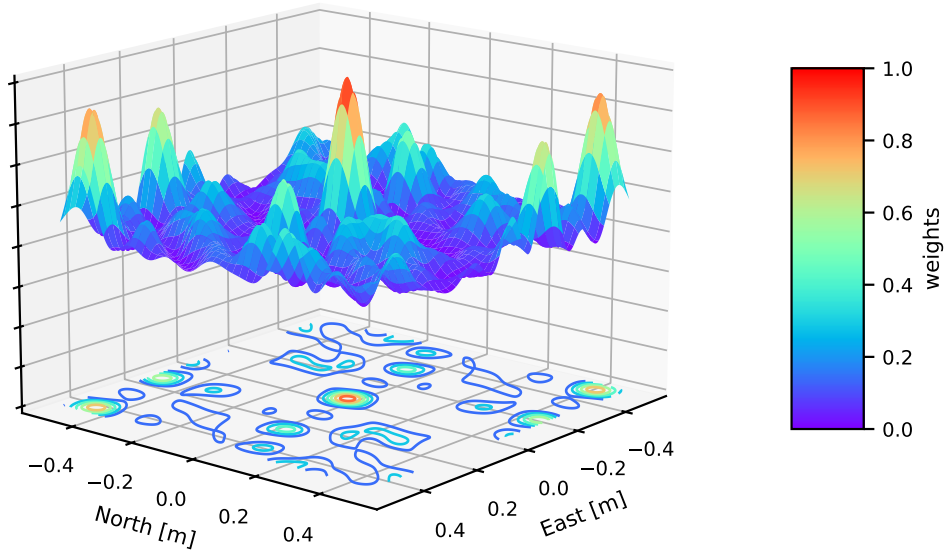
Figure 4.5: Example DPE Manifold with Carrier Phase Information

4.2 Proposed LEO Augmentation

As discussed in Chapter 1, this thesis explores the combination of DPE and LEO PNT to increase the performance of GNSS in high RFI scenarios. Specifically, two types of LEO augmentation sources are considered to acknowledge current and future capabilities. This section first looks to the future by explaining how a dedicated LEO PNT source can be integrated into a GNSS DPE architecture. Then, this integration is slightly modified to consider current opportunistic LEO PNT capabilities.

4.2.1 General Architecture

The proposed LEO-aided GNSS DPE architectures offered in this thesis are derived from the architecture presented in [38] and [39]. This architecture employs a Bayesian approach to DPE for added robustness. Specifically, the architecture is implemented as a Sequential Monte Carlo method or particle filter, as it is commonly known. This architecture was chosen, among others, for its high sensitivity to multi-modal probability distribution (i.e., manifolds), such as

those produced by Equation 4.3. For information regarding other iterative or grid-based DPE approaches, the reader is referred to the survey provided by [37].

Figure 4.6 illustrates the Sequential Importance Resampling (SIR) particle filter algorithm used by the abovementioned architecture. This algorithm is described for a single GNSS constellation as follows.
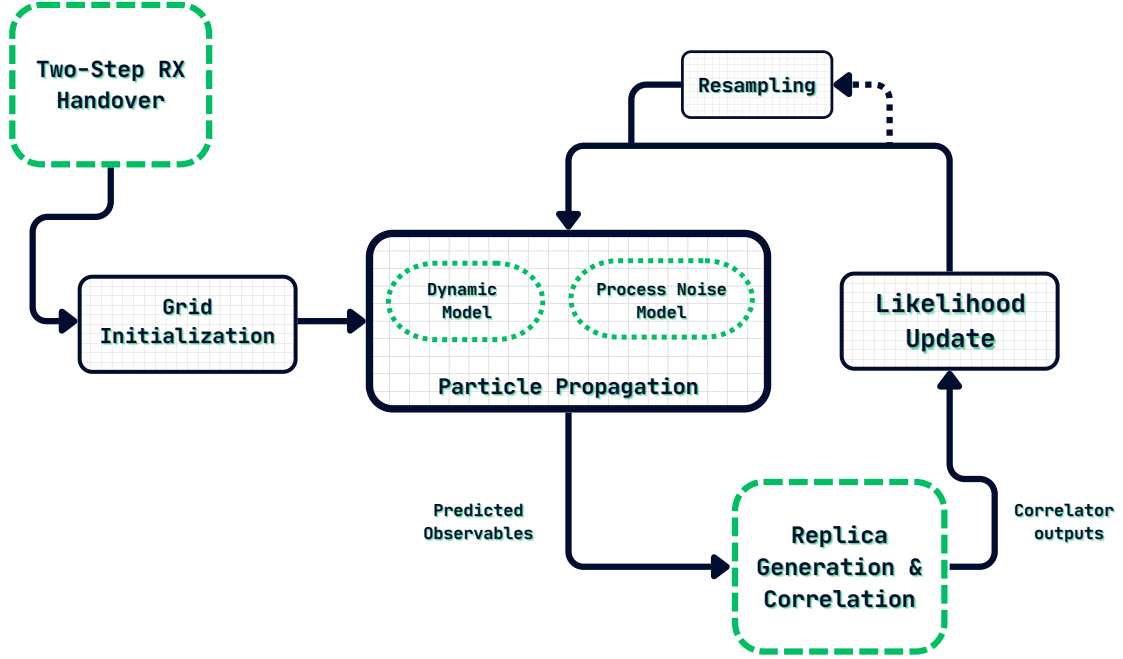
Figure 4.6: DPE Sequential Importance Resampling Particle Filter Architecture

Initialization

First, a grid of uniform particles representing γ candidates is centered at a two-step receiver's current estimate. Along with an initial state estimate, a two-step receiver handover process provides the necessary satellite ephemerides and data message synchronization for each channel. The initial grid is chosen to evenly spread particles around the current estimate, with its bounds based on the maximum expected errors in the τ and f_d domains for any given channel [39]. The grid spacing in each domain is defined by a user-specified standard deviation whose ± 3-σ values serve as the bounds. For the architectures in this thesis, a $\sigma_\tau = 15\,\text{m}$ and $\sigma_{f_d} = 3\,\text{m/s}$ were chosen with an initial resolution of 0.075 in their respective units. When transformed to the γ domain, this grid corresponds to 1201 particles for the position and clock bias states, with

1200 spread around a single particle at the current estimate. The resulting velocity and clock drift states are then interpolated to match the number of position and clock bias particles.

Time Update

Next, a dynamic model and process noise covariance propagate the particles in time to the ensuing likelihood update. The specific model and covariance used in this architecture are the same as those defined for the VDFLL in Equations 3.22 and 3.23, respectively. Once again, the dynamic model employs a constant velocity assumption. In addition, it should be noted that choosing an accurate process noise covariance is essential to preventing sample impoverishment over time [80] as random noise samples are added to each particle. In general, [80] is an excellent source for understanding the principles and limitations of modern particle filters.

Likelihood Update

After propagation, the particle states and satellite ephemerides are used to predict the observables (i.e., pseudoranges and pseudorange rates) that inform each candidate's corresponding correlator value. In practice, these values are obtained by correlating the received signal with the local replicas described by the predicted observables. Then, Equation 4.9 is employed to produce the objective function or manifold. For the rest of this thesis, this method will be called direct summation.

The manifold resulting from direct summation is normalized to create a likelihood function that weighs each particle. The resulting weights determine the new state estimate through a weighted sum of all particle states. The particles and weights are also used to determine the sample covariance associated with this estimate. After updating the state, the number of effective particles is computed and compared to a threshold, determining whether the particles need resampling. The resampling algorithm used in this thesis is called Multinomial Resampling and is detailed in [81]. Finally, the entire process is repeated over subsequent coherent integration periods. For more information on this architecture, the reader is referred to [38, 39].

LEO Augmentation Considerations

The general architecture outlined in this section provides a useful approach for GNSS DPE but needs to be modified to accommodate LEO augmentation. For dedicated LEO PNT sources, it is assumed this augmentation will be performed at the signal level for the best performance. However, this introduces a power obfuscation issue. Essentially, the higher received power of LEO sources (i.e., $\sim 30\,$dB stronger) renders all GNSS information inconsequential by drastically increasing the relative weight of LEO in the generated objective function. This result is notably problematic in scenarios with less than four LEO satellites, like those presented in Chapter 6.

Alternatively, an additional likelihood update is needed for opportunistic LEO sources whose Doppler shift can be measured. Fortunately, this update is relatively easy to include for a SIR particle filter. However, slight modifications to this update are necessary to aid when using a minimal number of candidate particles.

4.2.2   Dedicated LEO PNT Modifications

Direct summation provides a manifold that can be used to successfully estimate γ for standalone GNSS scenarios. However, it shows diminished performance when augmented with dedicated LEO PNT signals. Specifically, this performance reduction is a product of the high received power of LEO signals. Although it seems counterintuitive, this observation can be easily explained.

When combining correlators across channels, those from LEO signals will dominate the resultant sum because their magnitudes are much greater than those from GNSS. This is apparent when inspecting the definition of A in the correlator model given by Equation 3.2. As a result, the information provided by GNSS correlators is less influential in the estimate of γ. The obfuscation of GNSS information can be seen as an ambiguous manifold in Figure 4.7 for a direct summation LEO-aided GNSS scenario. It should be noted that the scenario depicted by this manifold utilizes less than four LEO satellites per likelihood update. Compared to Figure

4.5, it can be seen that higher-powered signals can conceal any refining information gained from lower-powered signals.
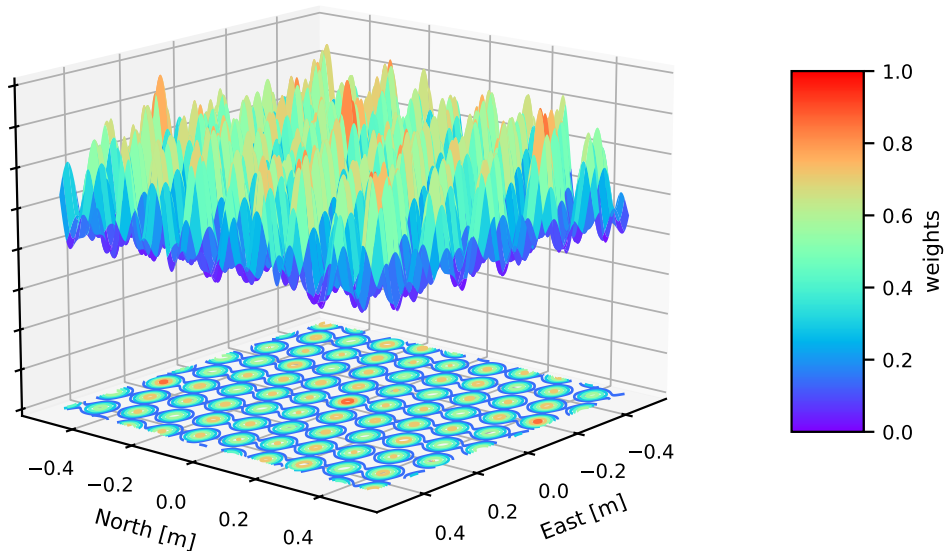
Figure 4.7: Direct Summation Manifold for a GNSS-LEO Scenario

Despite seeming complicated, this issue is relatively straightforward to address. Direct summation manifolds can be generated for each constellation and multiplied to produce a composite likelihood that doesn't obfuscate GNSS. This combination is possible given each direct summation manifold is an independently observed likelihood function. The rest of this thesis refers to this method as Likelihood Combination. Further, it is defined as follows

$$\Gamma = \prod_{i=1}^{L} [\mathbf{\Omega}_i] \tag{4.11}$$

where Γ becomes the new argument in Equation 4.10, and L is the number of considered constellations. An example of this combination is shown in Figure 4.8, where the benefits of high-powered LEO signals are clear in the reduced peak variance compared to the manifold in Figure 4.5.
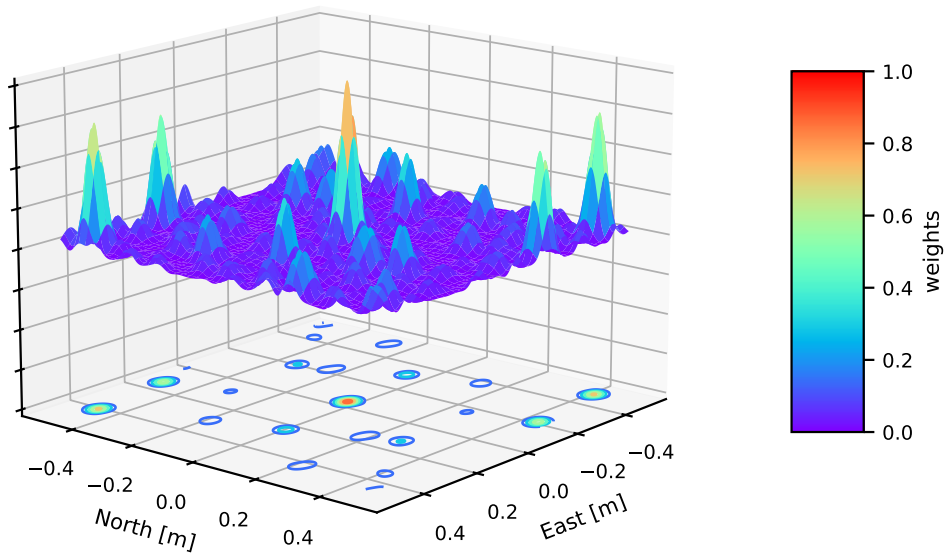
Figure 4.8: Likelihood Combination Manifold for a GNSS-LEO Scenario

The advantages of dedicated LEO PNT augmentation can also be seen in Figures 4.9 and 4.10. In these scenarios, GPS signals are subjected to 25 dB of nominal C/N_0 attenuation to simulate a high RFI environment. Specifically, these signals are received at C/N_0 values around 22 dB-Hz, where signals in ideal conditions are received near 47 dB-Hz. It is assumed that the LEO signals are not subjected to any attenuation given their relative power.

Once again, the reduction in manifold peak variance indicates the performance gain provided by LEO augmentation. In addition, less than 4 LEO satellites are available in the scenario depicted by Figure 4.10, which communicates that the degraded GPS signals are still being used. Otherwise, the resulting manifold would look similar to Figure 4.7, where the standalone LEO solution would be underdetermined.
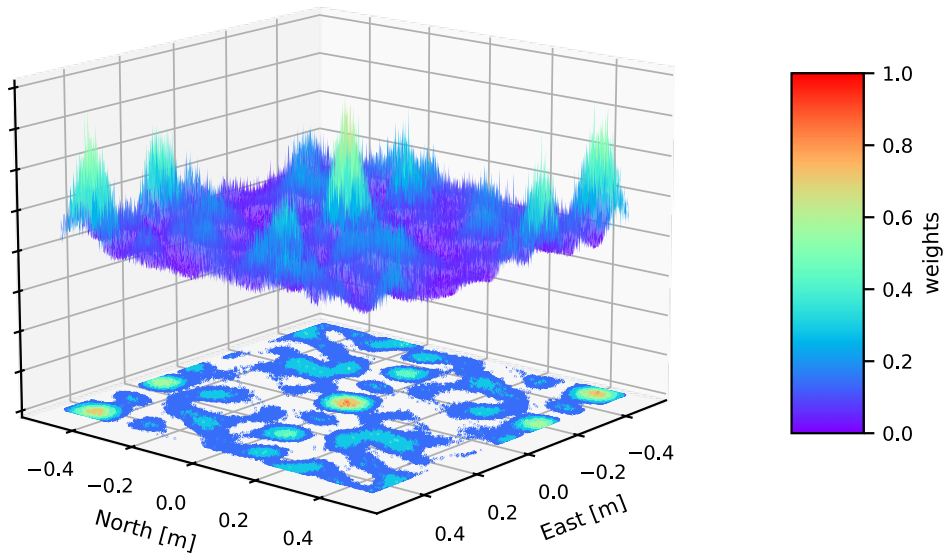
Figure 4.9: DPE Manifold for a GPS High RFI Scenario
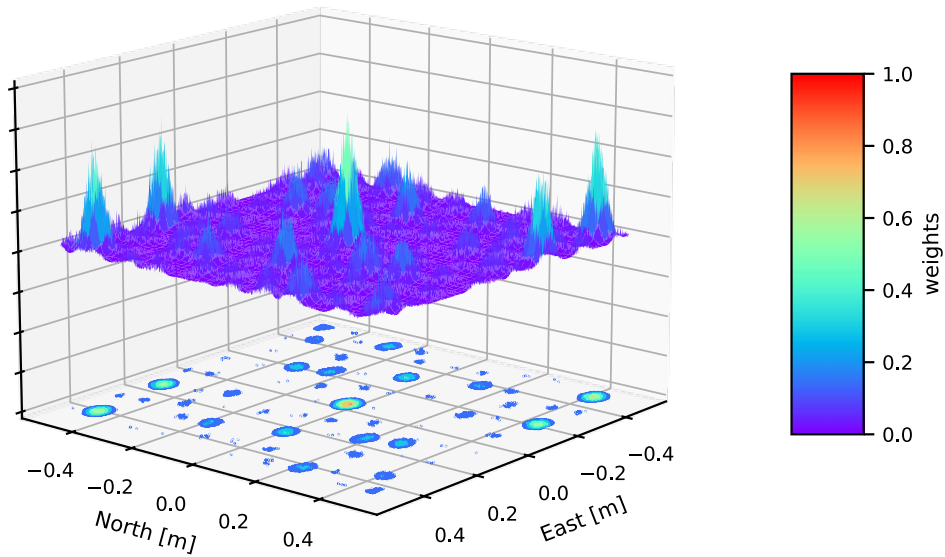
Figure 4.10: DPE Manifold for a GPS-LEO High RFI Scenario

4.2.3 Opportunistic LEO PNT Modifications

For opportunistic LEO PNT sources, an additional likelihood update is needed in the SIR particle filter to consider Doppler shift measurements. This new update is necessary because the DPE likelihood update is conducted at the signal level. In other words, the update requires full knowledge of each received signal's structure to produce the correlators that construct a likelihood manifold. Theoretically, opportunistic LEO signal structures can be inferred to allow for traditional correlation [13, 14]; however, these blind tracking methods are outside the scope of this thesis. Instead, it is assumed that Doppler shift measurements are provided through some means of carrier frequency tracking or snapshot identification.

Unlike the previous section, the likelihood update used for Doppler shift measurements is common in a particle filter architecture. Specifically, it is conducted with the exponential term of a Gaussian probability density function, like the one shown in Equation 4.3. For the Doppler shift update, this exponential term can be rewritten as

$$p(z \mid \boldsymbol{\gamma}, \sigma_z) = \exp\left(-\frac{1}{2\sigma_z^2}[z - h(\boldsymbol{\gamma}^j)]^2\right) \tag{4.12}$$

where z is a single opportunistic Doppler shift measurement, σ_z is the variance of that measurement, and $h(\boldsymbol{\gamma}^j)$ is the function that relates the jth particle's $\boldsymbol{\gamma}$ to the measurement. In this case, $h(\boldsymbol{\gamma}^j)$ is equivalent to Equation 3.14 when z is converted to a pseudorange rate.

During a Doppler shift update, Equation 4.12 is applied to each candidate particle. The resulting density is the assumed likelihood associated with each particle. Then, the weights of the particles are updated with the following

$$\omega_{k+1}^j = \omega_k^j \, p(z \mid \boldsymbol{\gamma}, \sigma_z) \tag{4.13}$$

where ω_k^j is the weight associated with the jth particle at time k. In the same manner as the DPE likelihood update, these weights are normalized before being used in a weighted sum to estimate $\boldsymbol{\gamma}$ for the current time step.

In the case of a minimal number of particles, the σ_z in Equation 4.12 must be modified to reduce the chance of sample impoverishment. Although the time update's process noise covariance attempts to reduce this effect, it is inadequate. The idea of sample impoverishment occurs when all particles are effectively resampled onto a single, highly-weighted particle. Using Equation 4.12, sample impoverishment can occur if σ_z is too small, solely producing a significant likelihood for one particle. Specifically, this hyper-focused weighting is possible when the current states for the majority of particles are not within $\pm 3\sigma_z$, after σ_z has been converted to the γ domain. This can be visualized in Figure 4.11 where the Gaussian resulting from an accurate σ_z heavily weighs one particle, causing sample impoverishment.

Sample Impoverishment
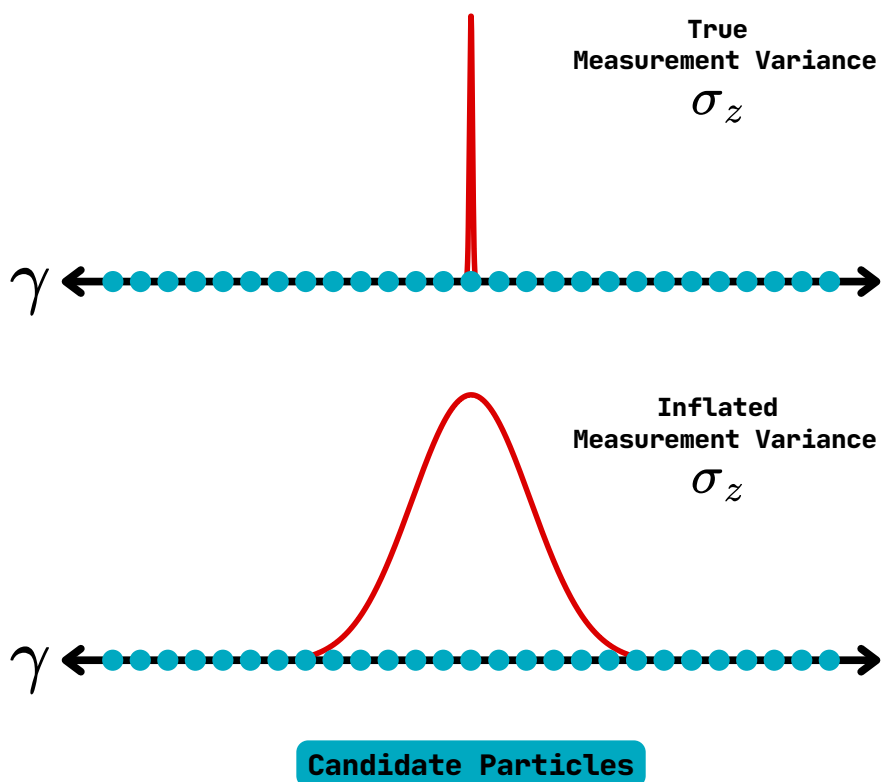
Figure 4.11: Likelihood Update and Sample Impoverishment Relationship

In the case of the proposed architecture, 1201 particles are not enough to prevent sample impoverishment when an accurate σ_z is used. Therefore, σ_z is inflated to the variance of the

predicted pseudorange rates for all particles after converting them to Doppler shifts. This inflation is also visualized in Figure 4.11. Unfortunately, this inflation degrades the theoretical performance of a particle filter with infinite particles. However, it prevents sample impoverishment in a particle filter with a sub-optimal number of particles and allows for continued aiding from opportunistic LEO sources. The performance of this opportunistic aiding is detailed for specific scenarios in Chapter 6.

Chapter 5

Simulation Environment

Assessing the proposed DPE architectures in this thesis requires an environment capable of simulating GPS L1 C/A, dedicated LEO PNT signals, and opportunistic LEO PNT signal measurements. For this reason, a Python library called Navsim was developed. In essence, Navsim allows users to simulate multiple constellations and their measurements for various RFI scenarios. This chapter overviews the Navsim environment and explains its additional capabilities by describing its primary modules—the satellite emitter module, measurement-level simulation module, and correlator-level simulation module. Figure 5.1 illustrates Navsim's general architecture.

Figure 5.1: Navsim Environment Architecture

5.1 Satellite Emitter Module

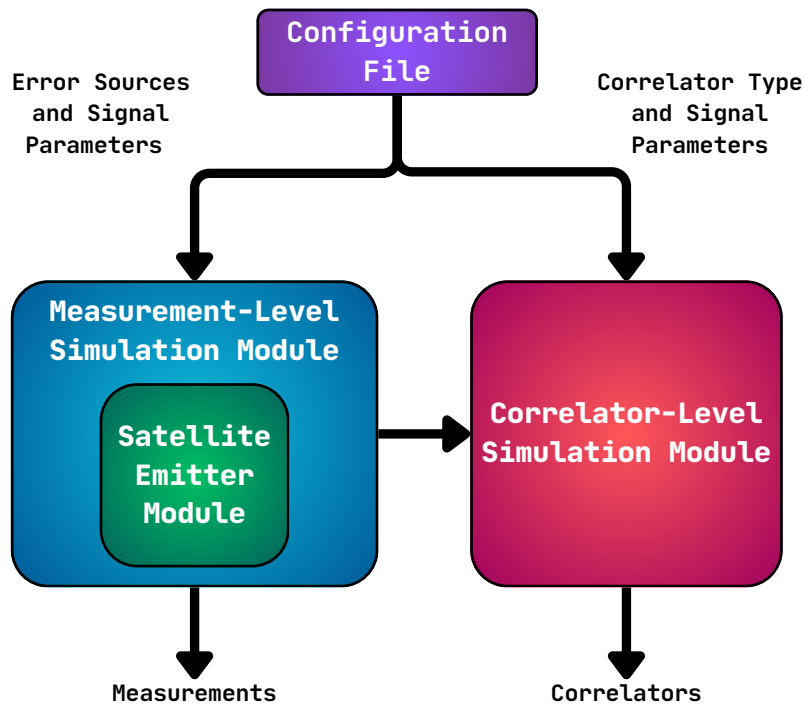The satellite emitter module is the foundation of Navsim. It allows a user to simulate the orbital states for most GNSS and a selection of broadband LEO constellations. Navsim's supported constellations are listed in Table 5.1.

Table 5.1: Navsim's Supported Constellations

GNSS		Broadband LEO	
🇺🇸	GPS	iridium	Iridium NEXT
🇪🇺	Galileo	STARLINK	Starlink
🇷🇺	GLONASS	ORBCOMM	Orbcomm
🇨🇳	BeiDou	Globalstar	Globalstar
🇯🇵	QZSS	EUTELSAT ONEWEB	OneWeb

Currently, the satellite emitter module depends upon two Python libraries to produce the orbital states of a simulated constellation. The first library was developed by Comma.ai and is called Laika [82]. Laika is intended to be used as an end-to-end GNSS measurement processing library for fusion algorithm development, but Navsim only uses a subset of its features. One of these features is the ability to retrieve the satellite states for the GNSS shown in Table 5.1. Laika does this by downloading the Extended Standard Product 3 (SP3) precise ephemeris [83] for a selected GNSS and propagating each satellite's states in time for a specified day, duration, and update rate. This propagation is performed with the user satellite position and velocity algorithms specified in [50].

The propagation of the broadband LEO constellations is accomplished with the second library called Skyfield [84]. Skyfield is generally used for locating celestial bodies but can also determine states for Earth satellites. This feature utilizes Two-Line Element (TLE) ephemeris sets for selected constellations and the Simplified General Perturbations 4 (SGP4) propagation

model [85]. Like Laika, Skyfield can simulate these states for a specified day, duration, and update rate.

The satellite emitter module is contained in a Python class with a simple interface called `SatelliteEmitters`. At initialization, this class accepts the name of the constellations to simulate and a desired mask angle. Then, the user can call a method that accepts a list of Python datetime objects, an array of receiver positions, and an array of receiver velocities to simulate a duration of time. This method is called `from_datetimes()`. The datetimes this method accepts inform the satellite propagation for the abovementioned libraries, while the receiver states allow the calculation of LOS range and range rate observables. Specifically, once the method is called, the satellite ECEF position and velocity states are returned to the user in a list with their corresponding reference observables. These reference observables are calculated with the following

$$r_u^j = \sqrt{(x_u - x_s^j)^2 + (y_u - y_s^j)^2 + (z_u - z_s^j)^2} \qquad (5.1)$$

$$a_{xyz}^j = \frac{[(x_u - x_s^j), (y_u - y_s^j), (z_u - z_s^j)]}{r_u^j} \qquad (5.2)$$

$$\dot{r}_u^j = (\dot{x}_u - \dot{x}_s^j)a_j^x + (\dot{y}_u - \dot{y}_s^j)a_j^y + (\dot{z}_u - \dot{z}_s^j)a_j^z \qquad (5.3)$$

where r_u^j is the true geometric range to each satellite in meters and $\dot{r}_u^j$ is the true range rate for each satellite in meters per second. In addition, x_u, y_u, and z_u and their derivatives are the user ECEF positions and velocities, and a_j^x, a_j^y, a_j^z are the ECEF unit vector components from the jth satellite s to the user u.

The `from_datetimes()` method is used throughout this thesis to produce the satellite states and reference LOS observables that inform subsequent measurement- and correlator-level simulations. Figure 5.2 illustrates an example satellite emitter module scenario using GPS, Galileo, and Iridium NEXT for a receiver in Auburn, AL.
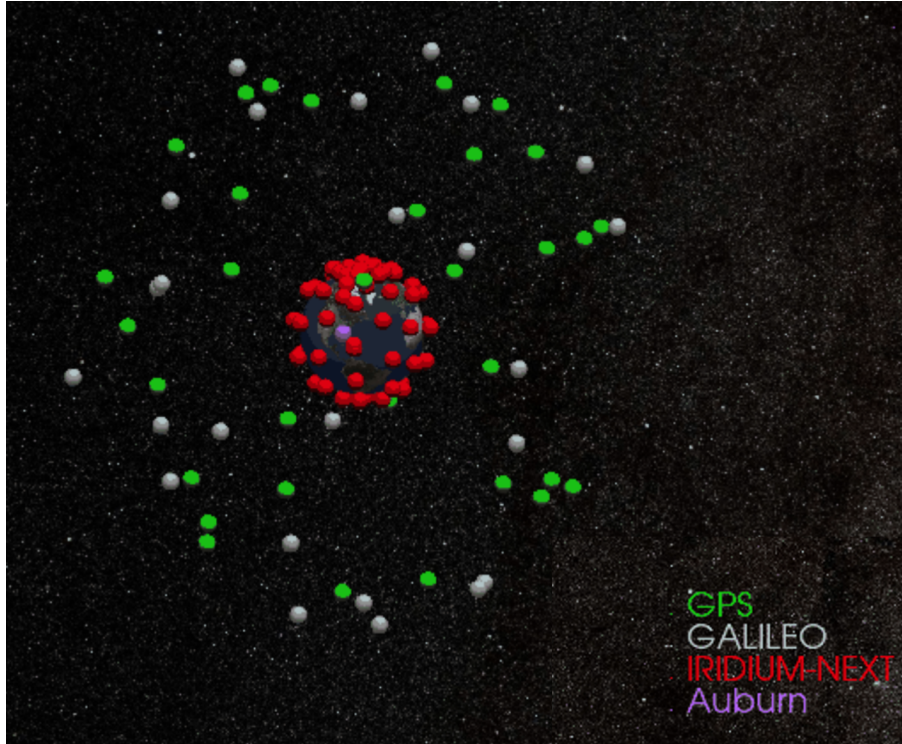
Figure 5.2: Example Navsim Satellite Emitter Module Scenario

5.2 Measurement-Level Simulation Module

The measurement-level simulation module applies realistic transmission and thermal noise errors to the reference observables returned by the satellite emitter module in the same manner as Equations 3.8 and 3.9. These errors are configured in a YAML file whose path is accepted during initialization of a Python class called `MeasurementSimulation`, where an instance of `SatelliteEmitters` is dependency injected. To invoke the `from_datetimes()` method outlined in Section 5.1, a method that accepts arrays of receiver positions and velocities named `generate_truth()` is called. When called, the method retrieves the ephemeris for the constellations in the configuration and simulates the satellite states for a specified day, duration, and update rate. Once these states are simulated, the `simulate()` method is called to apply measurement errors to the reference observables. Then, the consequent code pseudorange, carrier pseudorange, and pseudorange rate measurements are returned. The configurable errors used by the measurement-level simulation module include atmospheric channel delays, satellite clock errors, receiver clock errors, and thermal noise errors.

5.2.1 Atmospheric Error Models

The configurable atmospheric errors include ionospheric and tropospheric errors. The ionospheric errors are applied using one of two techniques. The first technique uses a Total Electron Count (TEC) map downloaded by Laika to determine the ionospheric delays that correspond to the simulated day in question. Specifically, the delays are computed using the receiver-to-emitter azimuth and elevation for all simulated time steps. The second technique uses the Klobuchar model outlined in [55] with pre-defined α and β values and the same azimuths and elevations used in the TEC map technique. Considering the ionosphere's dispersive nature, the resulting delays affect the ranging code and carrier signal differently. For this reason, a delayed code pseudorange and an advanced carrier pseudorange are produced in the measurement-level simulation module. The tropospheric errors are modeled using the International Standard Atmosphere (ISA) [86] and hydrostatic delay Saastamoinen [87] models, which are a function of the receiver position, emitter elevation, relative humidity, and the temperature at sea level.

5.2.2 Two-State Clock Error Model

The simulated clock errors for the satellite emitters and receiver utilize the two-state clock model outlined by [88]. In the two-state clock model, a clock's bias and drift are propagated with the following

$$\boldsymbol{x}_{k+1} = \boldsymbol{\Phi}\boldsymbol{x}_k + \boldsymbol{\nu}_k \tag{5.4}$$

$$\boldsymbol{x} = \begin{bmatrix} \delta t, \delta \dot{t} \end{bmatrix} \quad \boldsymbol{\Phi} = \begin{bmatrix} 1 & T \\ 0 & 1 \end{bmatrix}$$

where δt is the clock bias in seconds, $\delta \dot{t}$ is the clock drift in seconds per second, T is the simulation update period in seconds, and $\boldsymbol{\nu}_k$ is an additive white Gaussian noise (AWGN) vector drawn from $\boldsymbol{Q}_{clock}$ in Equation 3.23. The σ_b^2 and σ_r^2 variances that inform $\boldsymbol{Q}_{clock}$ are approximated as

$$\sigma_b^2 \approx \frac{h_0}{2} \tag{5.5}$$

$$\sigma_r^2 \approx 2\pi^2 h_{-2} \tag{5.6}$$

where h_0 and h_{-2} are Allan variance Power Spectral Density (PSD) coefficients for various clock qualities in seconds.

The resulting clock errors from Equation 5.4 need to be converted to units of meters and meters per second before being added to their corresponding reference observables. This is accomplished by multiplying them by the speed of light in meters per second. The five clock qualities available in Navsim and their h_0 and h_{-2} values are provided in Table 5.2. The values in this table are provided by [70]. In addition, further information regarding their Allan variance PSD coefficient derivation can be found in [89].

Table 5.2: Allan Variance Coefficients for Navsim Clock Types

Clock Type	h_0 [s]	h_{-2} [s]
Low-Quality TCXO	2×10^{-19}	2×10^{-20}
High-Quality TCXO	2×10^{-21}	3×10^{-24}
OCXO	2×10^{-25}	6×10^{-25}
Rubidium	2×10^{-22}	1×10^{-30}
Cesium	2×10^{-22}	1.5×10^{-33}

Figures 5.3 and 5.4 show the simulated clock bias and clock drift for a High-Quality Temperature-Compensated Crystal Oscillator (TCXO) over 5 minutes (300 s). This is the same receiver clock type and duration used in the Chapter 6 simulation studies.
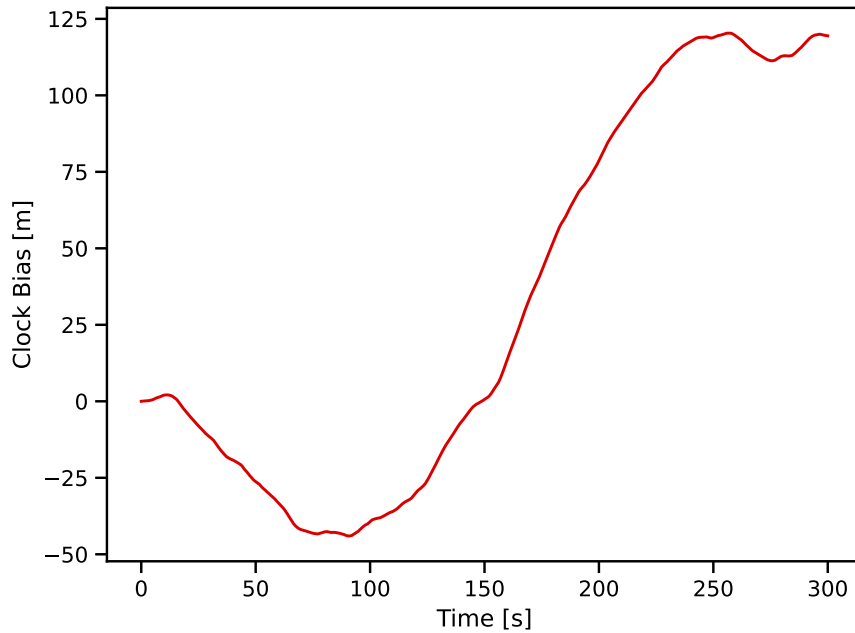
Figure 5.3: Simulated High-Quality TCXO Clock Bias
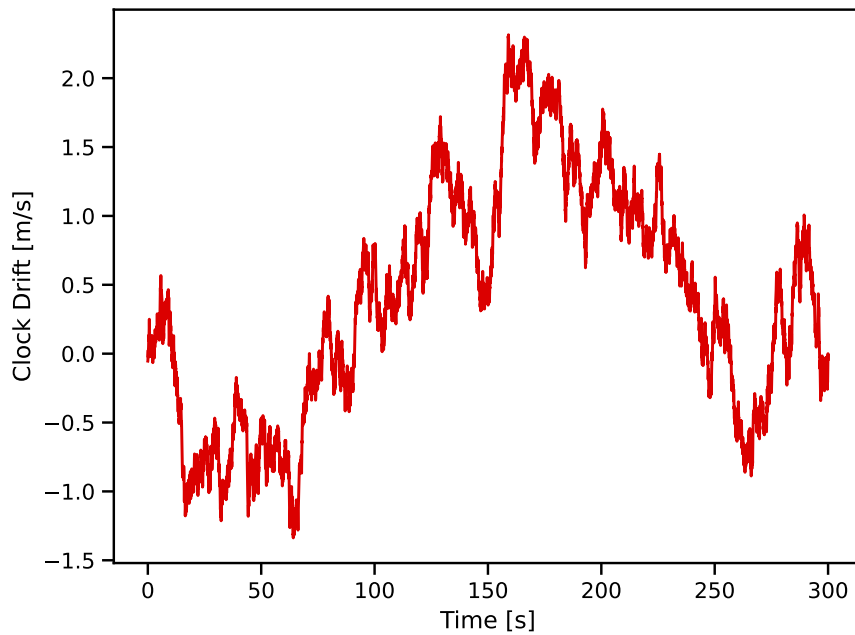
Figure 5.4: Simulated High-Quality TCXO Clock Drift

5.2.3   Received Power Model

The thermal noise errors applied by the measurement-level simulation module are a function of each emitter's received power, indicated as a C/N_0. The effective C/N_0 for each emitter is determined by a free-space path loss (FSPL) model and the nominal Effective Isotropic Radiated Power (EIRP) of each constellation's transmitting antennas. The FSPL model used by Navsim was derived from [57, 90] and its resulting C/N_0 for each emitter is given as

$$C/N_0 = EIRP - FSPL - N_0 - J/S - \upsilon \tag{5.7}$$

$$FSPL = 20 \log_{10}(4\pi \frac{r_u^j}{\lambda})$$

$$N_0 = 10 \log_{10}(kT_{noise})$$

where C/N_0 is the carrier-to-noise density ratio in dB-Hz, $EIRP$ is the transmitting antenna's Effective Isotropic Radiated Power in dB-W, $FSPL$ is the free-space path loss in dB, N_0 is the thermal noise density in dB-W/Hz, J/S is the user-defined jamming-to-signal ratio (or attenuation) in dB, and υ is an additional noise figure of $3\,\text{dB}$ to account for band-limiting, quantization, and cascaded noise in the receiver. In the FSPL calculation, r_u^j is the true geometric range to the satellite emitter, and λ is the signal's carrier wavelength. In the N_0 calculation, k is Boltzmann's constant, and T_{noise} is the noise temperature, which is assumed to be $290\,\text{K}$.

Given the true ranges to each emitter vary, the C/N_0 for each emitter will be slightly different using Equation 5.7. This difference provides realistic reception powers and is why the various RFI scenarios in Chapter 6 are indicated by signal attenuation rather than a constant C/N_0. In addition, these RFI scenarios are controlled using the J/S parameter in Equation 5.7. For the measurements returned by this module, the thermal noise is applied using loop filter measurement variance models, outlined in [53, 91]. The following section will describe how the thermal noise is applied to Navsim's correlator-level simulation outputs.

5.3 Correlator-Level Simulation Module

The correlator-level simulation module produces correlator outputs that effectively simulate the correlation of a local signal replica with a received signal. The benefit of this type of simulation is that it allows for the rapid testing of receiver architectures using a Monte Carlo analysis. When considering a Monte Carlo analysis at the signal level, the multiplications required to generate and process hundreds or thousands of baseband complex samples far exceed those needed for a correlator-level simulation. This is because a correlator model (e.g., the BPSK model in Equation 3.2) requires fewer than 20 multiplications for all integration period durations, while a signal sampled at 12.5 MHz, for example, requires 12,500 multiplications for a 0.001 s integration period.

The correlator model used in this thesis is found in Equation 3.2. As with the thermal noise errors described in Section 5.2.3, the correlator model uses the C/N_0 produced by Equation 5.7 to inform the scale factor A that determines the effect of the unit variance noise on each correlator. This model is applied after signal parameter errors are computed by differencing predicted measurements from a receiver with the outputs of the measurement-level simulation module.

The interface for the correlator-level simulation module is similar to the measurement-level simulation module. However, the correlator-level simulation is not entirely self-contained. This is because feedback from the receiver is required to generate the next set of correlator outputs at each simulated time step. The class called `CorrelatorSimulation` contains the correlator-level simulation and is initialized with the same configuration as the measurement-level simulation. It utilizes two methods called `compute_errors()` and `correlate()`. The `compute_errors()` method accepts the measurements from the measurement-level simulation, the predicted measurements from a receiver, and true or perturbed satellite states from the satellite emitter module. Once calculated, the resulting errors are buffered in memory until the `correlate()` method is called. This method accepts a code phase offset to simulate any early or late correlators, which is defined by Δ in Equation 3.2. In addition, the number of sub-correlators to return can be specified for use in a discriminator like Equation 3.28, for example.

In practice, these two methods are called in a loop where each iteration indicates a new simulated time step (i.e., integration period). For more information regarding Navsim's modules, the reader is referred to the source code `https://github.com/navsquad/navsim`.

5.4 Assumptions for Simulation Studies

Despite being developed for this thesis, not all of Navsim's features are used in the simulated scenarios presented in Chapter 6. For all scenarios, atmospheric and satellite clock errors were not simulated because they are not directly estimated in any of the considered receiver architectures. For the simulations involving dedicated LEO PNT and opportunistic LEO PNT satellite emitters, assumptions defined in the subsequent sections were made to simplify the relative performance comparison of their corresponding architectures.

5.4.1 Dedicated LEO PNT Simulations

The LEO constellations simulated in this thesis that transmit dedicated LEO PNT signals are considered proxy constellations. This means that these constellations are only used for their satellite states and not their signal structures (e.g., Iridium NEXT's Satellite, Time, and Location (STL) signal). Instead, their signals are replaced with a custom signal simulated at a frequency in the upper L-Band with the GPS L1 C/A BPSK modulation, allowing for the use of Equation 3.2. As a result, the chipping and data rates of this signal are 1.023 MHz and 50 Hz, respectively. Subsequently, this data rate defines the maximum coherent integration period as 20 ms for the dedicated LEO PNT signal, assuming no data message prediction. The specific carrier frequency for this signal is 1856.27 MHz. In addition, the relationship between the system times for GPS and the dedicated LEO PNT constellation is assumed to be known.

5.4.2 Opportunistic LEO PNT Simulations

The opportunistic LEO PNT scenarios simulated in this thesis make three assumptions. The first assumption uses Iridium NEXT emitter states from a Jackson Labs STL-2600 [92] receiver to generate an assumed model of TLE propagation error. This error model is necessary to achieve realistic results given opportunistic solutions do not have accurate knowledge of

emitter states. Emitter states from the STL-2600 were used to compute TLE errors for Iridium NEXT over a 13-minute (800 s) scenario. The intermittent three-dimensional ECEF position and velocity error magnitudes between the STL-2600 and TLE states can be seen in Figures 5.5 and 5.6, where each color indicates a different emitter's errors.
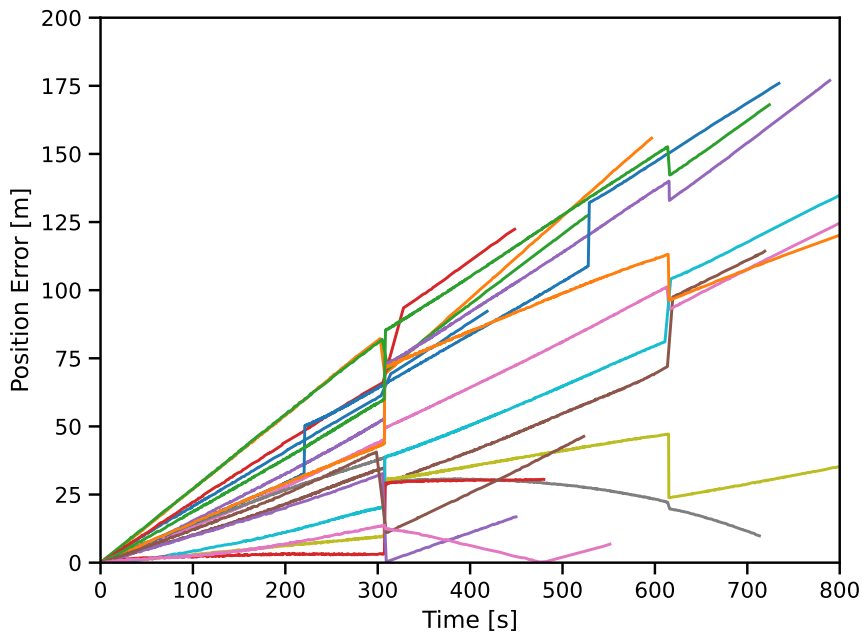
Figure 5.5: 3D Position State Error Magnitudes of TLE and STL-2600 Comparison
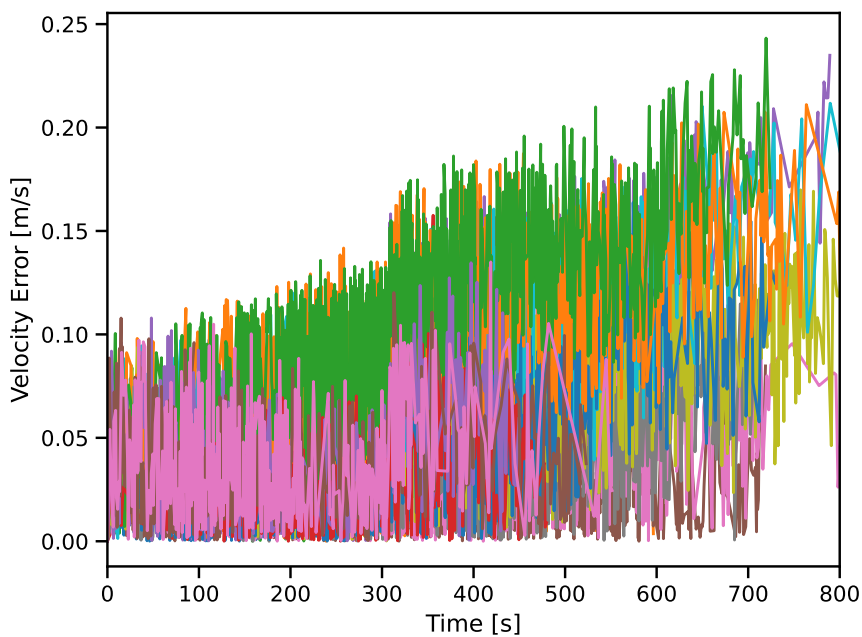
Figure 5.6: 3D Velocity State Error Magnitudes of TLE and STL-2600 Comparison

The results in Figure 5.6 indicate the velocity error behaves as a random walk. This allows for practical TLE errors to be simulated using a simple model. Traditionally, modeling these errors is not trivial [18, 93], but the random walk assumption is sufficient for comparing to solutions whose ephemeris is more accurate. One model for a random walk is the First-Order Gauss Markov (FOGM) process, which is described as

$$x_{k+1} = \exp\left(\frac{-T}{\tau}\right) x_k + \eta$$

$$\eta \sim \mathcal{N}(0, \sigma^2)$$

(5.8)

where τ is the time constant in seconds, T is the simulation update period in seconds, and σ^2 is the variance in the squared units of x.

Equation 5.8 was used to model each Cartesian ECEF velocity error to loosely approximate the final error magnitude variance (near 800 s) indicated in Figure 5.6. These velocity errors were then integrated to approximate the final position error magnitude variance in Figure 5.5. Through trial and error, it was determined that a σ of 0.0005 m/s and τ of 4000 s best approximated the final variances and general error growth. The results for 500 simulated FOGM position and velocity error magnitudes can be seen in Figures 5.7 and 5.8.
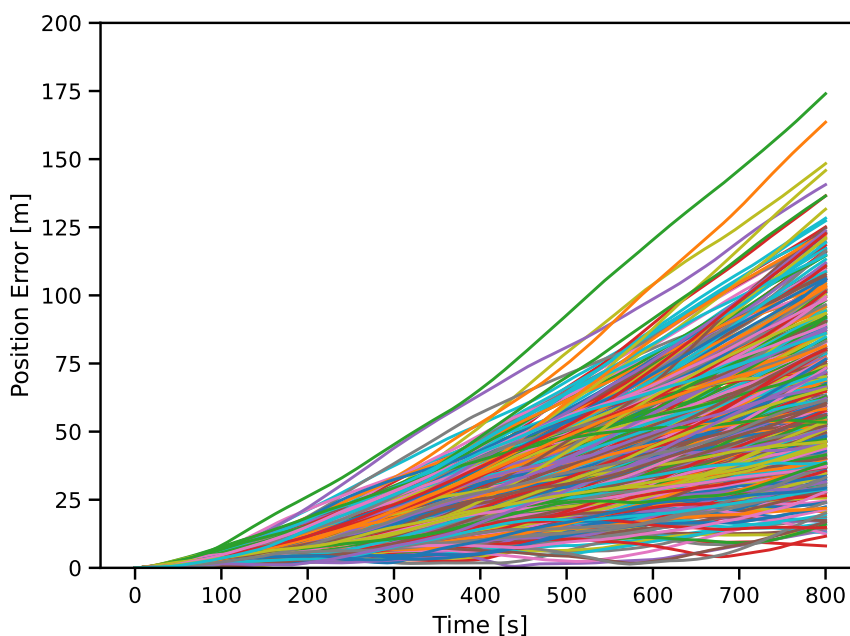
Figure 5.7: Simulated 3D Position State Error Magnitudes with FOGM Model
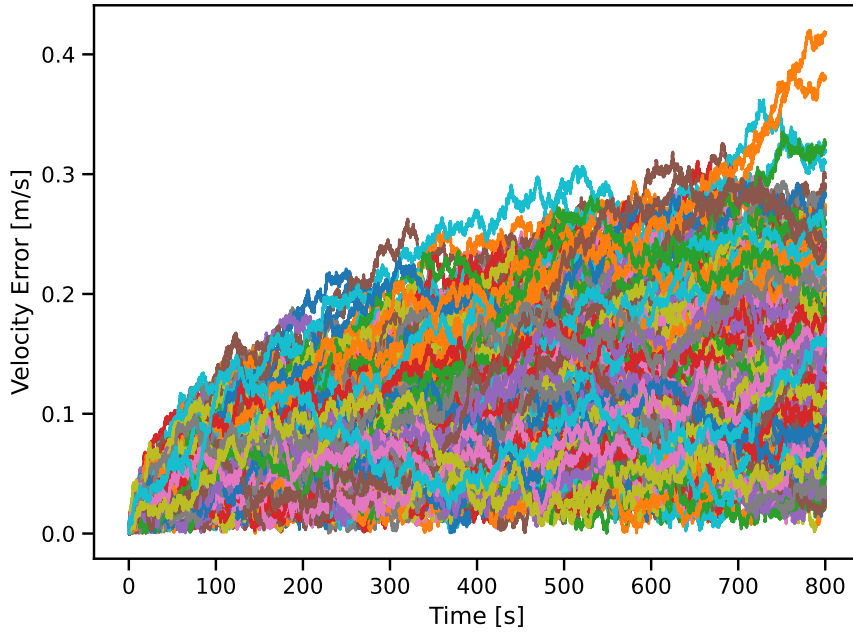
Figure 5.8: Simulated 3D Velocity State Error Magnitudes with FOGM Model

The second assumption pertains to the update rate of the opportunistic Doppler shift measurements used to aid GNSS. The update rate of the Jackson Labs STL-2600 was used for this value. It was determined for the same scenario depicted in Figures 5.5 and 5.6 that the average update rate was approximately 2 Hz. This slow average update rate is due to the nature of Iridium NEXT's Time Division Multiple Access (TDMA) channel access method. As a result of this method, only a single satellite emitter can be received at a time, causing variable update rates that depend on which emitters are in view. Therefore, this thesis assumes only one simulated opportunistic satellite can be received at a time in the studies presented in Chapter 6.

The third assumption regards the noise associated with the opportunistic Doppler shift measurements. The measurement noise associated with these measurements was applied using an FLL standard deviation model given by [91] as

$$\sigma_{\delta f} \approx \frac{1}{\pi T} \sqrt{\frac{B_L}{C/N_0}} \tag{5.9}$$

where B_L is an assumed loop filter bandwidth of 18 Hz, T is the simulation update period—not to be confused with the Doppler shift measurement update period—in seconds, and C/N_0 is the carrier-to-noise density ratio from Equation 5.7. This standard deviation is used to draw

samples from a zero-mean Gaussian distribution, which are added to the true Doppler shift measurements.

Chapter 6

Simulation Studies and Results

This chapter evaluates the performance of the proposed LEO-aided GNSS DPE architectures in three simulation studies. The first two studies evaluate the performance of the dedicated and opportunistic LEO PNT-aided architectures in different dynamic scenarios. Then, the third focuses on evaluating the dedicated LEO PNT architecture's computational efficiency compared to a standalone GNSS DPE architecture.

All of the simulation studies are conducted using Navsim, the simulation environment outlined in Chapter 5. In the first two studies, each architecture is evaluated with the root mean square error (RMSE) of its estimated position, velocity, and clock states. In addition, each architecture's probability of tracking a single GNSS constellation is examined. For all of the studies, this constellation is simulated as GPS. For each architecture, the received GPS L1 C/A signals are degraded by simulating the effective C/N_0 for each received satellite, which is further discussed in Section 5.3. The results for each of the proposed architectures are compared to other advanced receiver architectures. Specifically, these architectures comprise a standalone GPS DPE receiver, a LEO-aided GPS VDFLL receiver, and a standalone GPS VDFLL receiver. The remainder of this chapter refers to these architectures as DPE-GPS, VP-GPS-LEO, and VP-GPS, respectively. Finally, the dedicated and opportunistic LEO PNT-aided architectures are referred to as DPE-GPS-LEO and ODPE, respectively.

In the third study, the computational efficiency of DPE-GPS-LEO is evaluated. This is done by comparing its estimated position, velocity, and clock state RMSEs to those of DPE-GPS for various scenarios. Specifically, these scenarios vary the number of particles each architecture uses to show that fewer particles are required to achieve a specified accuracy for DPE-GPS-LEO. Further, this study constrains the number of total received channels to eight.

71

In addition, the number of LEO satellites is varied to determine how much each additional satellite affects the accuracy of the estimated states.

The three studies are called the Commercial Airliner study, the Ground Vehicle study, and the Computational Efficiency study, and are described in that order. The rest of this chapter outlines the scenarios used in each before presenting and discussing the results.

6.1 Commercial Airliner Study

The Commercial Airliner study is a Monte Carlo analysis for the abovementioned architectures. Specifically, 100 simulations are performed for the five architectures across nine dynamic GPS RFI scenarios, resulting in 4500 simulations. The RFI scenarios are implemented as described in Section 5.3 for a range of GPS C/N_0 attenuation values. These values begin at $0\,dB$ and increase by increments of $5\,dB$ of attenuation up to $40\,dB$. This corresponds to a C/N_0 range of approximately $47\,dB\text{-Hz}$ to $7\,dB\text{-Hz}$ for GPS, depending on the FSPL associated with each satellite. Given the relative power of LEO constellations, the considered LEO signals and measurements are assumed to be obtained in ideal conditions. In addition, a High-Quality TCXO is simulated as the receiver clock, and its states are regenerated for each simulation.

6.1.1 Scenario Description

The Commercial Airliner study is simulated at the Sydney Airport (SYD) in Sydney, New South Wales, Australia. Each simulation begins at 00:00:00 UTC on December 4th, 2023 (GPS Time: Week 2291, TOW 86418.0) and lasts for five minutes (300 s). The update rate of each simulation is 50 Hz. This corresponds to a coherent integration period of 20 ms for each architecture. The assumed platform is an aerial vehicle. This vehicle is subjected to a dynamic scenario that can be seen in Figure 6.1. Specifically, the simulated vehicle begins static, performs a taxi maneuver, and takes off from its respective runway. The maximum speed achieved throughout this trajectory is approximately 96 m/s (~214 mph).
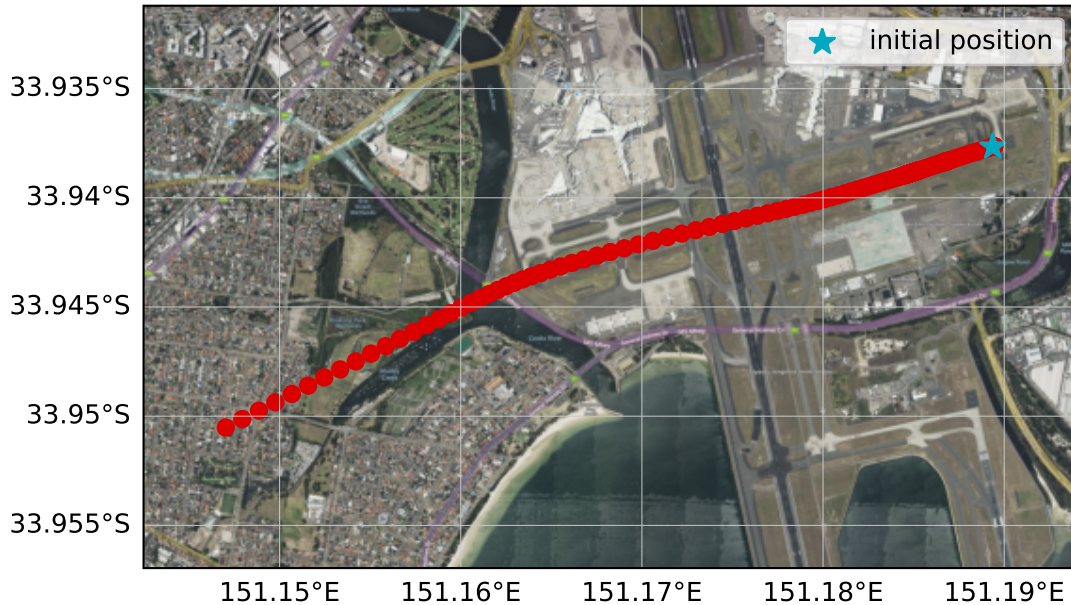
Figure 6.1: Dynamic Commercial Airliner Trajectory in Sydney, Australia

In addition, the GPS and Iridium NEXT constellations are simulated for this scenario using Navsim. GPS is used as the GNSS constellation received by each architecture. Iridium NEXT is used as a proxy constellation for each LEO-aided architecture. This proxy constellation is solely used for its satellite states, as described in Section 5.4. These states determine the transmission characteristics of a dedicated LEO PNT signal and opportunistic LEO PNT Doppler shift measurements. Further details describing this signal and these Doppler shift measurements can be found in Sections 5.4.1 and 5.4.2, respectively.

Figure 6.2 illustrates the geometry of the two simulated constellations. These constellations are simulated at a mask angle of 10 degrees, yielding the dilution of precision (DOP) values seen in Tables 6.1 and 6.2. Specifically, these tables provide the maximum and minimum geometric, horizontal, vertical, and time DOP values for standalone GPS and GPS with Iridium NEXT, respectively.
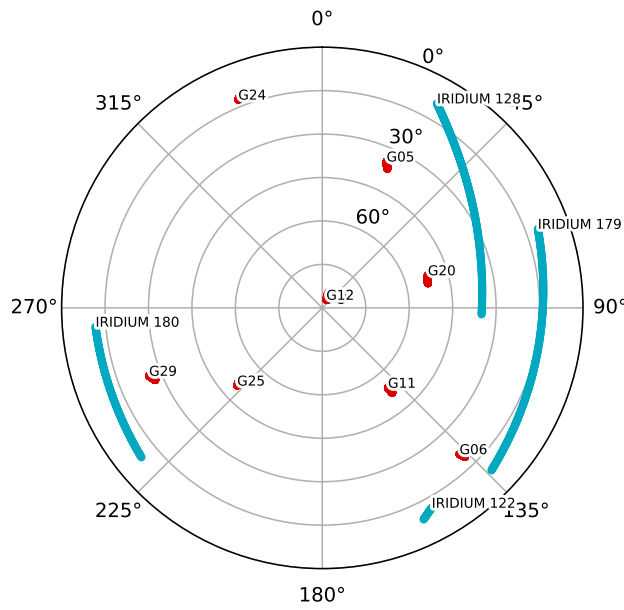
Figure 6.2: GPS and LEO Skyplot for Commercial Airliner Study

Iridium NEXT was selected as the LEO proxy constellation in this scenario for its small number of in-view satellites. Specifically, less than four LEO satellites can be seen for most of the duration, with only ~10 s where four are visible. This allows for a fair comparison between the considered GPS and LEO-aided architectures by preventing a consistently valid standalone LEO solution when GPS is heavily degraded. For the rest of this section, the GPS with Iridium NEXT scenarios will be referred to as GPS-LEO.

Table 6.1: Commercial Airliner Study GPS Dilution of Precision

Min./Max.	GDOP	HDOP	VDOP	TDOP	# GPS SV	# LEO SV
Min.	2.40	0.69	2.10	0.95	8	0
Max.	2.63	0.70	2.32	1.03	8	0

Table 6.2: Commercial Airliner Study GPS and LEO Dilution of Precision

Min./Max.	GDOP	HDOP	VDOP	TDOP	# GPS SV	# LEO SV
Min.	1.15	0.36	1.04	0.33	8	1
Max.	2.36	0.61	2.09	0.91	8	4

6.1.2 Results

In this study, each receiver architecture is initialized (or grid-centered for DPE) at the true state. The position and velocity process noise is defined using Equation 3.24 with $\sigma_{xyz} = 6\,\mathrm{m/s}^{\frac{3}{2}}$. The clock process noise was defined by the PSD coefficients for the High-Quality TCXO presented in Table 5.2. Figure 6.3 shows the resulting position and velocity RMSEs for each simulated GPS C/N_0 attenuation.

(a) Position RMSE (b) Velocity RMSE
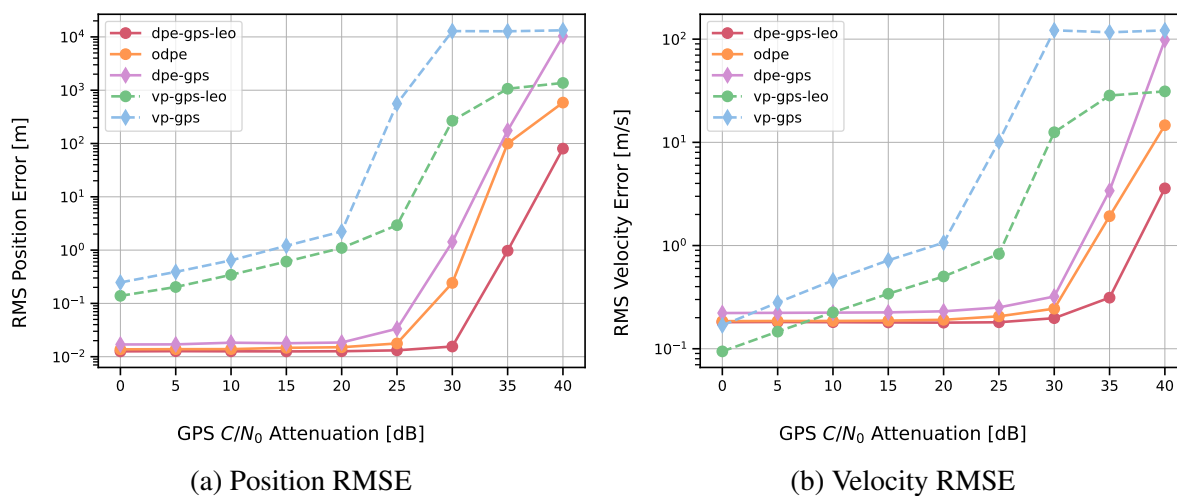
Figure 6.3: Position and Velocity State RMSEs for Dynamic Commercial Airliner Study

It can be seen that the DPE architectures are comparable to or better than the VP architectures in low GPS RFI regimes. The most significant difference is apparent in position RMSE performance, with nearly an order of magnitude difference between the DPE and VP architectures. This stark difference results from the carrier phase preservation of Equation 4.9, which is not possible using a VDFLL. Considering the high C/N_0 attenuation regimes, the DPE architectures perform better than VP until the DPE-GPS receiver is overwhelmed at an attenuation of 40 dB. The advantage of LEO-aiding is evident at this high C/N_0 attenuation as the performance of the aided architectures is superior to the standalone GPS architectures. Specifically, the proposed architectures perform the best, with the DPE-GPS-LEO understandably outperforming ODPE.

The same all-around benefits in high GPS C/N_0 attenuation regimes are seen in the clock bias and clock drift RMSEs shown in Figure 6.4. However, there is a noticeable difference

when observing the performance of the DPE architectures at low C/N_0 attenuation. The RMSEs for all the DPE architectures are greater than VP until 20 dB of GPS C/N_0 attenuation. This observation is alarming as it is consistent across all DPE architectures, regardless of whether they're being aided. It almost seems the clock states are not entirely observable in DPE, but this is false. These results are simply attributed to an insufficient number of particles. Specifically, the dynamics of the High-Quality TCXO cannot be tracked well because the effective bandwidth of the SIR particle filter is too small. In ideal signal conditions, 1201 particles cannot resolve these states compared to the VDFLL. However, this number of particles prioritizes computational efficiency while maintaining the desired performance in most high attenuation regimes.

(a) Clock Bias RMSE   (b) Clock Drift RMSE
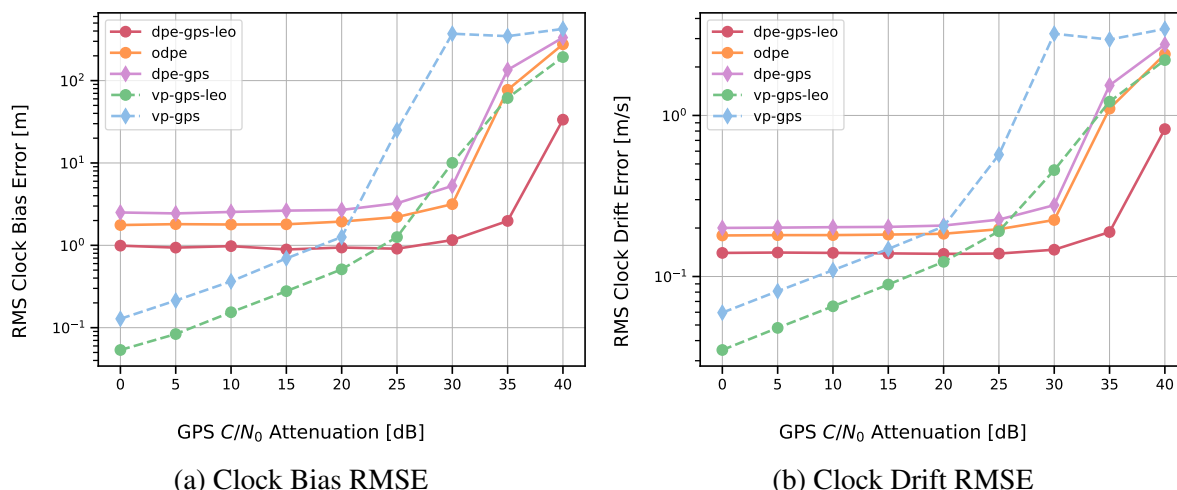
Figure 6.4: Clock Bias and Clock Drift State RMSEs for Dynamic Commercial Airliner Study

Two additional Monte Carlo analyses are performed to confirm the clock states are observable in DPE. The first analysis increases the number of particles to 12001 and reduces the duration to 30 s to prevent a prohibitively long simulation time. For context, this analysis for 12001 particles lasts nearly 36 hours per architecture, whereas the 1201 particle simulations last 12 hours per architecture. Figure 6.5 shows the clock state results for this analysis. The ODPE architecture is not included as it is bounded by DPE-GPS and DPE-GPS-LEO, as seen in Figure 6.4.

Compared to Figure 6.4, the DPE clock bias estimates in Figure 6.5 are more similar to their VP counterparts in the low attenuation regimes. This confirms that the clock bias

(a) Clock Bias RMSE

(b) Clock Drift RMSE
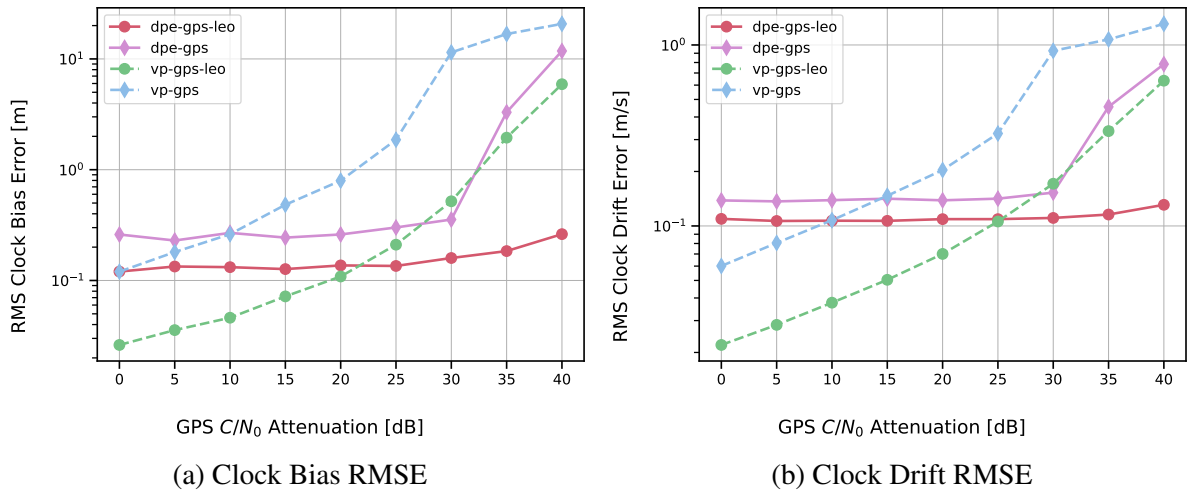
Figure 6.5: Clock State Observability Monte Carlo Analysis for 12001 Particles

is observable in DPE. However, the performance is still not ideal, implying that many more particles are needed to close the gap between the VP and DPE estimates. In addition, there is little discernible improvement in the clock drift, which motivates the second analysis.

The second analysis is performed over the same $30\,\text{s}$ duration but returns to using 1201 particles. Besides the number of particles, the difference between this analysis and the first is the simulated receiver clock type. A higher quality OCXO, detailed in Table 5.2, is simulated to decrease the effective bandwidth requirement of the SIR particle filter in hopes of confirming clock drift observability. In addition, this analysis was only conducted in the low attenuation regime. Figure 6.6 illustrates the results of this analysis.

(a) Clock Bias RMSE
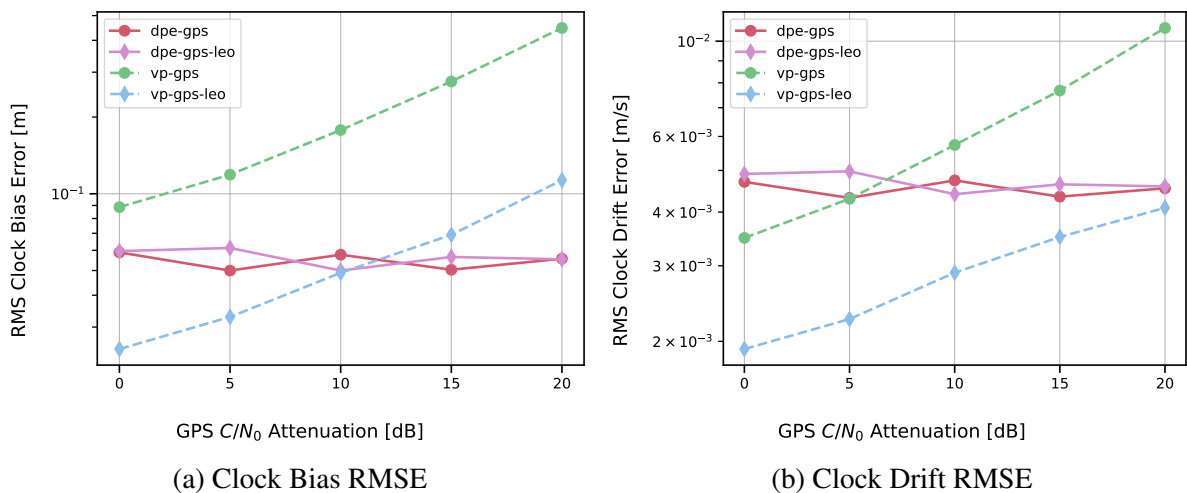
(b) Clock Drift RMSE

Figure 6.6: Clock State Observability Monte Carlo Analysis for an OCXO

Once again, the clock bias is observable. Unlike the first analysis, the clock drift is also observable. This is concluded by the DPE clock drift RMSEs compared to each VP architecture. Observing the scale of the RMSEs in Figure 6.6b, it can be seen that each estimate is more or less the same for the low GPS RFI regimes.

Figure 6.7 further demonstrates the performance capabilities of ODPE and DPE-GPS-LEO by presenting the probability of tracking GPS. The probability of tracking is computed as the mean percentage of successfully tracked satellites for each attenuation's 100 Monte Carlo simulations. A satellite is considered successfully tracked if the code phase errors associated with the satellite do not exceed ± 0.5 chips for the simulation's final γ estimate. For the Commercial Airliner study, these results indicate DPE-GPS-LEO increases the probability of tracking by up to 85.12 % for 40 dB of GPS C/N$_0$ attenuation. In addition, ODPE increases the probability of tracking by up to 28.52 % at the same attenuation. Table 6.3 further illustrates the probability of tracking GPS results for high GPS C/N$_0$ attenuation. In this table, the red entries indicate where the probability of tracking GPS is below 100%.
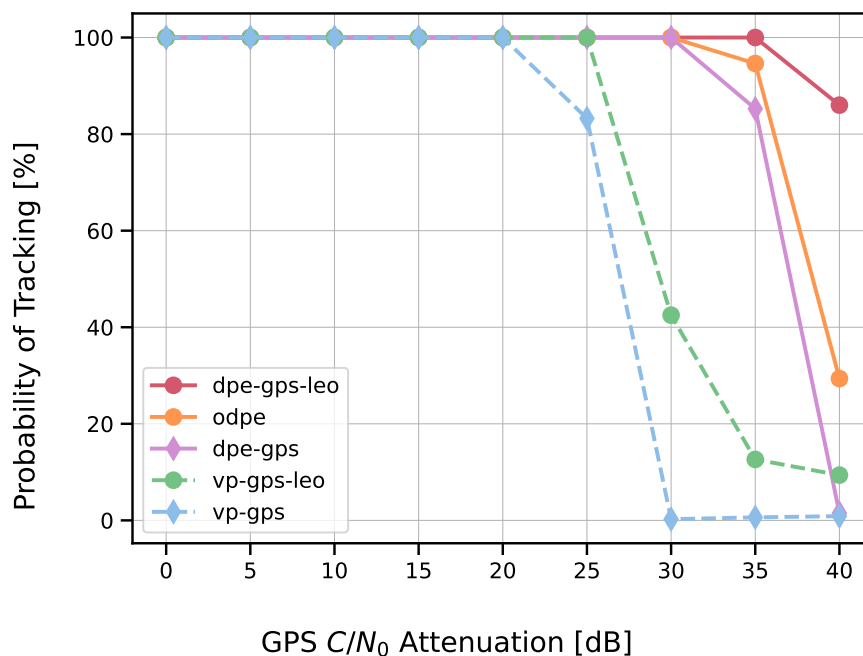
Figure 6.7: Probability of Tracking GPS for Dynamic Commercial Airliner Study

Table 6.3: Probability of Tracking GPS in High RFI for Dynamic Commercial Airliner Study

GPS C/N$_0$ Attenuation	DPE-GPS-LEO	ODPE	DPE-GPS	VP-GPS-LEO	VP-GPS
20 dB	100%	100%	100%	100%	100%
25 dB	100%	100%	100%	100%	83.3%
30 dB	100%	100%	100%	42.5%	0.25%
35 dB	100%	94.6%	85.3%	12.6%	0.63%
40 dB	86.0%	29.4%	1.50%	9.38%	0.88%

Further results for the Commercial Airliner study can be found in Appendix A. Specifically, a static scenario is considered at the initial position indicated in Figure 6.1. In addition, the dynamic scenario is repeated where the LEO proxy constellation is changed to Orbcomm. Overall, these additional results offer the same conclusions as this section but are included for completeness.

6.2 Ground Vehicle Study

Like the previous study, the Ground Vehicle study is a Monte Carlo analysis performed for the five considered architectures. Once again, 100 simulations are performed for each architecture across nine dynamic GPS RFI scenarios, resulting in 4500 simulations. The RFI scenarios are implemented as described in Section 5.3 for the same range of GPS C/N$_0$ attenuation values previously simulated. The considered LEO signals and measurements are assumed to be obtained in ideal conditions. In addition, a High-Quality TCXO is simulated as the receiver clock, and its states are regenerated for each simulation.

This study aims to analyze how the proposed DPE architectures' performance changes when applied to a platform with less consistent dynamics. In the previous study, the dynamics of the aerial vehicle were fairly predictable once it began to take off. This is not the case in the Ground Vehicle study, as the vehicle consistently stops before speeding up again. Therefore, the effect of the constant velocity assumption would likely change. Specifically, this study aims to see if the change in dynamics manifests itself differently in DPE compared to the VP architectures.

6.2.1 Scenario Description

The Ground Vehicle study is simulated in Miyanoshimo, Yamaguchi, Japan. Like the previous study, each simulation begins at 00:00:00 UTC on December 4th, 2023 (GPS Time: Week 2291, TOW 86418.0) and lasts for five minutes (300 s). The update rate of each simulation is 50 Hz. This corresponds to a coherent integration period of 20 ms for each architecture. The assumed platform is a ground vehicle. This vehicle is subjected to a dynamic scenario that can be seen in Figure 6.8. Specifically, the simulated vehicle begins static and then drives a route on a highway through two different cities, stopping occasionally at traffic signs. The maximum speed achieved throughout this trajectory is approximately 31 m/s ($\sim$69 mph).
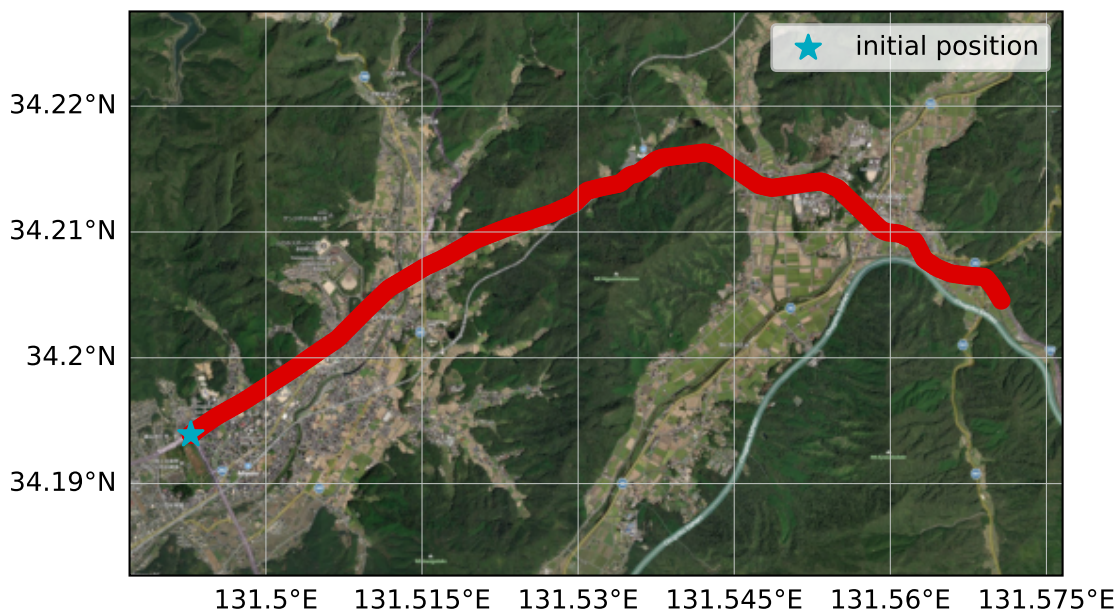
Figure 6.8: Dynamic Ground Vehicle Trajectory in Miyanoshimo, Japan

Once again, the GPS and Iridium NEXT constellations are simulated using Navsim for the same reasons discussed in the previous section. Figure 6.9 illustrates the geometry of the two simulated constellations. Like the Commercial Airliner study, these constellations are

simulated at a mask angle of 10 degrees, yielding the DOP values seen in Tables 6.4 and 6.5. One difference between this study and the previous is the number of visible LEO satellites. Specifically, less than four LEO satellites can be seen for the entire duration. In fact, only a maximum of two LEO satellites are ever visible simultaneously, lasting only ~48 s. Again, this allows for a fair comparison between the considered GPS and LEO-aided architectures by preventing a consistently valid standalone LEO solution when GPS is heavily degraded. In addition, the overall GPS DOP for this scenario is much worse than that seen in the Commercial Airliner study.
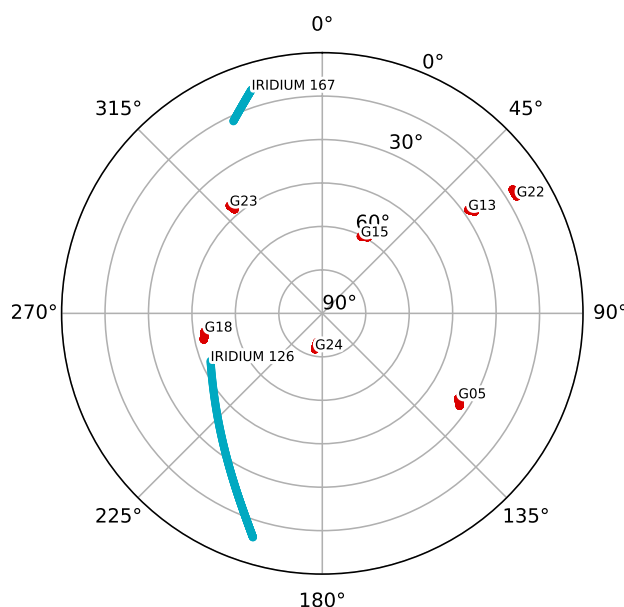
Figure 6.9: GPS and LEO Skyplot for Ground Vehicle Study

Table 6.4: Ground Vehicle Study GPS Dilution of Precision

Min./Max.	GDOP	HDOP	VDOP	TDOP	# GPS SV	# LEO SV
Min.	5.75	1.38	4.84	2.78	7	0
Max.	6.18	1.46	5.19	3.02	7	0

Table 6.5: Ground Vehicle Study GPS and LEO Dilution of Precision

Min./Max.	GDOP	HDOP	VDOP	TDOP	# GPS SV	# LEO SV
Min.	1.67	0.55	1.46	0.58	7	1
Max.	5.38	1.20	4.64	2.45	7	2

6.2.2 Results

As before, each receiver architecture is initialized (or grid-centered for DPE) at the true γ, which is defined in Equation 3.12. The position and velocity process noise is defined using Equation 3.24 with $\sigma_{xyz} = 6 \, \mathrm{m/s}^{\frac{3}{2}}$, the same value used in the previous study. The clock process noise was defined by the PSD coefficients for the High-Quality TCXO presented in Table 5.2. Figure 6.10 shows the resulting position and velocity RMSEs for each simulated GPS C/N$_0$ attenuation.

(a) Position RMSE (b) Velocity RMSE
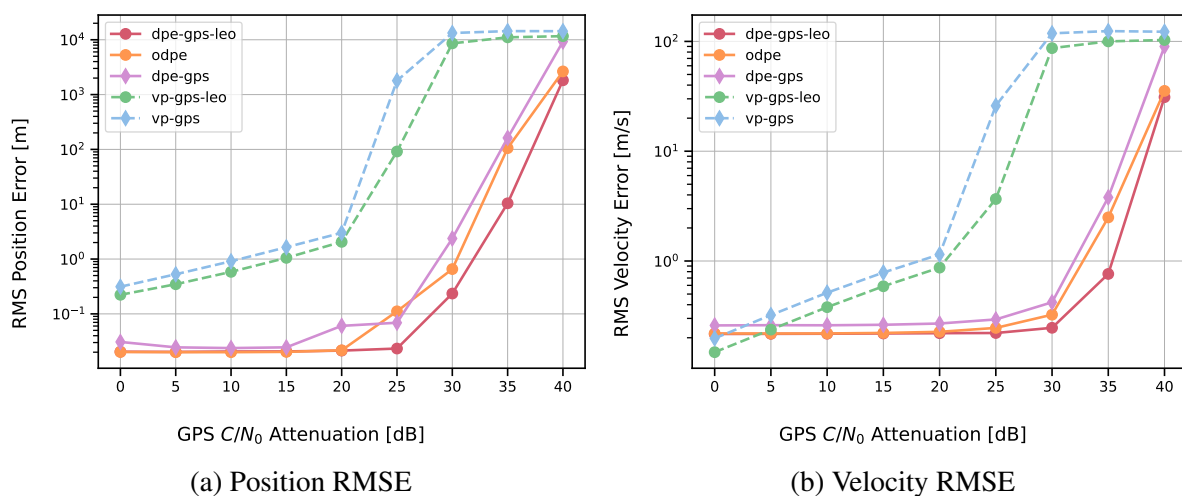
Figure 6.10: Position and Velocity State RMSEs for Dynamic Ground Vehicle Study

For the most part, the relative performance results indicated in Figure 6.10 are consistent with the previous study. There is no clear indication the change in dynamics affects the relative performance of the DPE and VP architectures. However, there is one slight outlier at 25 dB of attenuation for ODPE. Its position RMSE is slightly higher than that of DPE-GPS, but this is insignificant given the scale of the errors. Despite being negligible, this is likely attributed to ODPE's lack of robustness given its opportunistic nature (i.e., unknown ephemeris and slow update rate).

Considering the high attenuation regimes, each DPE architecture provides a more accurate solution than VP. However, this accuracy appears to fall off quicker than in the previous study. This is likely attributed to this scenario's significant increase in maximum DOP. As a result, the benefits of diverse satellite geometry cannot be exploited to reduce peak variance in the DPE

manifold when correlator noise is high. This is even the case in the GPS-LEO architectures, given only one LEO satellite is available for 252 s of the 300 s duration.

Once again, the same benefits seen in the position and velocity estimates appear in the clock state estimates for high RFI shown in Figure 6.11. Conversely, the low attenuation regimes possess the same RMSE discrepancies seen in the previous study. These discrepancies are explained explicitly in Section 6.1.2. Despite performing relatively well in the high regimes, an interesting observation for the DPE architectures can be made at 40 dB of GPS attenuation. At this level of RFI, it is apparent that all of the RMSEs seemingly converge. Once again, this is likely a result of the poor DOP relative to the Commercial Airliner study. Essentially, the DOP combined with the low effective bandwidth of the SIR particle filter appears to diminish the theoretical returns of each DPE architecture for the clock states.

(a) Clock Bias RMSE
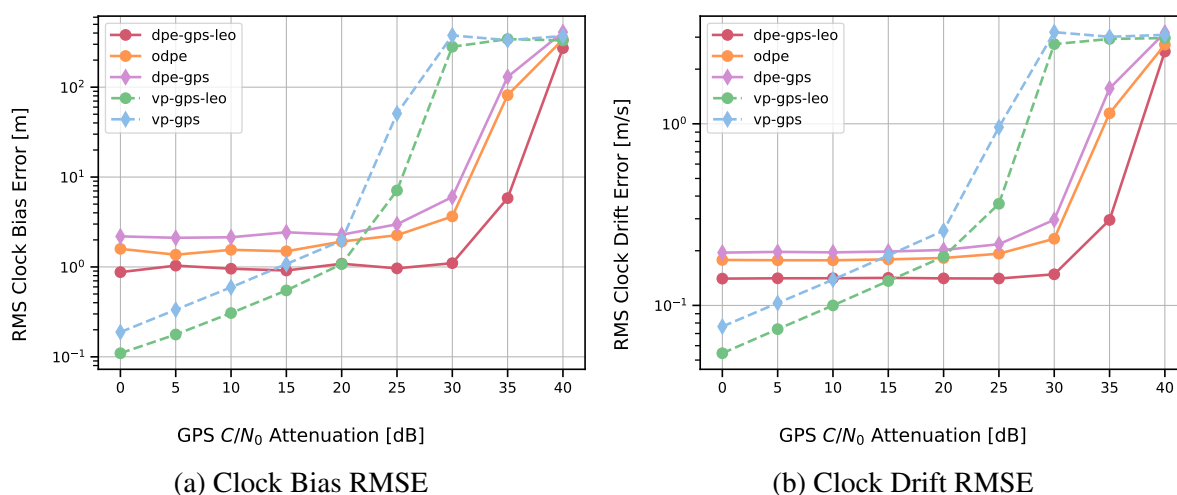
(b) Clock Drift RMSE

Figure 6.11: Clock Bias and Clock Drift State RMSEs for Dynamic Ground Vehicle Study

Figure 6.12 presents the probability of tracking GPS, whose definition is given in Section 6.1.2, for each architecture. In terms of purely aiding GPS, DPE-GPS-LEO and ODPE perform the best among the architectures, as expected. However, their respective increase in the probability of tracking is less than depicted in the Commercial Airliner study. This is an effect of the quicker estimate degradation at high GPS C/N_0 attenuation, which results from the higher DOP of the scenario. At the highest attenuation, DPE-GPS-LEO only provides a 13.99% maximum increase, while ODPE provides a 10.69% maximum increase. However, at 35 dB of attenuation, these performance increases jump to 99.29% and 96.19%, respectively,

83

demonstrating the advantages of the LEO-aided DPE architectures. Table 6.6 further illustrates the probability of tracking GPS results for high GPS C/N_0 attenuation. In this table, the red entries indicate where the probability of tracking GPS is below 100%.
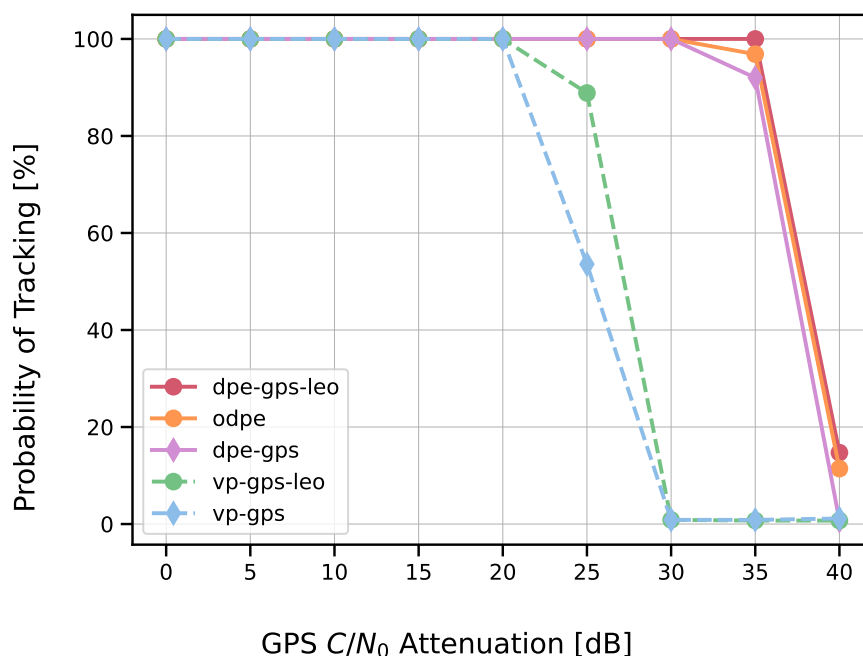
Figure 6.12: Probability of Tracking GPS for Dynamic Ground Vehicle Study

Table 6.6: Probability of Tracking GPS in High RFI for Dynamic Ground Vehicle Study

GPS C/N_0 Attenuation	DPE-GPS-LEO	ODPE	DPE-GPS	VP-GPS-LEO	VP-GPS
20 dB	100%	100%	100%	100%	100%
25 dB	100%	100%	100%	88.8%	53.6%
30 dB	100%	100%	100%	0.86%	0.86%
35 dB	100%	96.9%	92.0%	0.71%	0.86%
40 dB	14.7%	11.4%	0.71%	0.71%	1.14%

Further results for the Ground Vehicle study can be found in Appendix B. Specifically, a static scenario is considered at the initial position indicated in Figure 6.8. In addition, the dynamic scenario is repeated where the LEO proxy constellation is changed to Orbcomm. Overall, these additional results offer the same conclusions as this section but are included for completeness.

6.3 Computational Efficiency Study

The Computational Efficiency study is a simple Monte Carlo analysis performed for DPE-GPS-LEO and DPE-GPS. In this analysis, 200 simulations are performed for seven different numbers of candidate particles in a single GPS RFI scenario, totaling 1400 simulations. The specific RFI scenario subjects GPS to 25 dB of attenuation, corresponding to a received C/N_0 near 22 dB-Hz for each satellite. Given the relative power of LEO constellations, the considered LEO signals are assumed to be obtained in ideal conditions. In addition, a High-Quality TCXO is simulated as the receiver clock, and its states are regenerated for each simulation.

This study aims to indirectly analyze the computational efficiency of DPE-GPS-LEO compared to DPE-GPS. This analysis is important as it determines whether aiding from LEO can reduce the computational burden of GNSS DPE. Specifically, this can be determined by comparing the RMSEs of DPE-GPS-LEO and DPE-GPS when evaluated with the same number of particles and processed satellites. If the accuracy achieved by DPE-GPS-LEO is greater than DPE-GPS for N particles, then it can be assumed that the accuracy of DPE-GPS can be achieved with fewer than N particles for DPE-GPS-LEO. This is a valid characterization of efficiency as the number of particles DPE uses directly corresponds to the number of correlations performed by a receiver. In addition, this characterization is agnostic to specific hardware used to implement DPE in practice. The simulated scenario for this indirect analysis is outlined in the next section.

6.3.1 Scenario Description

The scenario used by the Computational Efficiency study employs the same dynamic trajectory from the Commercial Airliner study. However, only 30 s of the trajectory is considered to prioritize simulation efficiency. Like the previous studies, each simulation begins at 00:00:00 UTC on December 4th, 2023 (GPS Time: Week 2291, TOW 86418.0). The update rate of each simulation is 50 Hz. This corresponds to a coherent integration period of 20 ms for each architecture.

In addition, the GPS and OneWeb constellations are simulated for this scenario using Navsim. GPS is used as the GNSS constellation received by each architecture. OneWeb is used as a proxy constellation for DPE-GPS-LEO. Once again, this proxy constellation is used in the same manner as the previous studies. To ensure valid efficiency comparisons, the total number of received satellites is constrained to eight. In addition, the number of LEO satellites used by DPE-GPS-LEO varies from one to three to provide a better understanding of how each additional LEO satellite improves efficiency. This requires removing a GPS satellite for each additional satellite, posing potential DOP-related issues. To mitigate these issues, only LEO satellites above 30 degrees elevation are selected to ensure DOP does not decrease for each successive LEO satellite added. This warrants the use of OneWeb as it possesses more satellites than Iridium NEXT, guaranteeing at least three satellites above 30 degrees for the duration of the trajectory. Also, only three additional LEO satellites are considered to prevent a standalone LEO solution while GPS is degraded.

6.3.2 Results

As before, each receiver architecture is initialized (or grid-centered for DPE) at the true γ, which is defined in Equation 3.12. The position and velocity process noise is defined using Equation 3.24 with $\sigma_{xyz} = 6\,\mathrm{m/s}^{\frac{3}{2}}$, the same value used in the previous studies. The clock process noise was defined by the PSD coefficients for the High-Quality TCXO presented in Table 5.2. In addition, the number of particles varied from 2000 to 6000 using the grid resolution explained in Section 4.2.1. Figure 6.13 shows the resulting position and velocity RMSEs for each simulated number of particles, where DPE-GPS is depicted as the zero LEO case.

It can be seen that for all numbers of particles and any number of LEO satellites that DPE-GPS-LEO outperforms DPE-GPS in position estimation. This implies that adding LEO satellites to a GNSS DPE architecture greatly reduces the computational burden required to achieve a specified positioning accuracy. In fact, it can be seen that only 2000 particles are needed to achieve the positioning accuracy provided by 6000 particles for DPE-GPS in all LEO satellite cases. Virtually the same can be seen in the velocity RMSE results. In this case, only 2000-3000 particles are needed for all LEO satellite configurations to achieve the same

(a) Position RMSE (b) Velocity RMSE
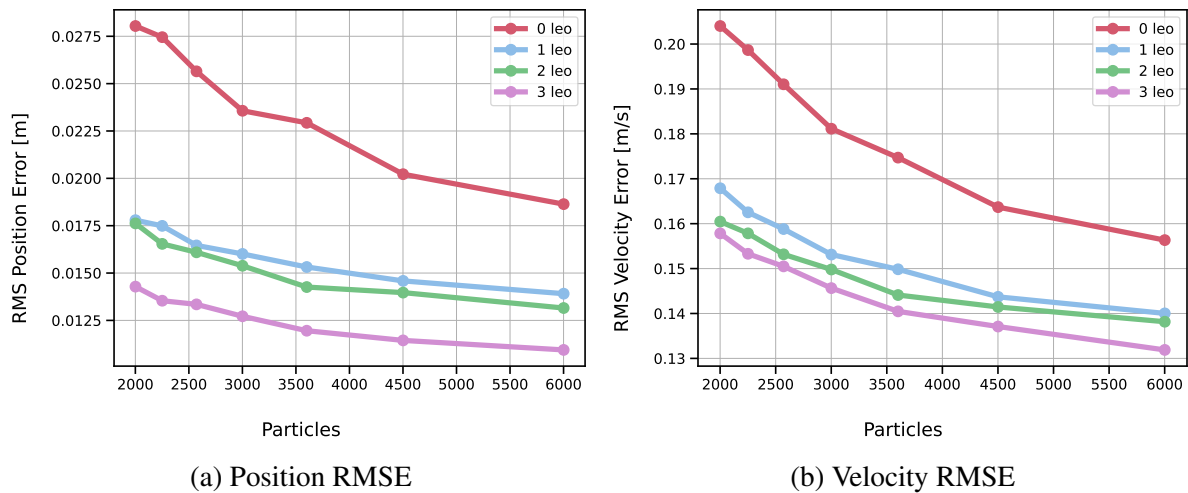
Figure 6.13: Position and Velocity State RMSEs for Dynamic Computational Efficiency Study

accuracy achieved by 6000 particles for DPE-GPS. Overall, it can be concluded that DPE-GPS-LEO requires less computation to achieve the same accuracy as DPE-GPS in position and velocity estimation.

The same general conclusions can be made for the clock state results as well. Figure 6.14 shows the resulting clock bias and clock drift RMSEs for each simulated number of particles, where DPE-GPS is depicted as the zero LEO case. Although the differences between each LEO case are not drastic, the relative performance of DPE-GPS-LEO and DPE-GPS is. It can be seen that better clock state estimation accuracy is achieved using 2000 particles for DPE-GPS-LEO compared to 6000 particles for DPE-GPS. This implies that the computational efficiency of DPE receivers that only estimate clock states (i.e., have previous knowledge of position and velocity) can be greatly improved with only one LEO satellite.

(a) Clock Bias RMSE
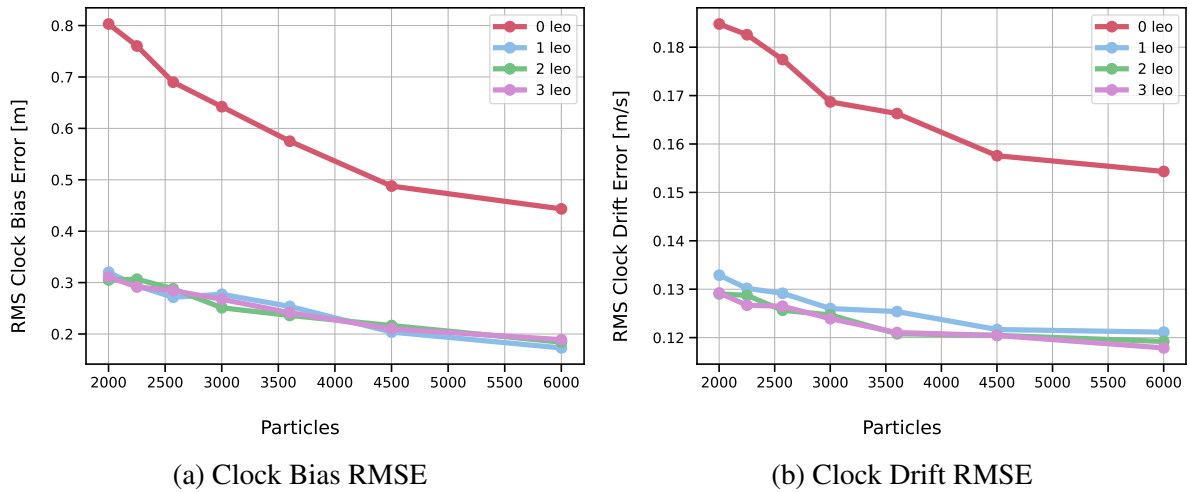
(b) Clock Drift RMSE

Figure 6.14: Clock Bias and Clock Drift State RMSEs for Dynamic Computational Efficiency Study

Although this study is fairly simple, it provides great insight into the potential computational gains of DPE-GPS-LEO. More studies must be conducted to better understand how specific hardware efficiency changes. However, this study generally concludes that LEO-aiding of a GNSS DPE receiver can be more computationally efficient when considering a specified accuracy.

Chapter 7

Conclusions and Future Work

7.1 Conclusions

This thesis begins the exploration of aiding GNSS DPE receiver architectures with LEO PNT sources. In the literature, DPE has been shown to outperform other advanced GNSS receivers but is still susceptible to GNSS interference. This thesis extended the state of the art by further increasing the performance and RFI resilience of DPE with LEO augmentation. Specifically, this was done by modifying a Bayesian DPE approach to accept dedicated LEO PNT signals and opportunistic LEO PNT measurements. The performance of the resulting architectures was evaluated in simulation using a measurement-level and correlator-level simulation environment called Navsim. It was determined that the LEO-aided DPE architectures outperformed all other considered advanced GNSS architectures for various RFI scenarios. This was indicated by the RMSEs associated with each architecture's position, velocity, and clock state estimates. For nearly all cases, these values were lower for the proposed architectures, indicating significant relative performance gains. Further, a probability of tracking metric indicated that these LEO-aided architectures greatly preserve the integrity of received GNSS signals. In fact, the probability of tracking GPS in the highest RFI scenario showed up to an 85.12% performance increase. Considering a 70% probability of tracking threshold for all tested architectures, the proposed DPE architectures survived nearly $10\,\text{dB}$ to $15\,\text{dB}$ more GPS attenuation compared to the VP architectures. Additionally, the robustness of the architectures was illustrated in scenarios with different dynamics and satellite geometries.

In addition, a simple computational efficiency study was conducted. This study concluded that aiding GNSS DPE with dedicated LEO PNT signals can reduce the computational burden

required to estimate a receiver's state with a certain accuracy. Specifically, it was determined that the number of evaluated candidate states and resulting correlations in a DPE architecture could be limited when it is LEO-aided without affecting accuracy. In fact, results imply that LEO-aided DPE architectures only require 1/3 of the candidate states used by a traditional DPE architecture in the tested scenarios.

7.2   Future Work

Regarding future efforts, the author suggests implementing the proposed architectures at the signal level to further understand the computational implications of each. These implementations should inform any modifications regarding parallelization and general receiver hardware selection. In addition, the dedicated LEO PNT architecture should be tested with simulated signals, given dedicated LEO PNT sources are not currently abundant. Regarding the opportunistic LEO PNT architecture, live-sky tests should be conducted. However, an additional receiver must be implemented to measure opportunistic Doppler shift before this can be done. Also, considerations for PNT signals outside of the L-band must be made as new LEO constellations target higher frequency bands. Further, comparisons should be made to other advanced receiver architectures using live-sky data when available.

Bibliography

[1]   Tyler G.R. Reid, Andrew Neish, and Brian Manning. "Localization & Mapping Require-
        ments for Level 2+ Autonomous Vehicles". en. In: *Proceedings of the 2023 International
        Technical Meeting of The Institute of Navigation*. Long Beach, California, Feb. 2023,
        pp. 107–123. DOI: 10.33012/2023.18634. URL: https://www.ion.org/publications/
        abstract.cfm?articleID=18634.

[2]   Robert Tenny and Todd E. Humphreys. "Robust Navigation for Urban Air Mobility".
        en-US. In: *Inside GNSS - Global Navigation Satellite Systems Engineering, Policy, and
        Design* (Mar. 2023). URL: https://insidegnss.com/robust-navigation-for-urban-air-
        mobility/.

[3]   Niels Joubert, Tyler G. R. Reid, and Fergus Noble. "Developments in Modern GNSS and
        Its Impact on Autonomous Vehicle Architectures". In: *2020 IEEE Intelligent Vehicles
        Symposium (IV)*. ISSN: 2642-7214. Oct. 2020, pp. 2029–2036. DOI: 10.1109/IV47402.
        2020.9304840. URL: https://ieeexplore.ieee.org/abstract/document/9304840.

[4]   Alan C O'Connor et al. *Economic Benefits of the Global Positioning System (GPS)*. en.
        Final Report RTI Project Number 0215471. Sponsored by the National Institute of Stan-
        dards and Technology. RTI International, 2019. URL: https://www.nist.gov/document/
        economic-benefits-global-positioning-system-gps-final-report.

[5]   Peter Anthony Iannucci and Todd E. Humphreys. "Fused Low-Earth-Orbit GNSS". en.
        In: *IEEE Transactions on Aerospace and Electronic Systems* (2022). ISSN: 0018-9251,
        1557-9603, 2371-9877. DOI: 10.1109/TAES.2022.3180000. URL: https://ieeexplore.
        ieee.org/document/9789273/.

[6] Dan Elliot. "Next-generation of GPS satellites are headed to space". en. In: *AP News* (Dec. 2018). URL: https://apnews.com/general-news-b05b1b6d22ec4058bf7419744205104b.

[7] Harry W. Jones. "The Recent Large Reduction in Space Launch Cost". In: NTRS Author Affiliations: NASA Ames Research Center NTRS Report/Patent Number: ARC-E-DAA-TN56851 NTRS Document ID: 20200001093 NTRS Research Center: Ames Research Center (ARC). Albuquerque, NM, July 2018. URL: https://ntrs.nasa.gov/citations/20200001093.

[8] Tyler G.R. Reid et al. "Broadband LEO Constellations for Navigation". en. In: *NAVIGATION* 65.2 (2018). _eprint: https://onlinelibrary.wiley.com/doi/pdf/10.1002/navi.234, pp. 205–220. ISSN: 2161-4296. DOI: 10.1002/navi.234. URL: https://onlinelibrary.wiley.com/doi/abs/10.1002/navi.234.

[9] Joshua Morales, Joe Khalife, and Zaher M. Kassas. "Simultaneous Tracking of Orbcomm LEO Satellites and Inertial Navigation System Aiding Using Doppler Measurements". In: *2019 IEEE 89th Vehicular Technology Conference (VTC2019-Spring)*. ISSN: 2577-2465. Apr. 2019, pp. 1–6. DOI: 10.1109/VTCSpring.2019.8746485. URL: https://ieeexplore.ieee.org/abstract/document/8746485.

[10] Sterling Thompson, Scott Martin, and David Bevly. "Single Differenced Doppler Positioning with Low Earth Orbit Signals of Opportunity and Angle of Arrival Estimation". en. In: ISSN: 2330-3646. Jan. 2021, pp. 497–509. DOI: 10.33012/2021.17845. URL: http://www.ion.org/publications/abstract.cfm?jp=p&articleID=17845.

[11] Joshua J. Morales et al. "Inertial Navigation System Aiding with Orbcomm LEO Satellite Doppler Measurements". en. In: Miami, Florida, Oct. 2018, pp. 2718–2725. DOI: 10.33012/2018.16059. URL: https://www.ion.org/publications/abstract.cfm?articleID=16059.

[12] Z. Kassas, J. Morales, and J. Khalife. "New-Age Satellite-Based Navigation - STAN: Simultaneous Tracking and Navigation with LEO Satellite Signals". en. In: *Inside GNSS* 14.4 (Jan. 2019). URL: https://par.nsf.gov/biblio/10180917-new-age-satellite-based-navigation-stan-simultaneous-tracking-navigation-leo-satellite-signals.

[13] Todd E. Humphreys et al. "Signal Structure of the Starlink Ku-Band Downlink". In: *IEEE Transactions on Aerospace and Electronic Systems* 59.5 (Oct. 2023). Conference Name: IEEE Transactions on Aerospace and Electronic Systems, pp. 6016–6030. ISSN: 1557-9603. DOI: 10.1109/TAES.2023.3268610. URL: https://ieeexplore.ieee.org/abstract/document/10107477.

[14] Zaher M Kassas, Nadim Khairallah, and Sharbel Kozhaya. "Ad astra: Simultaneous tracking and navigation with megaconstellation LEO satellites". In: *IEEE Aerospace and Electronic Systems Magazine* (2024). Publisher: IEEE.

[15] Min Li et al. "LEO-Constellation-Augmented Multi-GNSS Real-Time PPP for Rapid Re-Convergence in Harsh Environments". In: *GPS Solutions* 26 (2022). Publisher: Springer, pp. 1–12.

[16] Muyuan Jiang et al. "LEO Doppler-Aided GNSS Position Estimation". In: *GPS Solutions* 26.1 (2022). Publisher: Springer, p. 31.

[17] Li Cheng et al. "Structure and Performance Analysis of Signal Acquisition and Doppler Tracking in LEO Augmented GNSS Receiver". In: *Sensors* 21.2 (2021). Publisher: MDPI, p. 525.

[18] Nadim Khairallah and Zaher M. Kassas. "Ephemeris Tracking and Error Propagation Analysis of LEO Satellites With Application to Opportunistic Navigation". en. In: *IEEE Transactions on Aerospace and Electronic Systems* 60.2 (Apr. 2024), pp. 1242–1259. ISSN: 0018-9251, 1557-9603, 2371-9877. DOI: 10.1109/TAES.2023.3325797. URL: https://ieeexplore.ieee.org/document/10288195/.

[19] F. S. Prol et al. "Position, navigation, and timing (PNT) through low earth orbit (LEO) satellites: a survey on current status, challenges, and opportunities". In: *IEEE access : practical innovations, open solutions* 10 (2022), pp. 83971–84002. DOI: 10.1109/ACCESS.2022.3194050.

[20] Zaher M. Kassas and Todd E. Humphreys. "Observability Analysis of Collaborative Opportunistic Navigation With Pseudorange Measurements". In: *IEEE Transactions on Intelligent Transportation Systems* 15.1 (Feb. 2014). Conference Name: IEEE Transactions

on Intelligent Transportation Systems, pp. 260–273. ISSN: 1558-0016. DOI: 10.1109/ TITS.2013.2278293. URL: https://ieeexplore.ieee.org/document/6605632.

[21]   Robert J Danchik. "An Overview of Transit Development". In: *Johns Hopkins APL technical digest* 19.1 (1998). Publisher: JOHN HOPKINS UNIV APPLIED PHYSICS LABORATORY, p. 19.

[22]   *Iridium Launches Breakthrough Alternative Global Positioning System (GPS) Service.* en. Press Release. May 2016. URL: https://www.globenewswire.com/news-release/ 2016/05/23/842381/15411/en/Iridium-Launches-Breakthrough-Alternative-Global-Positioning-System-GPS-Service.html.

[23]   Greg Clark et al. *UK Space Strategy and UK Satellite Infrastructure*. en. Tech. rep. HC 100. House of Commons Science and Technology Committee, Oct. 2022. URL: https: //committees.parliament.uk/publications/31490/documents/176763/default/.

[24]   *Globalstar-Echo Ridge Agreement Advances New Assured PNT Technology and Service - Globalstar, Inc.* en. Press Release. July 2019. URL: https://investors.globalstar.com/ news-releases/news-release-details/globalstar-echo-ridge-agreement-advances-new-assured-pnt/.

[25]   Tyler G.R. Reid et al. "Satellite Navigation for the Age of Autonomy". en. In: *2020 IEEE/ION Position, Location and Navigation Symposium (PLANS)*. Portland, OR, USA: IEEE, Apr. 2020, pp. 342–352. ISBN: 978-1-72810-244-3. DOI: 10.1109/PLANS46316. 2020.9109938. URL: https://ieeexplore.ieee.org/document/9109938/.

[26]   Paul Anderson, George Schmitt, and Patrick Shannon. "Low Earth Orbit Navigation System (LEONS): Scalable GNSS-Independent Time Transfer and Positioning for Space Users". en. In: *Proceedings of the 2023 International Technical Meeting of The Institute of Navigation*. ISSN: 2330-3646. Jan. 2023, pp. 65–76. DOI: 10.33012/2023.18591. URL: http://www.ion.org/publications/abstract.cfm?jp=p&articleID=18591.

[27]   Inside GNSS. *Xona Raises $19 Million Series A for LEO Satellite Network*. en-US. May 2024. URL: https://insidegnss.com/xona-raises-19-million-series-a-for-leo-satellite-network/.

[28]   Inside GNSS. *TrustPoint Secures AFWERX Phase II Contract to Advance GNSS Solutions for the US Air Force*. en-US. Apr. 2024. URL: https://insidegnss.com/trustpoint-secures-afwerx-phase-ii-contract-to-advance-gnss-solutions-for-the-us-air-force/.

[29]   Pau Closas, Carles Fernández-Prades, and Juan Fernandez-Rubio. "Maximum Likelihood Estimation of Position in GNSS". In: *Signal Processing Letters, IEEE* 14 (June 2007), pp. 359–362. DOI: 10.1109/LSP.2006.888360.

[30]   Pau Closas, Carles Fernandez-Prades, and Juan A. Fernandez-Rubio. "CramÉr–Rao Bound Analysis of Positioning Approaches in GNSS Receivers". In: *IEEE Transactions on Signal Processing* 57.10 (Oct. 2009). Conference Name: IEEE Transactions on Signal Processing, pp. 3775–3786. ISSN: 1941-0476. DOI: 10.1109/TSP.2009.2025083.

[31]   Adrià Gusi-Amigó et al. "Ziv-Zakai Bound for Direct Position Estimation". en. In: *NAVIGATION* 65.3 (Sept. 2018), pp. 463–475. ISSN: 0028-1522, 2161-4296. DOI: 10.1002/navi.259. URL: https://onlinelibrary.wiley.com/doi/10.1002/navi.259.

[32]   Jürgen Dampf, Christian A. Lichtenberger, and Thomas Pany. "Probability Analysis for Bayesian Direct Position Estimation in a Real-Time GNSS Software Receiver". en. In: Miami, Florida, Oct. 2019, pp. 3543–3566. DOI: 10.33012/2019.16935. URL: https://www.ion.org/publications/abstract.cfm?articleID=16935.

[33]   Arthur Hsi-Ping Chu, Shubhendra Vikram Singh Chauhan, and Grace Xingxin Gao. "GPS Multireceiver Direct Position Estimation for Aerial Applications". In: *IEEE Transactions on Aerospace and Electronic Systems* 56.1 (Feb. 2020). Conference Name: IEEE Transactions on Aerospace and Electronic Systems, pp. 249–262. ISSN: 1557-9603. DOI: 10.1109/TAES.2019.2915393.

[34]   Kirsten Strandjord and Faith Cornish. "Direct Positioning Estimation Beyond the Constellation Using Falcon Gold Data Collected on Highly Elliptical Orbit". en. In: ISSN: 2330-3646. Jan. 2023, pp. 679–691. DOI: 10.33012/2023.18662. URL: http://www.ion.org/publications/abstract.cfm?jp=p&articleID=18662.

[35]   Shuo Tang et al. "Precise Direct Position Estimation: Validation Experiments". In: *2023 IEEE/ION Position, Location and Navigation Symposium (PLANS)*. ISSN: 2153-3598. Apr. 2023, pp. 911–916. DOI: 10.1109/PLANS53410.2023.10140046.

[36]   P. Closas et al. "Evaluation of GNSS Direct Position Estimation in Realistic Multipath Channels". en. In: ISSN: 2331-5954. Sept. 2015, pp. 3693–3701. URL: http://www.ion. org/publications/abstract.cfm?jp=p&articleID=12968.

[37]   Matthew Peretic and Grace X. Gao. "Design of a parallelized direct position estimation-based GNSS receiver". en. In: *NAVIGATION: Journal of the Institute of Navigation* 68.1 (Mar. 2021). Publisher: Institute of Navigation Section: Original Article, pp. 21–39. ISSN: 0028-1522, 2161-4296. DOI: 10.1002/navi.402. URL: https://navi.ion.org/ content/68/1/21.

[38]   Jürgen Dampf et al. "Particle Filter Algorithms and Experiments for High Sensitivity GNSS Receivers". In: *Proceedings of the 6th international Colloquium—Scientific and fundamental aspects of GNSS/Galileo, Valencia, Spain*. 2017, pp. 25–27.

[39]   Jürgen Dampf, Kathrin Frankl, and Thomas Pany. "Optimal Particle Filter Weight for Bayesian Direct Position Estimation in a GNSS Receiver". en. In: *Sensors* 18.8 (Aug. 2018). Number: 8 Publisher: Multidisciplinary Digital Publishing Institute, p. 2736. ISSN: 1424-8220. DOI: 10.3390/s18082736. URL: https://www.mdpi.com/1424-8220/18/8/2736.

[40]   Pau Closas and Carles Fernandez-Prades. "Bayesian nonlinear filters for Direct Position Estimation". en. In: *2010 IEEE Aerospace Conference*. Big Sky, MT: IEEE, Mar. 2010, pp. 1–12. ISBN: 978-1-4244-3887-7. DOI: 10.1109/AERO.2010.5446676. URL: http: //ieeexplore.ieee.org/document/5446676/.

[41]   Pratap Misra and Per Enge. *Global Positioning System: Signals, Measurements, and Performance*. eng. Revised 2. ed., 2. printing, revised and updated. Lincoln, Mass: Ganga-Jamuna Press, 2012. ISBN: 978-0-9709544-2-8.

[42] *The Global Positioning System: A Shared National Asset*. Washington, D.C.: National Academies Press, May 1995. ISBN: 978-0-309-05283-2. DOI: 10.17226/4920. URL: http://www.nap.edu/catalog/4920.

[43] Bill Clinton. *Press Release - U.S. Global Positioning System Policy*. Mar. 1996. URL: https://clintonwhitehouse4.archives.gov/WH/EOP/OSTP/html/gps-factsheet.html.

[44] Bill Clinton. *The United States' Decision to Stop Degrading Global Positioning System Accuracy*. May 2000. URL: https://clintonwhitehouse4.archives.gov/WH/EOP/OSTP/html/0053_2.html.

[45] *Global Positioning System (GPS) Overview — Navigation Center*. Mar. 2024. URL: https://www.navcen.uscg.gov/global-positioning-system-overview.

[46] *GPS.gov: Control Segment*. Aug. 2021. URL: https://www.gps.gov/systems/gps/control/.

[47] European Union Agency for the Space Programme. *EUSPA EO and GNSS Market Report.2024 / Issue 2* . en. LU: Publications Office, 2024. URL: https://data.europa.eu/doi/10.2878/73092.

[48] Jane Bondar. *How to Build a GPS App: Tech Requirements & Pitfalls Explained – NIX United*. en. Nov. 2021. URL: https://nix-united.com/blog/how-to-build-a-gps-app-tech-requirements-pitfalls-explained/.

[49] Robert Gold. "Optimal binary sequences for spread spectrum multiplexing (Corresp.)" In: *IEEE Transactions on Information Theory* 13.4 (1967). Publisher: IEEE, pp. 619–621.

[50] *NAVSTAR GPS Space Segment/Navigation User Segment Interfaces - IS-GPS-200*. en. Aug. 2022. URL: https://www.navcen.uscg.gov/sites/default/files/pdf/gps/IS-GPS-200N.pdf.

[51] *GPS Navigation Message - Navipedia*. Jan. 2021. URL: https://gssc.esa.int/navipedia/index.php?title=GPS_Navigation_Message#L1_C/A.

[52] Kai Borre et al. *A Software-Defined GPS and Galileo Receiver: a Single-Frequency Approach*. Springer Science & Business Media, 2007.

[53] Elliott D Kaplan and Christopher Hegarty. *Understanding GPS/GNSS: Principles and Applications*. Artech House, 2017.

[54] Matthew Lashley. "Modeling and Performance Analysis of GPS Vector Tracking Algorithms". en. Accepted: 2009-12-17T15:21:17Z. PhD thesis. Auburn University, Dec. 2009. URL: https://etd.auburn.edu//handle/10415/2009.

[55] John A. Klobuchar. "Ionospheric Time-Delay Algorithm for Single-Frequency GPS Users". In: *IEEE Transactions on Aerospace and Electronic Systems* AES-23.3 (May 1987). Conference Name: IEEE Transactions on Aerospace and Electronic Systems, pp. 325–331. ISSN: 1557-9603. DOI: 10.1109/TAES.1987.310829. URL: https://ieeexplore.ieee.org/document/4104345.

[56] H. W. Janes, R. B. Langley, and S. P. Newby. "Analysis of Tropospheric Delay Prediction Models: Comparisons with Ray-Tracing and Implications for GPS Relative Positioning". en. In: *Bulletin géodésique* 65.3 (Sept. 1991), pp. 151–161. ISSN: 1432-1394. DOI: 10.1007/BF00806344. URL: https://doi.org/10.1007/BF00806344.

[57] Angelo Joseph. "Measuring GNSS Signal Strength: What is the difference between SNR and C/N0?" In: *InsideGNSS* (Nov. 2010). URL: https://insidegnss.com/wp-content/uploads/2018/01/novdec10-Solutions.pdf.

[58] Emanuela Falletti, Marco Pini, and Letizia Lo Presti. "Low Complexity Carrier-to-Noise Ratio Estimators for GNSS Digital Receivers". en. In: *IEEE Transactions on Aerospace and Electronic Systems* 47.1 (Jan. 2011), pp. 420–437. ISSN: 0018-9251. DOI: 10.1109/TAES.2011.5705684. URL: http://ieeexplore.ieee.org/document/5705684/.

[59] Robert N. Crane. "A Simplified Method for Deep Coupling of GPS and Inertial Data". en. In: Jan. 2007, pp. 311–319. URL: http://www.ion.org/publications/abstract.cfm?jp=p&articleID=7162.

[60] Mark L Psiaki and Hee Jung. "Extended Kalman Filter Methods for Tracking Weak GPS Signals". en. In: (2002).

[61] José A Del Peral-Rosado et al. "Kalman Filter-based Architecture for Robust and High-Sensitivity Tracking in GNSS Receivers". In: *2010 5th ESA workshop on satellite navigation technologies and european workshop on GNSS signals and signal processing (NAVITEC)*. IEEE, 2010, pp. 1–8.

[62] Jong-Hoon Won, Thomas Pany, and Bernd Eissfeller. "Characteristics of Kalman filters for GNSS Signal Tracking Loop". In: *IEEE Transactions on Aerospace and Electronic Systems* 48.4 (2012). Publisher: IEEE, pp. 3671–3681.

[63] James J Spilker Jr. *Vector Delay Lock Loop Processing of Radiolocation Transmitter Signals*. 1995.

[64] Thomas Pany and Bernd Eissfeller. "Use of a Vector Delay Lock Loop Receiver for GNSS Signal Power Analysis in Bad Signal Conditions". In: *Proceedings of IEEE/ION PLANS 2006*. 2006, pp. 893–903.

[65] Jing Liu et al. "Vector Tracking Loops in GNSS Receivers for Dynamic Weak Signals". In: *Journal of Systems Engineering and Electronics* 24.3 (2013). Publisher: BIAI, pp. 349–364.

[66] Yu Luo et al. "Multipath Effects on Vector Tracking Algorithm for GNSS Signal". In: *Science China. Information Sciences* 57.10 (2014). Publisher: Springer Nature BV, pp. 1–13.

[67] Li-Ta Hsu et al. "Multipath Mitigation and NLOS Detection Using Vector Tracking in Urban Environments". In: *Gps Solutions* 19 (2015). Publisher: Springer, pp. 249–262.

[68] Scott Martin. "GPS Carrier Phase Tracking in Difficult Environments Using Vector Tracking For Precise Positioning and Vehicle Attitude Estimation". en. Accepted: 2017-04-25T15:47:40Z. PhD thesis. Apr. 2017. URL: https://etd.auburn.edu//handle/10415/5692.

[69] Yaakov Bar-Shalom, X Rong Li, and Thiagalingam Kirubarajan. *Estimation with Applications to Tracking and Navigation: Theory Algorithms and Software*. John Wiley & Sons, 2004.

[70] Robert Grover Brown and Patrick Y. C. Hwang. *Introduction to Random Signals and Applied Kalman Filtering with MATLAB Exercises*. eng. 4. ed. Hoboken, NJ: Wiley, 2012. ISBN: 978-0-470-60969-9.

[71] Pau Closas and Grace Gao. "Direct Position Estimation". In: *Position, Navigation, and Timing Technologies in the 21st Century: Integrated Satellite Navigation, Sensor Systems, and Civil Applications* 1 (2020). Publisher: Wiley Online Library, pp. 529–550.

[72] Arthur Hsi-Ping Chu. "GPS Multi-Receiver Direct Position Estimation for Aerial Applications". text. University of Illinois at Urbana-Champaign, July 2018. URL: https://hdl.handle.net/2142/101449.

[73] Pau Closas and Adria Gusi-Amigo. "Direct Position Estimation of GNSS Receivers: Analyzing main results, architectures, enhancements, and challenges". In: *IEEE Signal Processing Magazine* 34.5 (Sept. 2017). Conference Name: IEEE Signal Processing Magazine, pp. 72–84. ISSN: 1558-0792. DOI: 10.1109/MSP.2017.2718040.

[74] R.A. Iltis and L. Mailaender. "An adaptive multiuser detector with joint amplitude and delay estimation". In: *IEEE Journal on Selected Areas in Communications* 12.5 (June 1994). Conference Name: IEEE Journal on Selected Areas in Communications, pp. 774–785. ISSN: 1558-0008. DOI: 10.1109/49.298051. URL: https://ieeexplore.ieee.org/document/298051.

[75] Alon Amar and Anthony J. Weiss. "New Asymptotic Results on Two Fundamental Approaches to Mobile Terminal Location". In: *2008 3rd International Symposium on Communications, Control and Signal Processing*. Mar. 2008, pp. 1320–1323. DOI: 10.1109/ISCCSP.2008.4537430. URL: https://ieeexplore.ieee.org/abstract/document/4537430.

[76] Jürgen Dampf et al. "More Than We Ever Dreamed Possible: Processor Technology for GNSS Software Receivers in the Year 2015". In: *Inside GNSS* 10.4 (2015), pp. 62–72.

[77] Thomas Pany et al. "The Multi-Sensor Navigation Analysis Tool (MuSNAT)–Architecture, LiDAR, GPU/CPU GNSS Signal Processing". In: *Proceedings of the 32nd international technical meeting of the satellite division of the institute of navigation (ION GNSS+ 2019)*. 2019, pp. 4087–4115.

[78] Mark G Petovello et al. "Architecture and Benefits of an Advanced GNSS Software Receiver". In: *Journal of Global Positioning Systems* 7.2 (2008), pp. 156–168.

[79] Bin Huang et al. "STARx–a GPU Based Multi-System Full-Band Real-Time GNSS Software Receiver". In: *Proceedings of the 26th international technical meeting of the satellite division of the institute of navigation (ION GNSS+ 2013)*. 2013, pp. 1549–1559.

[80] Jos Elfring, Elena Torta, and René van de Molengraft. "Particle Filters: A Hands-On Tutorial". en. In: *Sensors* 21.2 (Jan. 2021). Number: 2 Publisher: Multidisciplinary Digital Publishing Institute, p. 438. ISSN: 1424-8220. DOI: 10.3390/s21020438. URL: https://www.mdpi.com/1424-8220/21/2/438.

[81] Tiancheng Li, Miodrag Bolic, and Petar M Djuric. "Resampling Methods for Particle Filtering: Classification, Implementation, and Strategies". In: *IEEE Signal processing magazine* 32.3 (2015). Publisher: IEEE, pp. 70–86.

[82] *commaai/laika: Simple Python GNSS processing library*. URL: https://github.com/commaai/laika/tree/master.

[83] International GNSS Service (IGS). *GNSS Final Combined Orbit Solution Product*. 1992. DOI: 10.5067/GNSS/GNSS_IGSORB_001. URL: http://cddis.gsfc.nasa.gov/Data_and_Derived_Products/GNSS/gnss_igsorb.html.

[84] Brandon Rhodes. *Skyfield: Generate high precision research-grade positions for stars, planets, moons, and Earth satellites*. original-date: 2013-01-30T21:19:21Z. Feb. 2020. URL: https://github.com/skyfielders/python-skyfield.

[85] David Vallado and Paul Crawford. "SGP4 Orbit Determination". en. In: *AIAA/AAS Astrodynamics Specialist Conference and Exhibit*. Honolulu, Hawaii: American Institute of Aeronautics and Astronautics, Aug. 2008. ISBN: 978-1-62410-001-7. DOI: 10.2514/6.2008-6770. URL: https://arc.aiaa.org/doi/10.2514/6.2008-6770.

[86] Mustafa Cavcar. "The International Standard Atmosphere (ISA)". In: *Anadolu University, Turkey* 30.9 (2000), pp. 1–6.

[87]   J Saastamoinen. "Atmospheric correction for the troposphere and stratosphere in radio ranging satellites". In: *The use of artificial satellites for geodesy* 15 (1972). Publisher: Wiley Online Library, pp. 247–251.

[88]   Lorenzo Galleani. "A tutorial on the two-state model of the atomic clock noise". en. In: *Metrologia* 45.6 (Dec. 2008), S175. ISSN: 0026-1394. DOI: 10.1088/0026-1394/45/6/S23. URL: https://dx.doi.org/10.1088/0026-1394/45/6/S23.

[89]   Naser El-Sheimy, Haiying Hou, and Xiaoji Niu. "Analysis and Modeling of Inertial Sensors Using Allan Variance". In: *IEEE Transactions on Instrumentation and Measurement* 57.1 (Jan. 2008). Conference Name: IEEE Transactions on Instrumentation and Measurement, pp. 140–149. ISSN: 1557-9662. DOI: 10.1109/TIM.2007.908635. URL: https://ieeexplore.ieee.org/abstract/document/4404126.

[90]   Akram Al-Hourani and Ismail Guvenc. "On modeling satellite-to-ground path-loss in urban environments". In: *IEEE Communications Letters* 25.3 (2020). Publisher: IEEE, pp. 696–700.

[91]   Paul Groves. *Principles of GNSS, Inertial, and Multi-sensor Integrated Navigation Systems*. en. Second. Vol. 39. Apr. 2012. URL: https://www.emerald.com/insight/content/doi/10.1108/ir.2012.04939caa.011/full/html.

[92]   Inside GNSS. *New GNSS-Independent Receiver Generates Nanosecond Timing, Meter-Level Accuracy from Low-Earth Orbit Satellite Signals*. en-US. Feb. 2021. URL: https://insidegnss.com/new-gnss-independent-receiver-generates-nanosecond-timing-meter-level-accuracy-from-low-earth-orbit-satellite-signals/.

[93]   Tim Flohrer, Holger Krag, and Heiner Klinkrad. "Assessment and categorization of TLE orbit errors for the US SSN catalogue". In: *Risk (Concord, NH)* 8.9 (2008), pp. 10–11.

Appendix A

Commercial Airliner Study

A.1 Static Scenario

The same scenario outlined in Section 6.1 was repeated for a static aerial vehicle on the ground. In this scenario, each receiver architecture is initialized (or grid-centered for DPE) at the true γ. The position and velocity process noise is defined with $\sigma_{xyz} = 6\,\mathrm{m/s}^{\frac{3}{2}}$. This choice of σ_{xyz} may seem peculiar given the vehicle is static; however, it is chosen because each architecture is assumed to be incapable of dynamically tuning its process noise covariance. Therefore, $\sigma_{xyz} = 6\,\mathrm{m/s}^{\frac{3}{2}}$ can consider dynamic and static scenarios, whereas a small value could only be used in static scenarios. The clock process noise was defined by the PSD coefficients for the High-Quality TCXO presented in Table 5.2.

Figure A.1 shows the resulting position and velocity RMSEs, Figure A.2 shows the resulting clock state RMSEs, and Figure A.3 and Table A.1 show the probability of tracking GPS for each simulated GPS C/N$_0$ attenuation.
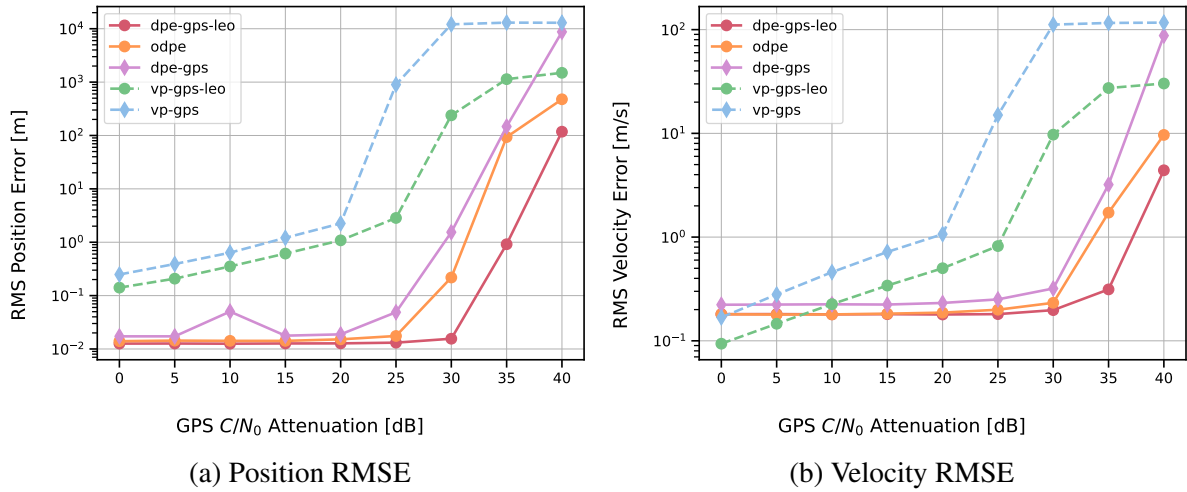

(a) Position RMSE

(b) Velocity RMSE

Figure A.1: Position and Velocity State RMSEs for Static Commercial Airliner Study

(a) Clock Bias RMSE
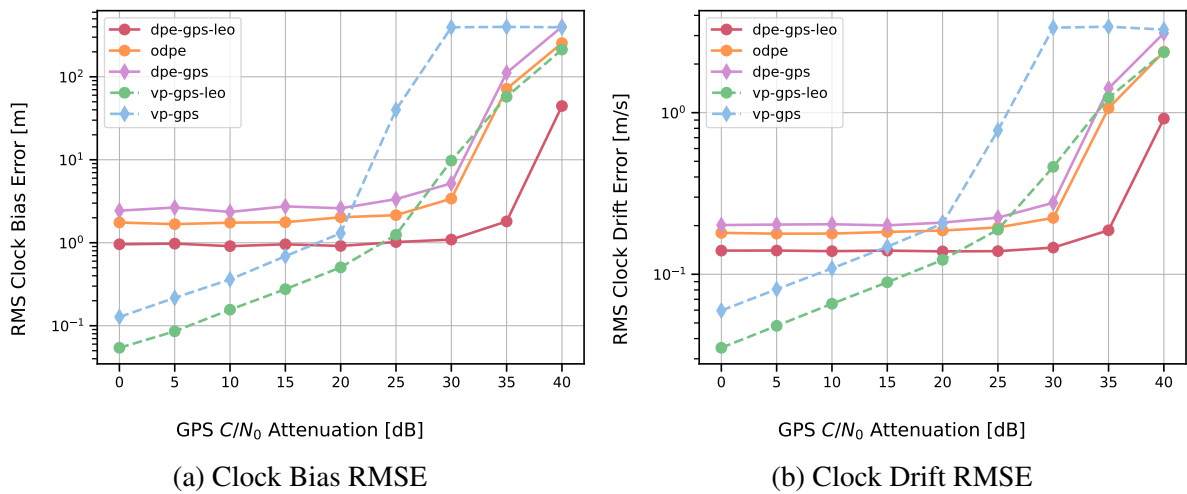
(b) Clock Drift RMSE

Figure A.2: Clock Bias and Clock Drift State RMSEs for Static Commercial Airliner Study
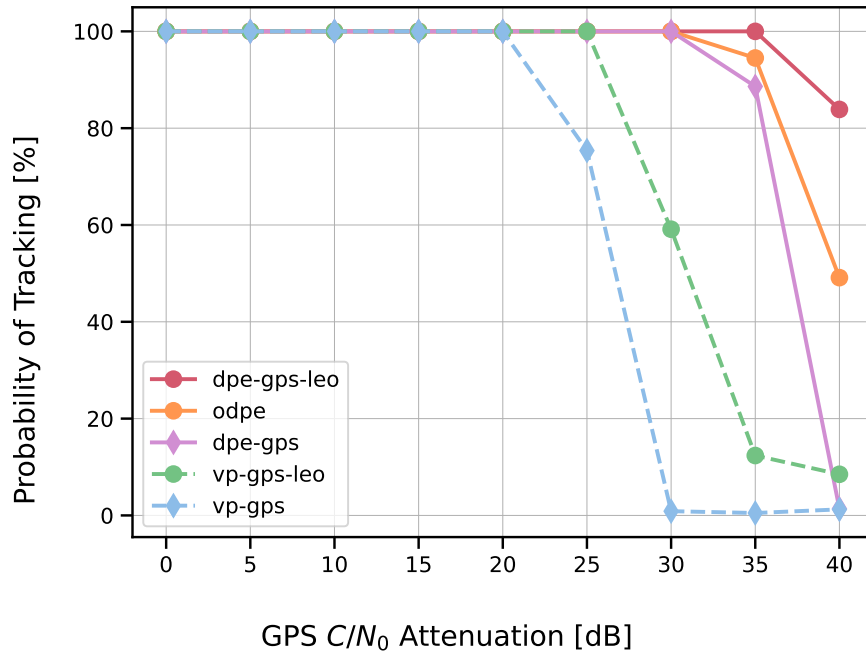
Figure A.3: Probability of Tracking GPS for Static Commercial Airliner Study

Table A.1: Probability of Tracking GPS in High RFI for Static Commercial Airliner Study

GPS C/N$_0$ Attenuation	DPE-GPS-LEO	ODPE	DPE-GPS	VP-GPS-LEO	VP-GPS
20 dB	100%	100%	100%	100%	100%
25 dB	100%	100%	100%	100%	75.4%
30 dB	100%	100%	100%	59.1%	0.88%
35 dB	100%	94.5%	88.6%	12.4%	0.50%
40 dB	83.9%	49.1%	1.38%	8.50%	1.25%

A.2 Orbcomm Proxy LEO Constellation Scenario

The same scenario outlined in Section 6.1 was repeated for a dynamic aerial vehicle whose LEO proxy constellation was changed to Orbcomm. Figure A.4 and Table A.2 depict the satellite geometry characteristics resulting from this change.
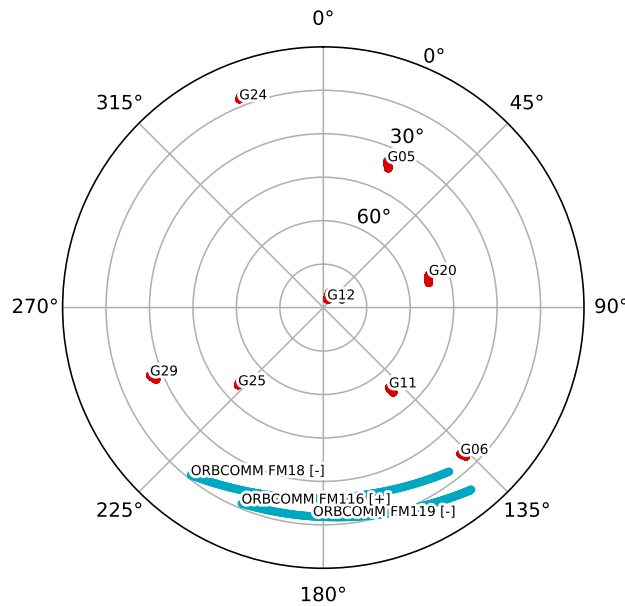

Figure A.4: GPS and LEO (Orbcomm) Skyplot for Commercial Airliner Study

Table A.2: Commercial Airliner Study GPS and LEO (Orbcomm) Dilution of Precision

Min./Max.	GDOP	HDOP	VDOP	TDOP	# GPS SV	# LEO SV
Min.	1.51	0.53	1.31	0.52	8	1
Max.	1.98	0.60	1.74	0.73	8	3

Figure A.5 shows the resulting position and velocity RMSEs, Figure A.6 shows the resulting clock state RMSEs, and Figure A.7 and Table A.3 show the probability of tracking GPS for each simulated GPS C/N$_0$ attenuation.
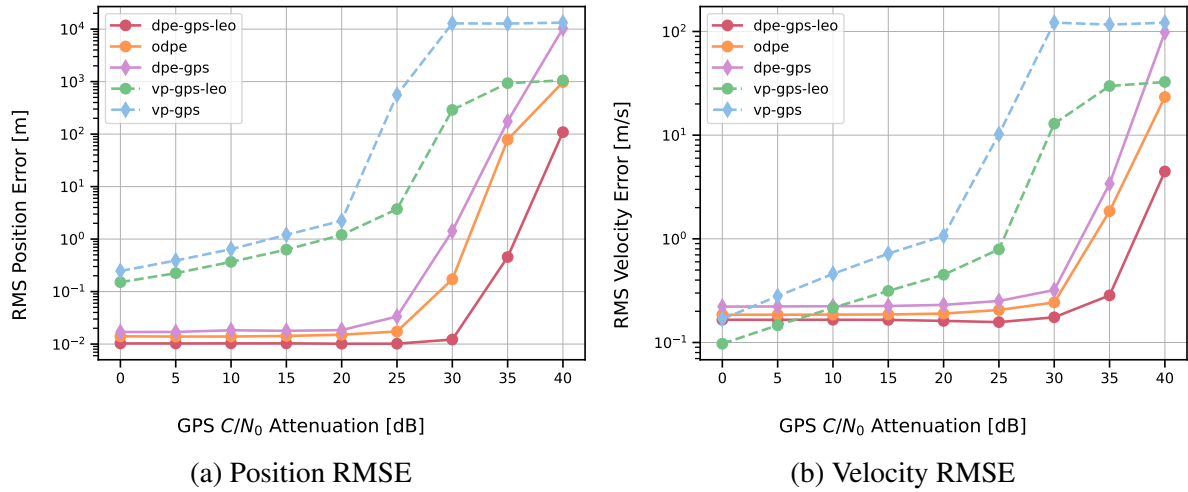

(a) Position RMSE

(b) Velocity RMSE

Figure A.5: Position and Velocity State RMSEs for Orbcomm Dynamic Commercial Airliner Study

(a) Clock Bias RMSE
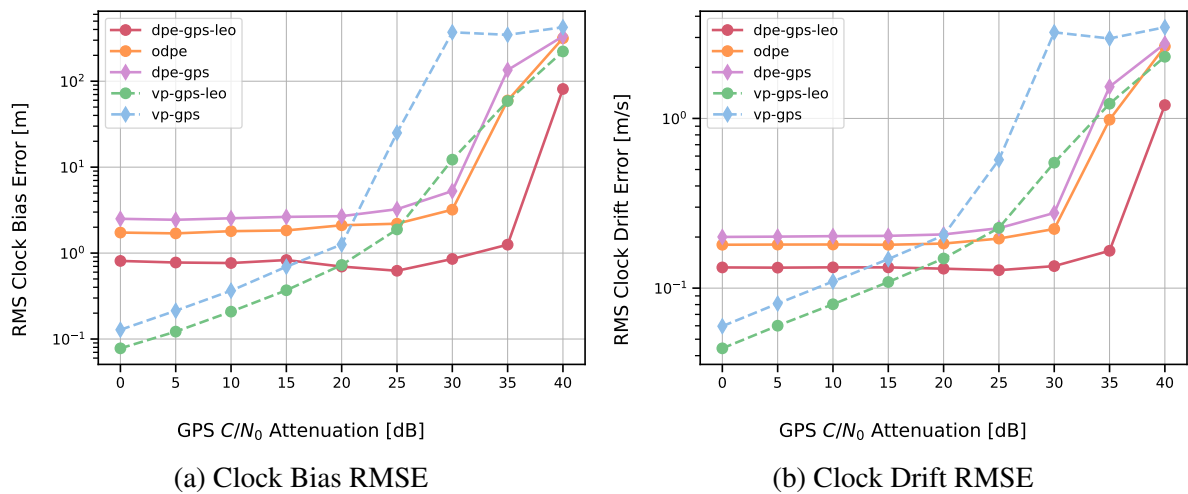
(b) Clock Drift RMSE

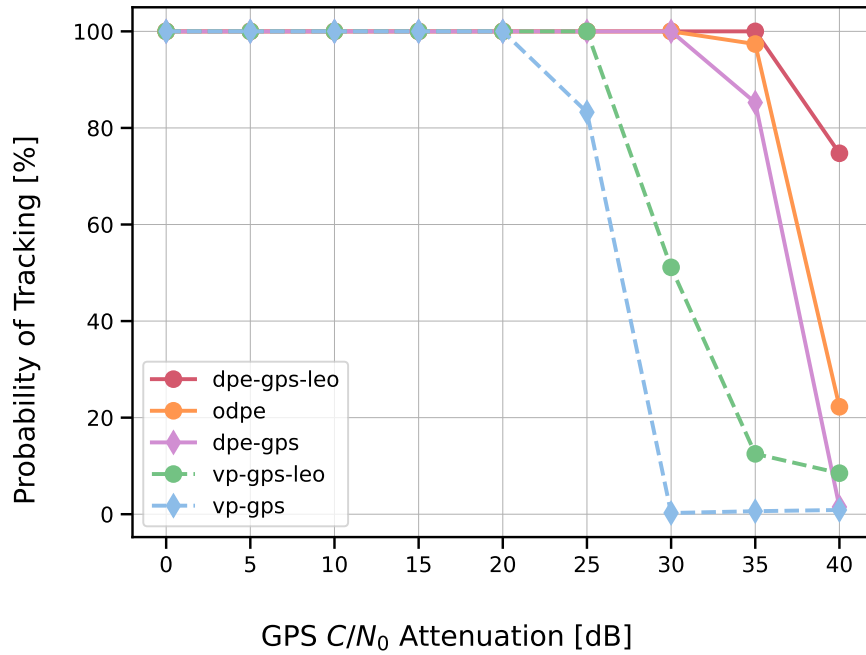Figure A.6: Clock Bias and Clock Drift State RMSEs for Orbcomm Dynamic Commercial Airliner Study

Figure A.7: Probability of Tracking GPS for Orbcomm Dynamic Commercial Airliner Study

Table A.3: Probability of Tracking GPS in High RFI for Orbcomm Dynamic Commercial Airliner Study

GPS C/N$_0$ Attenuation	DPE-GPS-LEO	ODPE	DPE-GPS	VP-GPS-LEO	VP-GPS
20 dB	100%	100%	100%	100%	100%
25 dB	100%	100%	100%	100%	83.3%
30 dB	100%	100%	100%	51.1%	0.25%
35 dB	100%	97.4%	85.3%	12.5%	0.63%
40 dB	74.8%	22.3%	1.50%	8.50%	0.88%

Appendix B

Ground Vehicle Study

B.1 Static Scenario

The same scenario outlined in Section 6.2 was repeated for a static ground vehicle. In this scenario, each receiver architecture is initialized (or grid-centered for DPE) at the true γ. The position and velocity process noise is defined with $\sigma_{xyz} = 6\,\mathrm{m/s^{\frac{3}{2}}}$. This choice of σ_{xyz} is explained in Section A.1. The clock process noise was defined by the PSD coefficients for the High-Quality TCXO presented in Table 5.2.

Figure B.1 shows the resulting position and velocity RMSEs, Figure B.2 shows the resulting clock state RMSEs, and Figure B.3 and Table B.1 show the probability of tracking GPS for each simulated GPS C/N$_0$ attenuation.
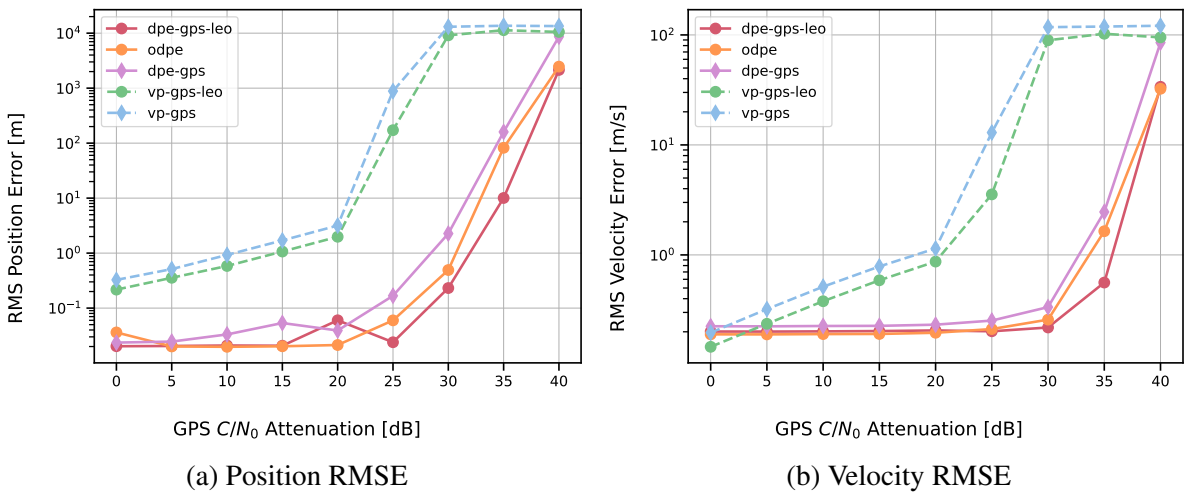

(a) Position RMSE   (b) Velocity RMSE

Figure B.1: Position and Velocity State RMSEs for Static Ground Vehicle Study

(a) Clock Bias RMSE
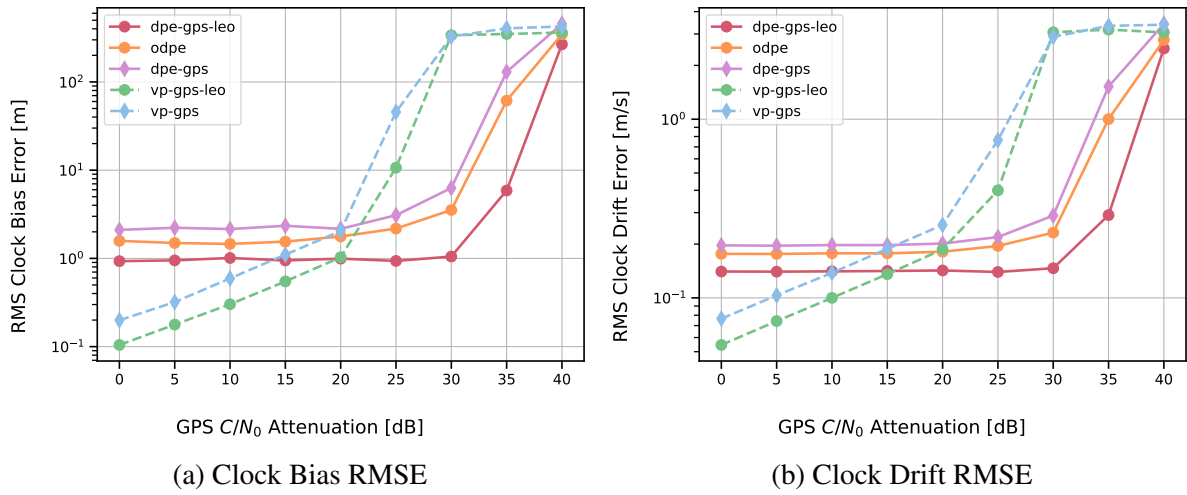
(b) Clock Drift RMSE

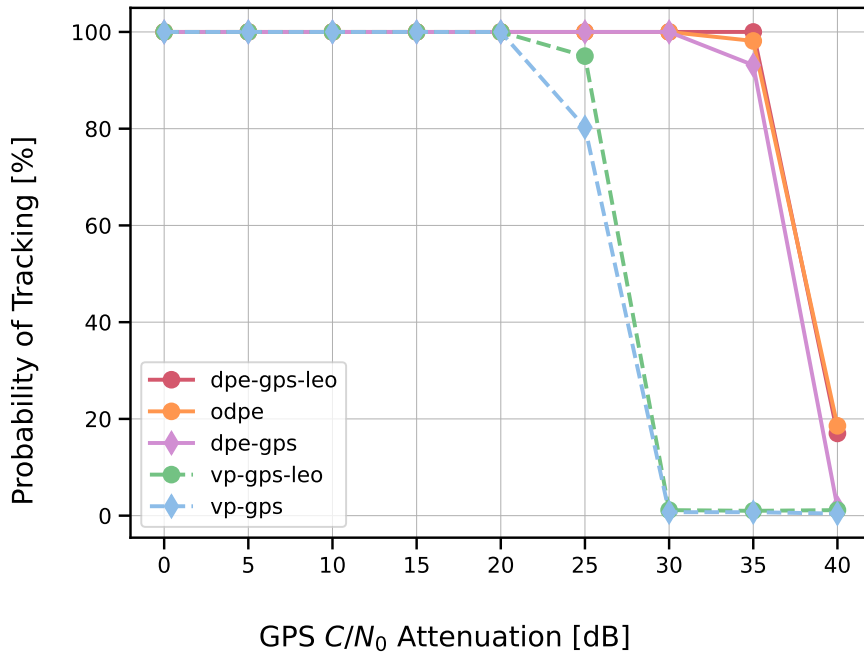Figure B.2: Clock Bias and Clock Drift State RMSEs for Static Ground Vehicle Study

Figure B.3: Probability of Tracking GPS for Static Ground Vehicle Study

Table B.1: Probability of Tracking GPS in High RFI for Static Ground Vehicle Study

GPS C/N$_0$ Attenuation	DPE-GPS-LEO	ODPE	DPE-GPS	VP-GPS-LEO	VP-GPS
20 dB	100%	100%	100%	100%	100%
25 dB	100%	100%	100%	95.0%	80.3%
30 dB	100%	100%	100%	1.14%	0.71%
35 dB	100%	98.1%	93.1%	1.00%	0.71%
40 dB	17.0%	18.6%	1.71%	1.14%	0.43%

B.2   Orbcomm Proxy LEO Constellation Scenario

The same scenario outlined in Section 6.2 was repeated for a dynamic ground vehicle whose LEO proxy constellation was changed to Orbcomm. Figure B.4 and Table B.2 depict the satellite geometry characteristics resulting from this change.
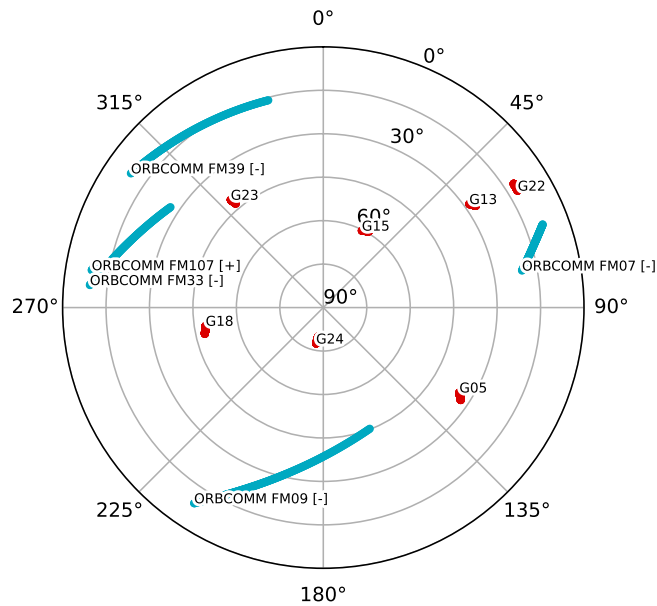

Figure B.4: GPS and LEO Skyplot (Orbcomm) for Ground Vehicle Study

Table B.2: Ground Vehicle Study GPS and LEO (Orbcomm) Dilution of Precision

Min./Max.	GDOP	HDOP	VDOP	TDOP	# GPS SV	# LEO SV
Min.	1.50	0.53	1.29	0.46	8	1
Max.	5.91	1.43	4.98	2.84	8	4

Figure B.5 shows the resulting position and velocity RMSEs, Figure B.6 shows the result-ing clock state RMSEs, and Figure B.7 and Table B.3 show the probability of tracking GPS for each simulated GPS C/N$_0$ attenuation.
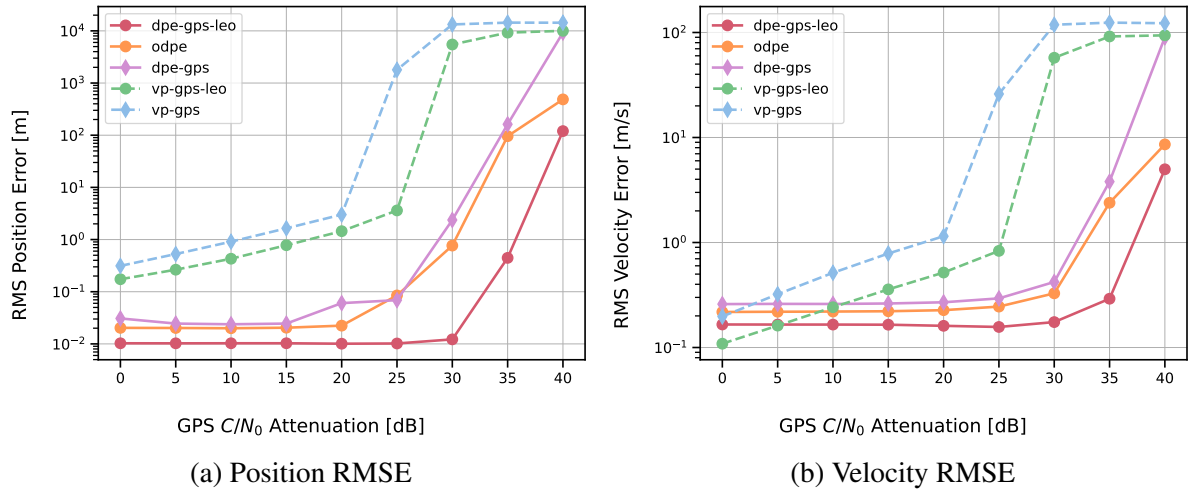

(a) Position RMSE

(b) Velocity RMSE

Figure B.5: Position and Velocity State RMSEs for Orbcomm Dynamic Ground Vehicle Study
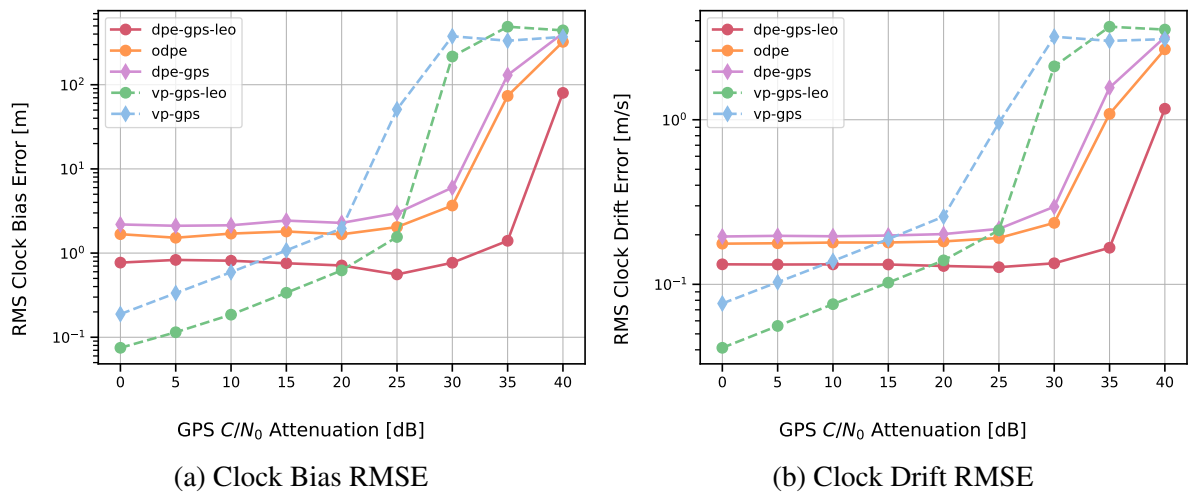

(a) Clock Bias RMSE

(b) Clock Drift RMSE

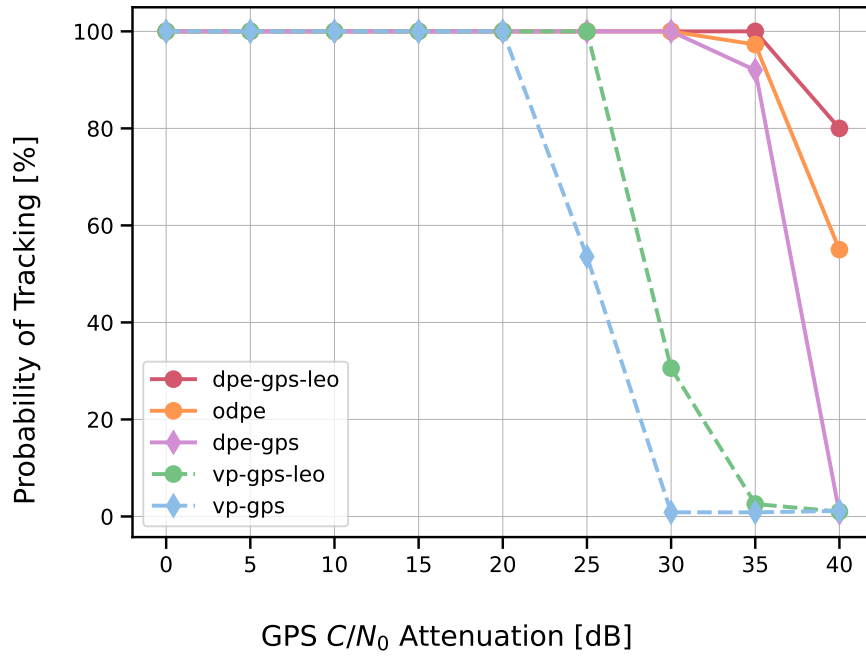Figure B.6: Clock Bias and Clock Drift State RMSEs for Orbcomm Dynamic Ground Vehicle Study

Figure B.7: Probability of Tracking GPS for Orbcomm Dynamic Ground Vehicle Study

Table B.3: Probability of Tracking GPS in High RFI for Orbcomm Dynamic Ground Vehicle Study

GPS C/N$_0$ Attenuation	DPE-GPS-LEO	ODPE	DPE-GPS	VP-GPS-LEO	VP-GPS
20 dB	100%	100%	100%	100%	100%
25 dB	100%	100%	100%	100%	53.6%
30 dB	100%	100%	100%	30.6%	0.86%
35 dB	100%	97.3%	92.0%	2.57%	0.86%
40 dB	80.0%	55.0%	0.71%	1.00%	1.14%